공학박사 학위논문

평행금속판 도파로를 이용한 테라헤르츠 파의 전파 특성 연구

The properties of Terahertz Wave Propagation in Parallel-Plate Waveguides

지도교수   전 태 인

2013년 2월

한국해양대학교 대학원

전기전자공학부

이 의 수

본 논문을 이의수의 공학박사 학위논문으로 인준함.

위원장   장 낙 원   (인)

위 원   전 태 인   (인)

위 원   서 동 환   (인)

위 원   주 양 익   (인)

위 원   박 경 현   (인)

2013 년   1 월

한국해양대학교 대학원

PREFACE

I would like to sincerely thank my adviser, Dr. Tae-In Jeon for welcoming me as his PhD student and setting me on a path for achieving scientific excellence. His immense knowledge, wisdom, guidance, patience, and the extremely high standards set by him for laboratory performance has inspired me to achieve great things. I am really proud of what we have accomplished together in the past four years. He was always an instant help to me whenever I struggled in the lab. He always motivated me and showed the right path every time I felt low during my research. Thanks a lot for everything you have done for me and the financial support throughout this study.

And I would like to thank my colleagues, Dr. Young-Bin Ji, Jin-Suk Jang, Sang-Hoon Kim, JeongSang Jo, Hyeon-Sang Bark, Eom-Bae Moon, Jingshu Zha, and Geun-Ju Kim for many fruitful discussions and help which I got from them on a very regular basis.

Finally, I would also like to thank my parents Jeom-Jae Lee and Young-Sook Bae; my loving girlfriend Mi-Kyoung Kim. They give me encouragement and love throughout this process.
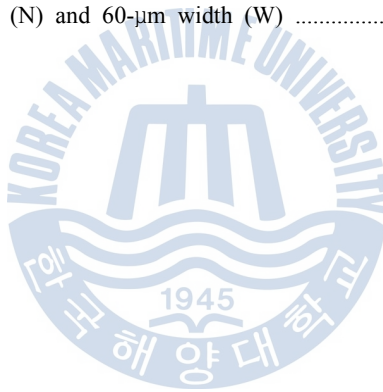
TABLE OF CONTENTS

Chapter			Page

- Ⅴ -

LIST OF TABLES

LIST OF FIGURES

- XI -

- XII -

▶ The work presented in this thesis is based on the work published in the following papers in refereed journals :

P1. **E. S. Lee**, J. S. Jang, S. H. Kim, Y. B. Ji, and T.-I. Jeon, *"Propagation of Single-Mode and Multi-Mode Terahertz Radiation Through a Parallel-Plate Waveguide,"* J. Korean Phys. Soc. **53**, 1891 (2008).

P2. **E. S. Lee** and T.-I. Jeon, *"THz Filter Using the Transverse-electric (TE₁) Mode of the Parallel-plate Waveguide,"* J. Opt. Soc. Korea. 13(4), 423-427(2009)

P3. **E. S. Lee**, D. H. Kang, A. I. Fernandez-Dominguez, F. J. Garcia-Vidal, L. Martin-Moreno, D. S. Kim, and T.-I. Jeon, *"Bragg reflection of terahertz waves in plasmonic crystals,"* Opt. Express 17(11), 9212‒9218 (2009).

P4. S.-H. Kim, **E. S. Lee**, Y. B. Ji, and T.-I. Jeon, *"Improvement of THz coupling using a tapered parallel-plate waveguide,"* Opt. Express 18(2), 1289‒1295 (2010).

P5. **E. S. Lee**, Y. B. Ji, and T.-I. Jeon, *"Terahertz band gap properties by using metal slits in tapered parallel-plate waveguides,"* Appl. Phys. Lett. 97(18), 181112 (2010).

P6. **E. S. Lee**, S.-G. Lee, C.-S. Kee, and T.-I. Jeon, *"Terahertz notch and low-pass filters based on band gaps properties by using metal slits in tapered parallel-plate waveguides,"* Opt. Express 19(16), 14852‒14859 (2011).

P7. S.-G. Lee, C.-S. Kee, **E. S. Lee**, and T.-I. Jeon, *"Photonic band anti-crossing in a coupled system of a terahertz plasmonic crystal film and a metal air-gap waveguide,"* J. Appl. Phys. 110(3), 033102 (2011).

P8. S.-G. Lee, **E. S. Lee**, T.-I. Jeon, and C.-S. Kee, *"Properties of defected one-dimensional terahertz plasmonic crystal films in a metal air-gap waveguide,"* J. Appl. Phys. 110(9), 093101 (2011).

P9. **E. S. Lee**, J.-K. So, G.-S. Park, D. Kim, C.-S. Kee, and T.-I. Jeon, *"Terahertz band gaps induced by metal grooves inside parallel-plate waveguides,"* Opt. Express 20(6), 6116‒6123 (2012).

P10. **E. S. Lee** and T.-I. Jeon, *"Tunable THz notch filter with a single groove inside parallel-plate waveguides,"* Opt. Express 20(28), 29605-29612 (2012).

P11. **E. S. Lee** and T.-I. Jeon, *"Resonant transmission through slit arrays patterned parallel-plate waveguide,"* Submitting

평행금속판 도파로를 이용한
테라헤르츠 파의 전파 특성 연구

이 의 수

Division of Electrical and Electronics Engineering
Graduate School of
Korea Maritime University

Abstract

테라헤르츠(이하, THz) 파는 전자기파 스펙트럼 영역에서 마이크로웨이브 영역과 적외선 영역의 사이로, 일반적으로 0.1 ~ 10 THz (파장 : 3mm~30μm)에 해당하는 파를 말하며, 적외선이 가지는 직진성과 마이크로웨이브가 가지는 투과성을 동시에 가지는 독특한 특성을 가지는 영역대의 전자기파이다. 따라서, 비금속성을 띄는 대부분의 물질의 (옷, 나무, 플라스틱, 종이 등) 투과가 가능하여 이와 같은 재질로 내부에 숨겨져 있는 물질의 확인이 가능하며 (이미징), 인체와 같은 바이오 물질의 경우, 기존에 사용되어 오던 X-ray에(10^6 THz = 4.13 keV) 비하여 에너지가 (1 THz = 4.13 meV) 현저히 낮기 때문에 물질의 원자나 분자를 이온화 시키지 않는 비파괴 특성을 가진다. 또한, 많은 물질의 분자들이 THz 영역에서 공진 특성을 가지고 있어 물질의 연구(분광학)에도 많이 사용되고 있다. 게다가, 앞으로 기존의 무선 통신 및 정보 처리 등에 있어 더 넓은 대역폭과 더 빠른 속도를 필요로 함에 따라 THz 파가 사용되게 될 것이다. 이

렇듯, 앞으로 그 응용은 기존의 다른 영역의 기술과 결합하여 계속해서 확대되게 될 것이다.

최근, THz 파의 단일 횡전자계(TEM) 모드의 전파가 가능한 평행금속판도파로의 특성을 이용하여, 분광학(spectroscopy), 포토닉 도파로(photonic waveguide), 이미징, 필터, 센서 등의 여러 분야에서 활발한 응용이 진행되고 있다. 이 중에서 THz 파의 다양한 응용 및 집적 회로의 구현 등, 모든 시스템에 기본적으로 필요한 수동 소자, 즉 여러 기능의 필터 개발은 반드시 필요하다. 이에 본 저자는 스펙트럼 영역에서 강한 차단 영역, 즉 밴드 갭의 형성이 가능한 포토닉 결정 구조를 평행금속판도파로 구조와 결합하여 다양한 기초 연구 및 그 응용 연구를 실시하였다.

먼저, (Chapter II) 평행금속판도파로의 기본 단일, 다중 모드 전파 특성에 관한 기초 연구를 이론 및 실험을 통하여 실시하였으며, (Chapter III) 이 중, 저주파 영역을 차단하는 스펙트럼 전파 특성을 가진 TE$_1$ 모드를 이용하여 THz 고주파 대역 통과 필터를 구현하였다. 그리고, (Chapter IV) 파장 이하의 좁은 공간에 THz 파를 집속, 전파가 가능한 평행금속판도파로의 특성을 이용하여 THz 파가 평행금속판도파로로부터 빠져 나오는 출구 근처에(THz 표면파) 슬릿 배열의 포토닉 결정 구조를 위치시켜, THz 표면파와 포토닉 결정 구조 간의 강한 Bragg 반사 현상과 이에 대한 각 슬릿의 반사 계수를 성공적으로 측정하였다. (Chapter V) 그리고, 기존까지 자유 공간을 전파하는 THz 파를 파장 이하의 평행금속판도파로 갭 사이로 결합시키기 위해 준광학 기법인 실리콘 렌즈가 사용되었다. 하지만, 이는 실리콘 렌즈의 높은 굴절률(n=3.417)에 따른 반사 손실이 두 실리콘 렌즈의 의해 약 50 %가 발생하며 또한, 실리콘 내부 전반사로 인하여 시간 영역에서 긴 측정을 불가능하게 만드는 다중 반사 신호가 측정된다. 따라서, 실리콘 렌즈를 경사각 3°를 가지는 경사진 도파로 구조로 대체하여 기존 실리콘 렌즈의 사용에 비해 약 2배 이상의 결합 효율 향상 및 내부 전반사를 제거하였다.

(Chapter VI) 이 장에서는 Chapter V에서 연구 된 포토닉 결정 구조, 즉

슬릿 배열을 평행금속판도파로 내의 갭 중앙에 위치시켜, 집속된 THz 파와 슬릿 배열 간의 여러 강한 밴드 갭을 구현하였고, 발생한 여러 밴드 갭에 대한 그 형성 메카니즘을 C언어를 이용하여 직접 구현한 Finite-Difference Time-Domain 시뮬레이션을 이용하여 완벽히 분석하였다. (Chapter VII) 그리고, photonic band anti-crossing 모델을 이용하여 앞서 형성된 밴드 갭 중, 평행금속판과 슬릿 사이의 간격에 따라 밴드 갭의 위치가 변화는 현상을 다른 접근에서 분석하였으며, (Chapter VIII) Chapter VI에서 형성된 밴드 갭 내에 결함 구조의 슬릿 배열을 이용, 강한 결함 모드를 발생시켜 이에 대한 연구를 실시하였다. (Chapter IX) 그리고, 앞서 분석한 밴드 갭 형성 메카니즘의 이해를 바탕으로, 저주파, 특정 주파수 대역 통과 필터 및 특정 주파수 가변 차단 필터를 개발하였고, 이를 미량의 가스 검출이 가능한 센서로의 적용을 실시하였다.

(Chapter X) Chatper VI에서 연구된 슬릿 배열과 유사한 홈(groove) 배열을 평행금속판도파로의 갭 중앙이 아닌 한쪽 금속판 내에 구조화하여 앞서 슬릿 배열의 경우보다 더 많은 여러 밴드 갭의 구현 및 그 형성 메카니즘을 분석하였다. (Chapter XI) 그리고, 앞서 Chapter X에서의 여러 밴드 갭을 이용하여 여러 필터 및 미량의 가스 및 유동 액체 센서로의 응용을 실시하였다.

(Chapter XII) 이 장에서는 새로운 형태의 평행금속판도파로를 제안한다. 기존의 두껍고 평평한 평행금속판 구조에서 30 μm의 얇은 금속판에 슬릿 배열을 가공하여 도파로의 내외부가 슬릿을 통하여 연결이 되도록 하였다. 따라서, 도파로 내부를 전파해 나가던 THz 파가 전자기파의 회절 현상으로 인하여 공기 슬릿 배열을 통하여 도파로 내에서 외부로 빠져나가게 되는 반면, 도파로의 공기 갭의 두 배에 해당하는 길이의 파장에서 강한 투과 공진 현상이 일어나게 되어, 마치 특정 밴드 패스 필터의 특성을 가지게 되었다. 이는 횡전자계 모드를 이용한 저주파 차단은 처음이며, 공기 갭의 조절에 의하여 특정 밴드의 주파수 가변이 가능하다. 또한, 외부로 드러나는 특이한 구조로 인하여 앞으로 다양한 응용의 가능성이 기대된다.

Chapter I.   Introduction

Over the past 20 years, terahertz (THz) technologies have been shown the dramatic growth as the development of THz time-domain spectroscopy (THz-TDS). THz waves can penetrate non-conducting materials (such as clothing, wood, plastic, paper etc.) that make us see inside objects. And THz radiation can be used for medical imaging that biological tissues are not ionized unlike X-rays. Many various kinds of materials can be also characterized by the strong interaction with THz waves. And THz frequency can offer faster speeds and larger bandwidth with more channels compared with currently used wireless communication. So, this THz frequency can be utilized for various fields such as security [1], imaging [2], manufacturing [3], medical imaging [4], communication [5], astronomy [6], spectroscopy [7], etc..

To realize compact THz applications mentioned above, we need new higher power source and detector. In addition, the development of waveguides which can transfer energy efficiently and functional devices such as switches, filters, divider, and modulator, etc. are necessary for THz integrated circuits.

1.1 Metal parallel-plate waveguides

Over the past decade, THz waveguides are one of the important topics which have been researched intensively in the THz community. And the demand for ever increasing bandwidth from GHz frequency regions and the succeeding improvements in device performance will keep pushing us on the development of various THz waveguides, more and more.

For supporting the low-loss and single transverse electromagnetic (TEM) mode propagation, various THz wave guiding structures have been demonstrated, such as circular and rectangular metals [8,9], single-crystal sapphire fibers [10], plastic ribbon planar wave guides [11], coplanar and single metal wires [12−15], coaxial cables [16], and metal *parallel-plate waveguides* (*PPWGs*) [17,18]. All of above

each waveguides have their strengths and weaknesses. By the extreme group velocity dispersion near the cutoff frequencies of several waveguide structures, sub-ps THz pulses have been broadened excessively [8-11]. But this excessive pulse broadening would not occur for TEM modes such as a two-wire transmission line, a coaxial transmission line, or a *PPWG* because they don't have a cutoff frequency. And among these waveguides, quasi-optic coupling techniques are not effective for the two wire or the coaxial transmission lines because of their complex field patterns of the TEM modes. However, the simple field pattern of the TEM mode of PPWGs makes quasi-optic coupling techniques be possible efficiently.

PPWGs have been researched in the many various application fields as one of most active fields. PPWGs with ability of single TEM mode transmission with the low-loss and negligible dispersion have been employed in studies on high resolution spectroscopy [19], sensing [20], imaging [2], filtering [21], the super-prism effect [22], Bragg resonances [23], photonic waveguides [24], wave guiding [18,25], and surface plasmon coupling [26], etc.. In the recently, even by using the dispersive TE_1 mode propagation, universal THz filters [27,28], THz guiding [29], and sensing applications [30,31] are demonstrated efficiently.

1.2 Photonic crystals

Photonic crystals can occur in nature and be also formed artificially and the concept is originally from the solid state physics. In a semiconductor crystal, the periodic potential of the atoms arranged periodically affects the electron motion by creating allowed and forbidden electronic energy bands. This forbidden electronic energy bands is named as *photonic band gaps* or *energy gaps* where light at certain wavelengths cannot propagate through it.

Analogically, if a material has regularly repeating structure in space, *photonic band gaps* are formed. So, if materials are designed as photonic crystals, the wave propagation can be manipulated and controlled. Such a photonic crystals have been

well characterized in both the microwave and optical regimes.

At THz frequencies, various photonic crystal demonstrations have been researched such as 1-D dielectric stacks [32], 2-D metallic [33] and dielectric photonic crystals [34] embedded in PPWGs, free-standing dielectric 2D photonic crystals [35], hole arrays [36], plastic photonic crystal fibers [37], etc.. As mentioned above, the primary demonstrations of photonic crystals are their filtering capability, such as stop bands having a dynamic range up to 40 dB over varying bandwidths. Among these research of various structures, our study will focus on the photonic crystals embedded in PPWGs. Due to the simple structure of PPWGs, various photonic crystals can be easily combined and the structure of planar photonic crystals are necessary for single-chip interconnects.

1.3 Outline of Thesis

As mentioned above, PPWGs are the ideal tool for use in various THz applications. In **Chapter II**, we investigate the fundamental propagation properties of single- and multi-mode THz radiation through PPWGs at various inter-plate sizes and THz field polarizations. This understanding will be certainly needed before we utilize PPWGs for THz applications. In **Chapter III**, we develop our initial PPWG THz application—a high-pass filter utilizing the TE_1 mode. In **Chapter IV**, we demonstrate the successful measurement of surface plasmon (SP) Bragg reflection using PPWGs and estimate the value of reflection coefficients at a series of slits in a photonic crystal array placed near the exit of a PPWG. As was highlighted in Chapter 1.1, a PPWG structure can confine the propagated THz waves within sub-100 μm air gaps, resulting in the launch of SPs within the structure that interact strongly with the slits of a specially fabricated array of photonic crystals located at the PPWG exit, resulting in Bragg reflection. In **Chapter V**, we describe a novel type of a PPWG in which the cylindrical Si lens is replaced with a tapered structure (a tapered PPWG or TPPWG). This simplified structure avoids many of the drawbacks of Si lenses and allows increased coupling of terahertz

energy into the PPWG; as such, it will be used in all of the experiments further described in this thesis and in many other terahertz waveguide applications.

In **Chapter VI**, we describe the results of several studies carried out in which a series of metal slit arrays were positioned at the center of the air gap in a TPPWG. Whereas the research described in Chapter **IV** involved only Bragg reflection, the 1-D photonic structures developed here induce several interesting band gap structures having a variety of formation mechanisms. The properties of the induced band gaps are analyzed through experimental and FDTD simulation studies. Using the photonic band anti-crossing model, we deduce in **Chapter VII** that the position of the forbidden frequency gap depends on the ratio of the period of the plasmonic crystal to the air-gap size, and in **Chapter VIII**, we investigate the characteristics of the localized defect modes caused by a defect slit located at the center of the slit array in a PPWG. This is examined for potential use in THz sensor applications. In **Chapter IX**, the applications of induced band gaps for use in various types of THz filter applications including a low-pass filter (LPF), a (tunable) notch filter, and a gas sensor are explored.

In **Chapter X**, the characteristics of band gaps caused by locating metal grooves within a flare PPWG are shown. Using deep grooves, we are able to investigate, through an experiment and FDTD simulation studies, several interesting band gap types, each having a different forming mechanism, and then in **Chapter XI**, we again assess the potential applications of each band gap type for use in THz applications such as LPFs, (tunable) notch filters, and microfluidic sensors. Finally, in **Chapter XII**, we suggest another novel PPWG structure, i.e., a photonic PPWG, in which two metal plates are patterned with slit arrays having a half pitch off-set, and explore a new resonant transmission pathway through this device in which terahertz waves leak through the air slits via diffraction. A new resonance at a wavelength corresponding to half the size of the air gap is demonstrated. All of these studies are reviewed, and we present our conclusions and recommendations for future work in **Chapter XIII**.

1.4 Broadband THz setup
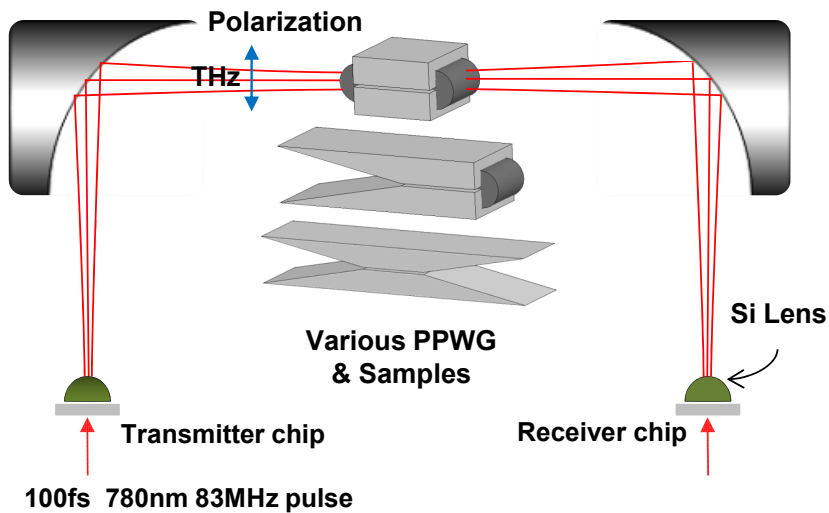
Figure 1.1   Diagram of standard THz-TDS system.

Figure 1.1 is a standard THz-TDS system based on photoconductive switch antenna [38] which is used in all of my experimental work. The explanation about THz-TDS system has been well detailed in many places, we will not give the detailed mention.

THz radiation is generated and detected using photoconductive switches driven by 12mW optical pulse trains from an 780 nm, ~100fs, 83MHz mode locked Ti: sapphire femtosecond laser. The transmitter chip (Tx) to generate THz pulse consists of simple coplanar transmission line structure of two 10 µm wide metal lines separated by 80 µm, fabricated on LT-GaAs. The laser excitation is focused onto the metal-semiconductor interface of the positively biased (80V) transmission line to create a spot of photocarriers. The receiver chip (Rx) to detect THz pulse consists of two 20-µm-wide stubs separated by a 5-µm gap in a coplanar transmission line consisting of two parallel 10-µm-wide aluminum lines separated

- 5 -

from each other by 30µm. This structure was fabricated on an ion-implanted silicon-on-sapphire (SOS) wafer. The generation and detection of THz pulses were well discussed previously [38]. And various PPWGs and sample will be placed in the collimated THz beam between the transmitter and receiver as shown in Fig. 1.1. So, we could characterize the properties of samples by taking the numerical Fourier transform of the comparison by THz pulses passed through it or not.

Chapter II.   THz propagation through PPWGs

As previously stated, PPWG is the ideal tool for various THz applications. In this chapter, we present an experimental study with a theoretical explanation, of single- and multi-mode THz propagation through a PPWG. The air gap's sizes and polarizations of THz field will vary for a deep understanding. And then, based on this propagation properties, we will try to demonstrate a high pass filter using TE_1 mode, results in the cutoff of the low frequency region in Chapter III.

2.1   Waveguide Specimen
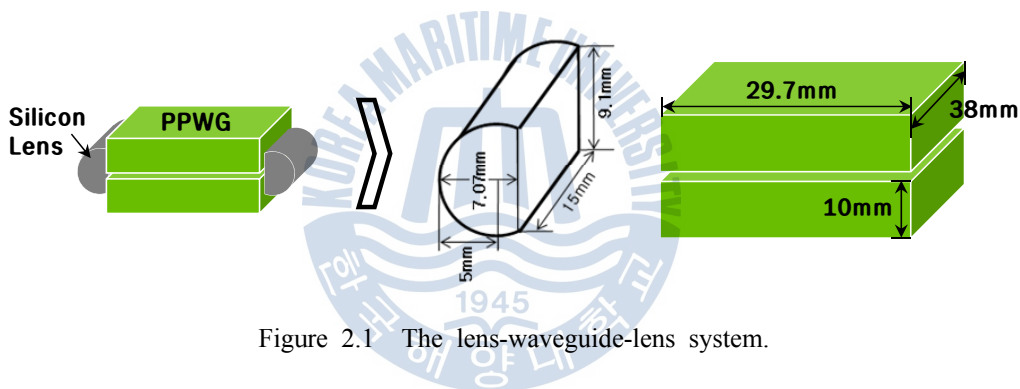
Figure 2.1   The lens-waveguide-lens system.

As shown in Fig. 2.1, the waveguide consists of two parallel conducting plates and two plano-cylindrical Si lenses [17]. Silicon material is chosen for the plano-cylindrical lenses, due to its low dispersion and absorption properties in the THz frequency range. Two plates are combined with sub-wavelength air gaps to guide THz pulse through. But having such small gap sizes compared to the wavelengths makes the coupling of THz pulses into PPWGs's air gap hard. So, by using the quasi-optic coupling technique of cylindrical lenses, THz beams is shaped and reduced the beam to make it suitable for coupling into the sub-wavelength gap. Therefore, Si lenses are attached to input side of PPWG to focus the incoming

THz beam into the small air gaps and output side of it to radiate the outcoming THz beam from the air gaps as shown in Fig. 2.1.

In this experiment, PPWG plates were machined and polished using commercially available aluminum. Due to the small air gap, in the manufacturing process, the inner surfaces of PPWG plates and input and output faces of waveguide need a high degree of precision. If the precision of plates are low, the air gap will not be constant value which means the different air gaps over the entire plates. It leads to inaccurate experiment results. PPWG plates were fabricated with the dimensions of 38-mm wide, 29.7-mm long and 20-mm thick. And two plano-cylindrical high-resistivity Si lenses couple THz radiation into and out of waveguide with line focus. The lenses are 15 mm x 9.1 mm x 7.07 mm with a 5 mm radius of curvature, and have a low power absorption constant in the order of 0.05 cm^{-1} and a high resistivity silicon (n=3.418) at THz frequencies [39]. The waist of the THz beam due to the plano-cylindrical Si lens is within sub-hundred micrometers.

- 8 -
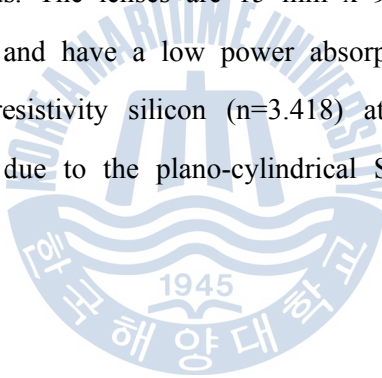
2.2   Fundamental theory of PPWG

Waveguides are structures used to guide EM waves from point to point. However, the fundamental characteristics of waveguide are definitely different with propagation modes which result from the basic differences in geometry for a waveguide. When EM wave is incident into one side of a PPWG, it hits the walls during the propagation through it which results in the multi-reflection. These reflected waves by the interaction with each other make particular EM field patterns in a plane perpendicular to the propagation direction of EM wave. They have unique properties each and we call them, 'modes' or 'transverse mode'. The allowed modes can be obtained by solving Maxwell's equations for the boundary conditions of a given waveguide.

These transverse modes in a PPWG can be classified into three types, TEM mode (Transverse ElectroMagnetic mode, TM_0) which doesn't have electric and magnetic field in the direction of propagation, and TM modes (Transverse Magnetic) which don't have magnetic field in the direction of propagation, and TE modes (Transverse Electric) which don't have electric field in the direction of propagation. The existence of modes in PPWG can be determined by a) the material, shape and size of a PPWG, b) the material inside a PPWG, c) the operating frequency. Among these modes, only TEM mode doesn't have cutoff frequencies which waves can not propagate through PPWG in the lower frequency region of it.

In this chapter, we introduce several useful basic formulas to analyze the experimental data [40,41].

2.2.1   General Wave Characteristics in a PPWG structure

Given any time-harmonic source of EM radiation, when the EM waves propagate away from the source through a medium characterized by ε and μ, the phasor electric and magnetic fields must satisfy the *source-free Maxwell's equations* given by

$$\text{Faraday' law} \ : \ \nabla \times \widetilde{E} = - j\omega\mu\widetilde{H} \tag{1}$$

$$\text{Ampere's law} \ : \ \nabla \times \widetilde{H} = j\omega\varepsilon\widetilde{E} \tag{2}$$

The source-free Maxwell's equations can be manipulated into wave equations for the electric and magnetic fields. These *wave equations* are

$$\nabla^2\widetilde{E} + k^2\widetilde{E} = \nabla^2\widetilde{H} + k^2\widetilde{H} = 0, \qquad where \quad k = \omega\sqrt{\mu\varepsilon} \tag{3}$$

where the wavenumber k is real-valued for lossless media and complex-valued for lossy media.

The electric and magnetic fields of a general wave propagating in the +z-direction through an arbitrary medium with a *propagation constant* of γ are characterized by a z-dependence of $e^{-\gamma z}$.
The electric and magnetic fields of the wave may be written as

$$\widetilde{E}(x,y,z) = e(x)e^{-\gamma z} \tag{4}$$

$$\widetilde{H}(x,y,z) = h(x)e^{-\gamma z}, \tag{5}$$

$$\gamma = \alpha + j\beta \tag{6}$$

where α is the *wave attenuation constant* and β is the *wave phase constant*. The propagation constant is purely imaginary ($\alpha=0$, $\gamma=j\beta$) when the wave travels without attenuation (no losses) or complex-valued ($\gamma = \alpha + j\beta$) when losses are present.

For a parallel-plate waveguide, the plates are infinite in the y-extent, as shown in Fig. 2.2.

2.2.2 TM$_m$ mode (TM$_0$ = TEM)
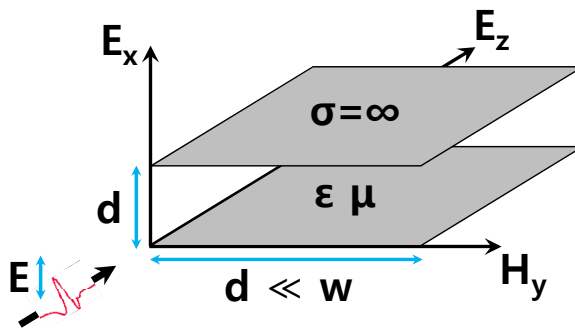
Figure 2.2   PPWG for TM modes.

When PPWG's plates are perpendicular to the incoming THz beams polarization, TM modes can be guided by *Maxwell's equations* (and *wave equations*) and *boundary conditions*. The waveguide is infinitely wide, oriented along the y-axis, and uniform along z-axis. And the longitudinal electric field of the TM mode are determined by solving the appropriate boundary value problem for the given waveguide geometry.

The TM boundary conditions for the PPWG structure are

$$\widetilde{E_z^{TM}}(0,y,z) = \widetilde{E_z^{TM}}(d,y,z) = 0 \tag{7}$$

So, the *longitudinal electric field*, E_z of the TM modes in the PPWG is given by

$$E_z = Asin(k_x x)e^{-\gamma_z z}, \text{ where } k_x = \frac{m\pi}{d}, \ m = 0,1,2,3,... \text{ and } \gamma_z = \alpha + j\beta_z \tag{8}$$

and using Maxwell's equations, *other field components* can be written as

Ampere's law : $-\frac{\partial}{\partial z}H_y = j\omega\varepsilon E_x, \ \ \frac{\partial}{\partial x}H_y = j\omega\varepsilon E_z$

$$H_y = -\frac{jw\varepsilon}{k_x}Acos(k_x x)e^{-\gamma_z z}, \tag{9}$$

$$E_x = -\gamma_z\frac{1}{k_x}Acos(k_x x)e^{-\gamma_z z} \tag{10}$$

- 11 -

2.2.3 TE modes
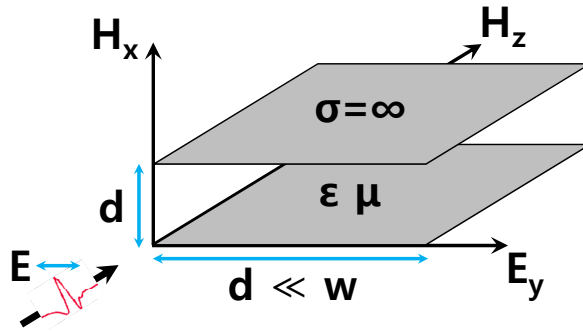
Figure 2.3   PPWG for TE modes.

When PPWG's plates are parallel to the incoming THz beams polarization, TE modes can be guided by *Maxwell's equations* (and *wave equations*) and *boundary conditions*. We apply the TE boundary conditions. Given no longitudinal electric field for the TE case, the boundary conditions for the transverse electric field components on the plates of the waveguide must be enforced. The TE boundary conditions are

$$\widetilde{E_y^{TE}}(0,y,z) = \widetilde{E_y^{TE}}(d,y,z) = 0 \tag{11}$$

So, the *transverse electric field*, E_y of the TE modes in the PPWG is given by

$$E_y = A\sin(k_x x)e^{-\gamma_z z}, \text{ where } k_x = \frac{m\pi}{d}, \ m = 0,1,2,3,... \text{ and } \gamma_z = \alpha + j\beta_z \tag{12}$$

and using Maxwell's equations, *other field components* can be written as

Faraday's law : $-\dfrac{\partial}{\partial z}E_y = -j\omega\mu H_x, \ \ \dfrac{\partial}{\partial x}E_y = -j\omega\mu H_z$

$$H_x = -\frac{\gamma_z}{jw\mu}A\sin(k_x x)e^{-\gamma_z z}, \tag{13}$$

$$H_z = -\frac{1}{j\omega\mu}k_x A\cos(k_x x)e^{-\gamma_z z} \tag{14}$$

- 12 -

2.2.4 Cutoff frequencies for TM and TE modes

The longitudinal electric field of the TM modes within the PPWG must satisfy the wave equation,

$$\nabla^2 \widetilde{E}_z + k^2 \widetilde{E}_z = 0, \qquad where \quad k = \omega\sqrt{\mu\varepsilon} \tag{15}$$

$$(\frac{\partial}{\partial z^2} + \frac{\partial}{\partial x^2} + \omega^2\mu\varepsilon)E_z = 0, \quad (\gamma_z^2 - k_x^2 + \omega^2\mu\varepsilon)E_z = 0 \tag{16}$$

So, propagation constant in the PPWG waveguide for TM modes is defined by

$$\gamma_{z,m} = \sqrt{k_x^2 - k^2} = \sqrt{k_x^2 - \omega^2\mu\varepsilon} = \sqrt{\left(\frac{m\pi}{d}\right)^2 - \omega^2\mu\varepsilon} \tag{17}$$

The Eq. (17) for the waveguide propagation constant $\gamma_{z,m}$ can be used to determine the cutoff frequency for the waveguide mode. The propagation characteristics of the wave are defined by the relative sizes of the parameters k_x and k. The propagation constant may be written in terms of the attenuation and phase constants as Eq. (6) : $\gamma_{z,m} = \alpha_m + j\beta_m$

so that,

if $k_x > k$: $\gamma_{z,m} = \alpha_m$, (Real number) $\Rightarrow e^{-\gamma z} = e^{-\alpha z}$

Waves are attenuated (*evanescent* modes)

if $k_x = k$: $\gamma_{z,m} = 0$, (0) $\Rightarrow e^{-\gamma z} = 0$, Cutoff frequency

if $k_x < k$: $\gamma_{z,m} = j\beta_m$, (Imaginary number) $\Rightarrow e^{-\gamma z} = e^{-j\beta z}$

Waves are not attenuated (*propagation* modes)

Therefore, the cutoff frequencies for the TM modes in the PPWG are found by solving,

$$f_{c,m} = \frac{m}{2d}\frac{1}{\sqrt{\mu\varepsilon}}, \quad m = 0, 1, 2, ... \tag{18}$$

Note that the cutoff frequency for a particular PPWG waveguide mode depends on the dimensions of the waveguide d, the material inside the waveguide ε and μ, and the indices of the mode m.

In general, the cutoff frequency will increase as the mode index increases. Thus, in practice, only the lower order modes are important as the waveguide is operated at frequencies below of the cutoff frequencies of the higher order modes. And the derived propagation constant, cutoff equations, phase velocity, and group velocity for PPWG in the TM modes ara the same for TE modes.

2.2.5 Waveguide Group velocity and Phase velocity

The velocity of propagation for the TEM wave is referred to as the phase velocity which a point of constant phase moves. The phase velocity of the TEM wave is equal to the velocity of energy transport. And the *phase velocity of the TEM wave* traveling in a lossless medium can be characterized by ε and μ is given by

$$v_{p,\,TEM}^{'} = \frac{\omega}{k} = \frac{1}{\sqrt{\mu\varepsilon}} \tag{19}$$

The phase velocity of TE or TM mode in a PPWG is defined in the same manner as that of the TEM wave which the velocity at which a point of constant phase moves. However, the waveguide phase velocity is not equal to the velocity of energy transport along the waveguide. The velocity at which energy is transported along the waveguide is defined as the *group velocity*. The differences between the waveguide phase velocity and group velocity can be understanded using the field equations of the TE or TM modes.

Let's consider the equation for the y-component of the TE_1 mode electric field, Eq (12) in a PPWG.

$$\widetilde{E_y^{TE_1}} = A sin(\frac{\pi x}{d})e^{-j\beta_{TE_1}z} \tag{20}$$

By applying the trigonometric identity: $\sin(\frac{\pi x}{d}) = \frac{1}{2j}[e^{j\pi x/d} - e^{-j\pi x/d}]$ (21)

This component of the waveguide electric field can be written as

$$\widetilde{E_y^{TE_1}} = \frac{A}{2j}[e^{-j(\beta_{TE_1}z - \pi x/d)} - e^{-j(\beta_{TE_1}z + \pi x/d)}] \tag{22}$$

$$e^{-\gamma_{z,1}z} = e^{-j\beta_{TE_1}z} \Rightarrow \gamma_{z,1} = \sqrt{k_{x,\,TE_1}^2 - k^2} = j\beta_{TE_1} \Rightarrow \beta_{TE_1} = k\sqrt{1 - \left(\frac{f_{c,\,TE_1}}{f}\right)^2} \tag{23}$$

- 15 -

The two terms in the TE$_1$ mode equation above represent TEM waves moving in the directions shown below.
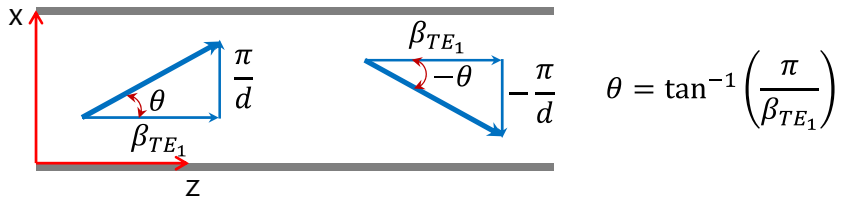
Figure 2.4 Two terms in the TE$_1$ mode represented TEM waves.

Thus, the TE wave in the PPWG can be represented as the superposition of two TEM waves reflecting from the upper and lower waveguide walls as they travel down the waveguide.
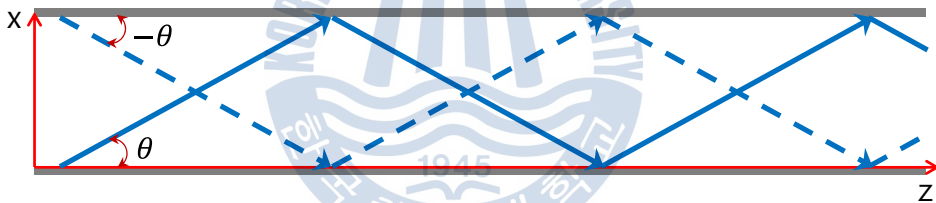
Figure 2.5 Two TEM waves reflecting from the upper and lower plates.

For the general TE$_m$ and TM$_m$ waves, the phase velocity of the TEM component is given by

$$v_{P,\,TM/E_m} = \frac{\omega}{\beta_{TM/E_m}} \tag{24}$$

Inserting the equation for the waveguide phase constant β_m gives

$$v_{p,\,TE_1} = \frac{\omega}{\beta_{TE_1}} = \frac{\omega}{k\sqrt{1-\left(\dfrac{f_{c,\,TE_1}}{f}\right)^2}} = \frac{v_p^{'}}{\sqrt{1-\left(\dfrac{f_{c,\,TE_1}}{f}\right)^2}} \tag{25}$$

The waveguide phase velocity represents the speed at which points of *constant phase of the component TEM* waves travel down the waveguide. The waveguide phase velocity is larger than the TEM wave phase velocity given that the square root in the denominator of the waveguide phase velocity equation is less than unity. The relationship between the waveguide phase velocity, waveguide group velocity, and the TEM component wave velocity is shown below.
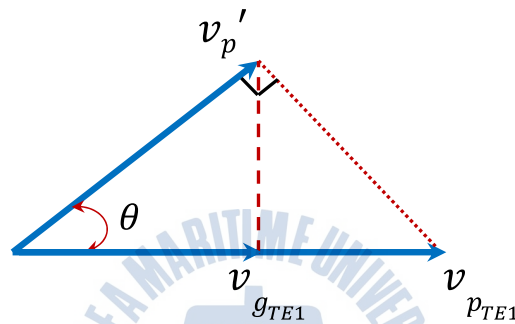
Figure 2.6   The relationship between the waveguide phase velocity $(v_{p,\,TE_1})$, waveguide group velocity $(v_{g,\,TE_1})$, and the TEM component velocity (v'_p).

$$v'_p = v_{p,\,TE_1} \cdot \cos\theta \;\;\Rightarrow\;\; v_{p,\,TE_1} = \frac{v'_p}{\cos\theta} \;\;\Rightarrow\;\; \cos\theta = \sqrt{1 - \left(\frac{f_{c,\,TE_1}}{f}\right)^2} \tag{26}$$

$$v_{g,\,TE_1} = v'_p \cdot \cos\theta = v'_p \cdot \sqrt{1 - \left(\frac{f_{c,\,TE_1}}{f}\right)^2} \tag{27}$$

$$v_{g,\,TE_1} \cdot v_{p,\,TE_1} = v'^2_p \tag{28}$$

The waveguide group velocity (the velocity of energy transport) is always smaller than the TEM wave phase velocity given the square root term in the numerator of the group velocity equation.

2.2.6 Attenuation in Waveguide

The propagating waves in the ideal PPWG characterized by a perfect conductor filled with a perfect insulator suffer no attenuation as the travel down the waveguide. But, two loss mechanisms exist in a realistic waveguide : 1) *conductor loss* and 2) *dielectric loss*.

1) The fields associated with the propagating waveguide modes produce currents that flow in the walls of the waveguide. Given that the waveguide walls are constructed from an imperfect conductor ($\sigma_c < \infty$), the walls act like resistors and dissipate energy in the form of heat.

2) Also, the dielectric within the waveguide is not ideal ($\sigma_d > 0$) so that dielectric also dissipates energy in the form of heat.

Therefore, the overall attenuation constant α for a realistic waveguide can be written in terms of the two loss components as

$$\alpha_{TM/E_m} = \alpha_{c_{TME}} + \alpha_{d_{TME}} \tag{29}$$

where $\alpha_{c_{TME}}$ is the attenuation constant due to conductor loss and $\alpha_{d_{TME}}$ is the attenuation constant due to dielectric loss.

The following absorptions are derived by following Reference [41].

$$\alpha = \frac{1}{d}\frac{R}{\zeta} \text{ for } TEM \tag{30}$$

$$\alpha = \frac{2}{d}\frac{R}{\zeta}\frac{1}{[1-(\lambda/\lambda_c)^2]^{1/2}} \text{ for } TM \tag{31}$$

$$\alpha = \frac{2}{d}\frac{R}{\zeta}\frac{(\lambda/\lambda_c)^2}{[1-(\lambda/\lambda_c)^2]^{1/2}} \text{ for } TE \tag{32}$$

R : the characteristic resistance of the metallic plate

ζ : the intrinsic impedance of the medium $= \sqrt{\dfrac{\mu}{\varepsilon}}$

2.3 Single TEM and TE$_1$ mode
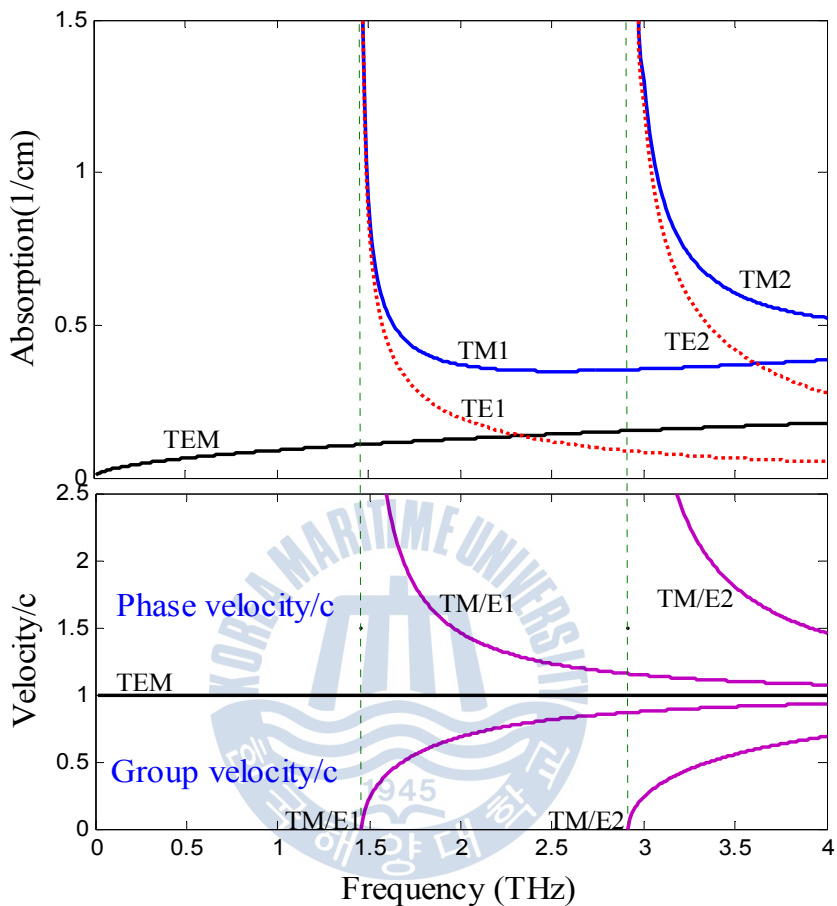
Figure 2.7   (a) Field absorption and (b) Phase and group velocities for TEM and the first two modes with a plate separation of 103 µm. Cutoff frequencies for the TM and the TE modes are shown by the dotted vertical lines.

Before we measure the propagated THz waves of the single TEM and TE$_1$ mode through a PPWG, we get the useful information about their modes by using the basic formulas, Eq. (1)~(32). The calculated absorptions for TEM and the two modes for a 103-µm air gap are shown in Fig. 2.7(a). Because of the reactive wave impedance before the cutoff frequency, the amplitude for each mode should

be zero in the spectrum. Since the absorptions of higher TM modes, not TEM mode, are bigger than those of TE modes, the THz amplitudes of TM modes are more attenuated than those of TE modes in the high frequency region. The TEM mode has no cutoff frequency and its absorption gradually increases with increasing frequency; also, it has the smallest absorption coefficient compared with higher TM modes in all frequency ranges. But, in the high frequency region, the graph shows that the absorption of TE mode is lowest.

Figure 2.7(b) shows the phase and the group velocities for a 103-µm air gap. When the frequency increases from the cutoff frequency, the phase velocity and the group velocity approach the speed of light in free space. The group velocity of each mode gets faster and approaches the speed of light with increasing frequency. But near the cutoff frequency, the group velocity becomes the zero velocity so we need very long scans to detect the signal. And in the all modes except TEM mode, the propagted waves will be showed the phenomenon of negative chirp which the lower frequencies travel slower than the higher frequencies.

2.3.1   Experimental Results : Reference and single TEM mode
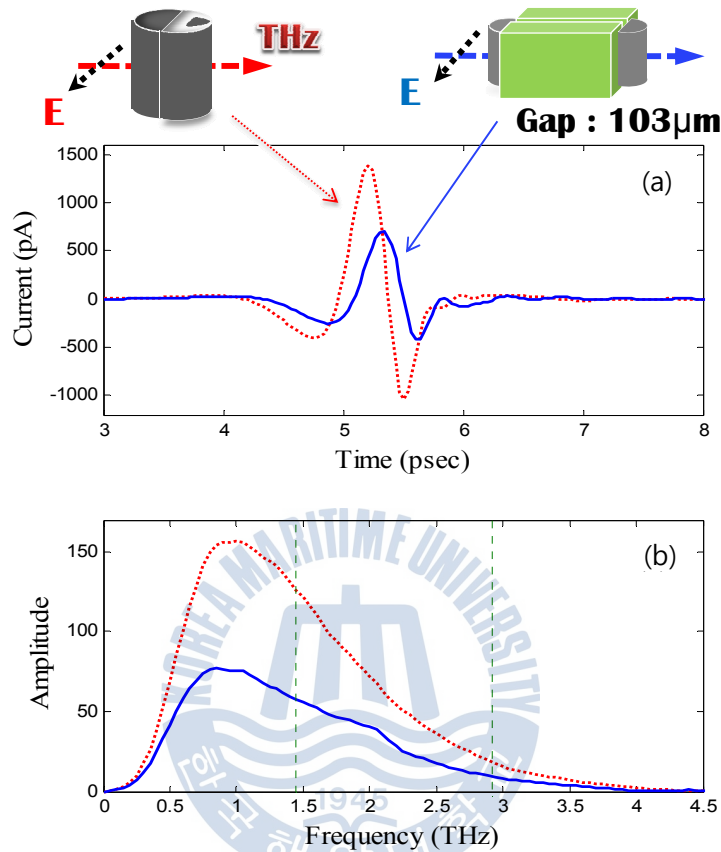
Figure 2.8 (a) The measured for reference and TEM mode THz pulses with a 103 µm air gap when the polarization is normal to the plates. (b) Amplitude spectra of the reference and TEM mode THz pulses.

The reference pulse is obtained by removing PPWG and attaching the two cylindrical Si lenses because their confocal position is almost on the flat surface. This measured pulse has a peak to peak of approximately 2.4 nA and a available spectrum band from 0 to 4 THz, as shown in Fig. 2.8 (dashed line). The measured dispersionless pulse shape means that Si lens does not distort THz pulse. To characterize the THz propagation through PPWG, PPWG is positioned between Si

- 21 -

lenses. The center of flat Si surfaces are adjusted to the center of small air gap at the input and output of PPWG. The polarization of THz pulse is perpendicular to the plate surfaces. The measured THz pulse and spectrum through the 29.7 mm long PPWG with a 103 µm air gap is shown in Fig. 2.8. The amplitudes of pulse and spectrum are decreased, but it clearly shows a negligible group-velocity dispersion. Actually, the reason of changed amplitude is due to the reflection at the input and output faces of PPWG by the mismatch in the size of the focused beam and air gaps, not the propagation loss from real metal with the finite conductivity [41]. The measured two pulse shapes (not amplitude) in Fig. 2.8(b) are almost similar that there are no delayed oscillation and no cutoff frequency (in the spectrum). So, this means that THz pulse can propagate through PPWG with single TEM mode.
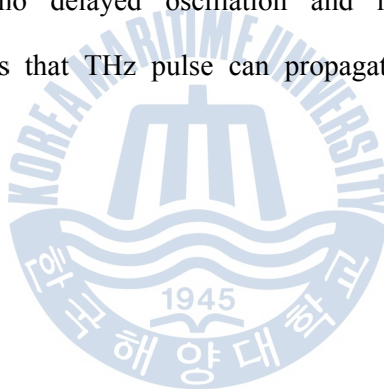
2.3.2　Experimental Results : TE mode
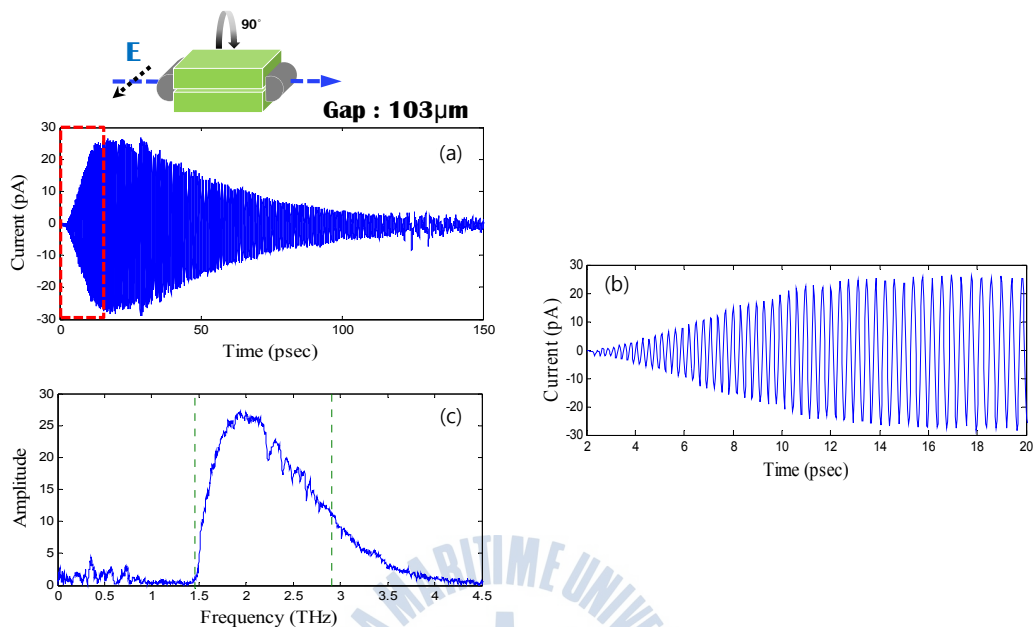
Figure 2.9　(a) Measured TE$_1$-mode THz pulse transmitted through a PPWG with a plate separation 103 µm when the polarization direction of the input electric field is parallel to the plates. (b) Extension of the oscillation from 2 psec to 20 psec. (c) Relative amplitude spectrum of the TE$_1$-mode pulse.

When the PPWG is rotated 90 degrees and made parallel to the incoming THz beams polarization, the measured THz pulse is as shown in Fig. 2.9(a). The air gap and size of PPWG are exactly same with that of TEM mode. Based on the well-known wave equations, Maxwell's equations and the boundary conditions, only TE modes can exist in the PPWG. Because of the high group-velocity dispersion near cutoff frequency, the time domain pulse is stretched and expands to more than 150 psec with negative chirp which the lower frequencies travel slower than the higher frequencies, as shown in Fig. 2.9(a). Figure 2.9(b) shows the extension of the oscillation from 2 psec to 13 psec for clarity. And the spectrum of the

- 23 -

time-domain THz pulse is shown in Fig. 2.9(c). The low frequency is truncated until 1.46 THz, which is the first cutoff frequency to show up and the spectrum extends up to 4 THz. The calculated cutoff frequency and the experimental results agree well. It can't detect any THz signal below the cutoff frequency because the wave impedance only has reactive components that can be used for a high pass filter for a THz system. The incident THz beam has even field pattern and the receiver chip is not sensitive to the odd field pattern. So, the second-order TE mode (TE$_2$ mode) does not show up in the spectrum because of the odd field pattern.

2.4 Multi-TM and TE modes
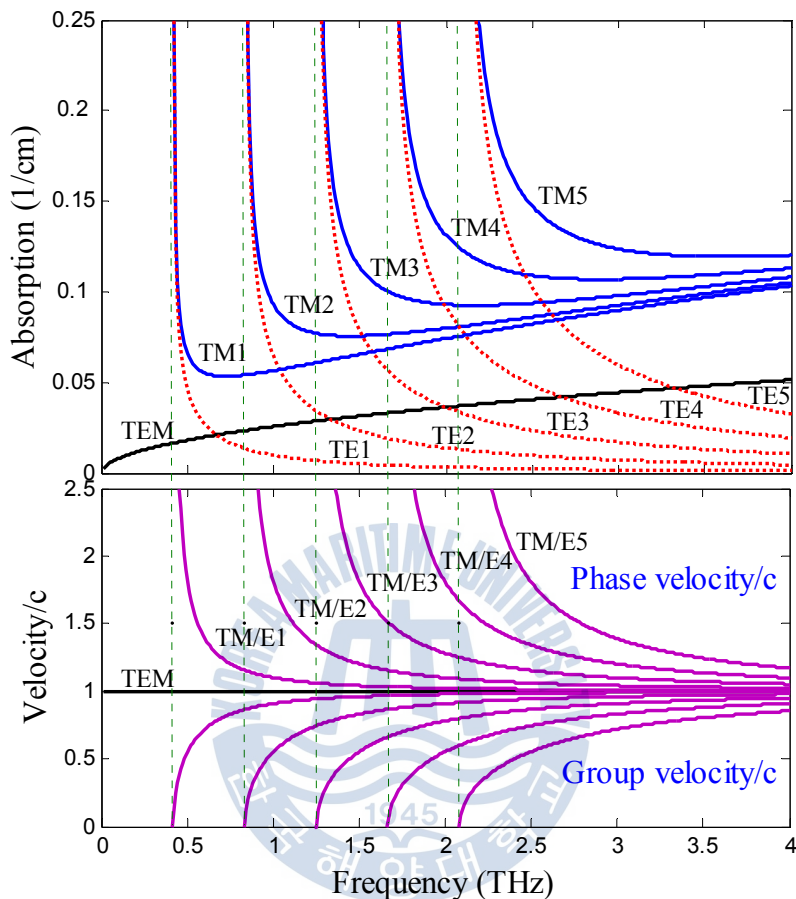
Figure 2.10 (a) Field absorption and (b) Phase and group velocities for TEM and the first five modes with a plate separation of 360 µm. Cutoff frequencies for the TM and the TE modes are shown by the dotted vertical lines.

Figure 2.10 shows the absorptions, phase and the group velocities for TEM and the first five modes with a 360-µm air gap. By the increased air gap with a plate separation of 360 µm, the nine modes can exist in the 4 THz for each modes, according to the Eq. (18). The their properties between modes are similar with that of the a 103-µm air gap.

2.4.1 Experimental Results : multi-TM modes
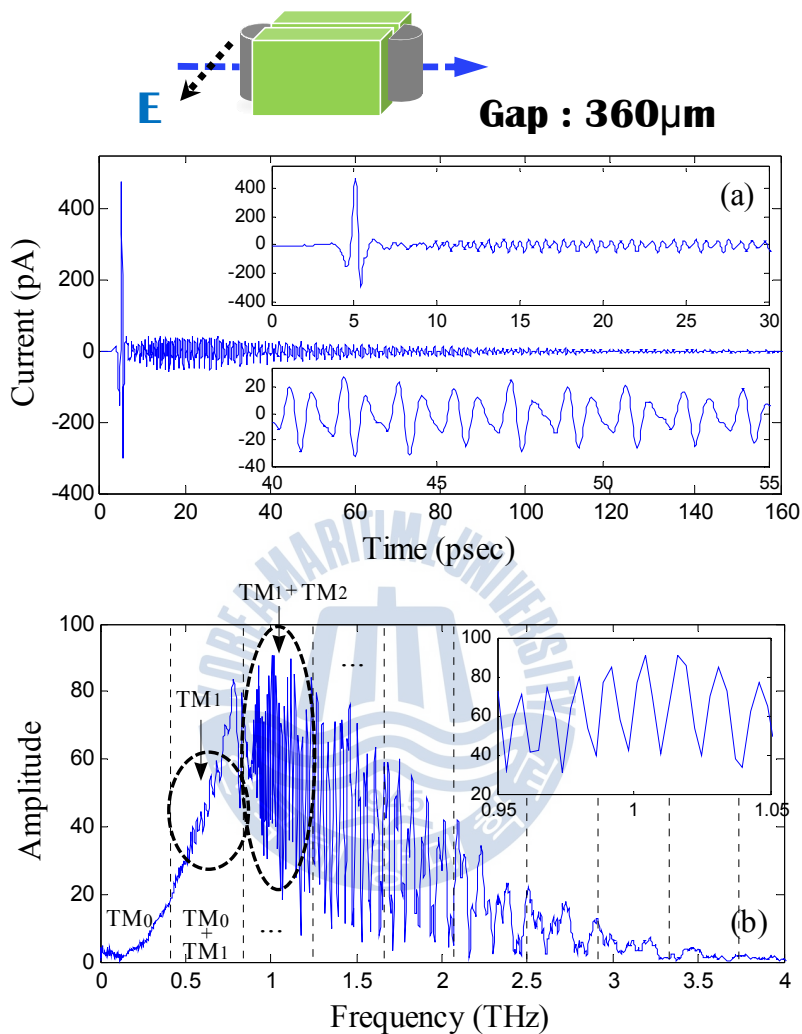
Figure 2.11   Measurement for a parallel-plate at a 360 µm-separation. (a) TM-mode THz pulse in the time domain. (b) Amplitude spectrum of the TM-mode THz pulse. The envelope of the amplitude spectrum indicates the TM_0 mode.

Figure 2.11 shows the measured TM modes for a 360-µm air gap when the waveguide is perpendicular to the THz beam polarization. The first shown THz pulse indicates the TEM mode, and the delayed oscillation pulses indicate higher

TM modes because of their slow group velocities, as shown in the upper inset figure. The maximum amplitude of the oscillations is about 30 pA, which is much smaller than that of the multi-TE mode. The lower inset figure shows the expanded oscillation from 40 psec to 55 psec. The two different-amplitude THz pulses are periodically repeating, which indicates that at least two different TM modes with very low group velocities are propagating. Figure 2.11(b) shows the corresponding amplitude spectrum for the THz pulse. The spectrum clearly shows the TEM (TM_0) mode (envelope of the spectrum) without a cutoff frequency and higher TM modes with a cutoff frequency. The small TM_1 mode, which is an odd field pattern, comes out at 0.42-THz, and the large TM_2 mode, which is an even field pattern, comes out at 0.83 THz.

2.4.2 Experimental Results : multi-TE modes
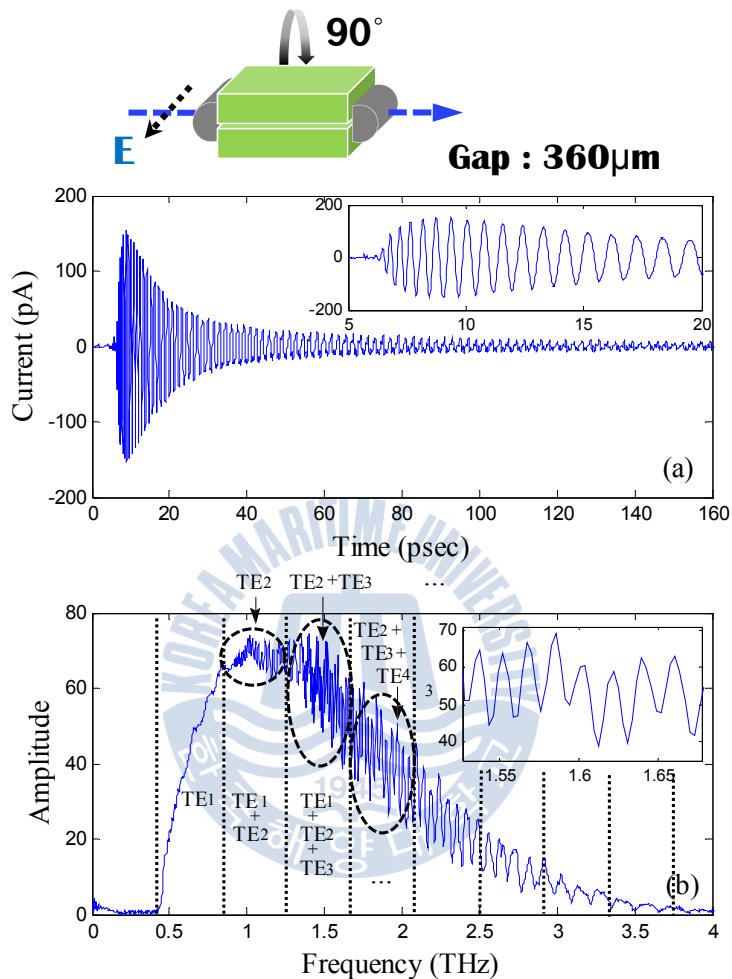
Figure 2.12 Measurement for a parallel-plate at a 360 µm-separation. (a) TE-mode THz pulse in the time domain. (b) Amplitude spectrum of the TE-mode THz pulse. The envelope of the amplitude spectrum indicates the TE_1 mode.

Figure 2.12 shows the measured TE modes for a 360-µm air gap. As explained for the TE mode for a 103-µm air gap, the time domain pulse is stretched to more than 160 psec. Because most of the incoming THz field couples to the PPWG, the maximum amplitude of oscillations is about 160 pA, which is 6 times bigger than

that of a 103-µm air gap. The inset shows the extended figure from 5 psec to 20 psec. The high-frequency oscillation components come first, and the low-frequency oscillation components come next because the group velocity of the low-frequency components is slower than that of the high-frequency components. The spectrum clearly shows a group-velocity delay, as shown in Fig. 2.12(b). The theoretically calculated cutoff frequencies for TE modes are 0.42 THz, 0.83 THz, 1.25 THz, and 1.67 THz from the first to the fourth, as shown by the vertical dash lines in the spectral domain. Due to the evanescent wave before the cutoff frequency, the spectrum of each TE mode comes out after the cutoff frequency. The dominant TE_1 mode starts from 0.42 THz. Most of the spectral energy belongs to the TE_1 mode. The amplitude of TE_2 mode, which is for a 0.83-THz cutoff frequency, is very small because of the odd field pattern. However, the amplitude of the TE_3 mode is relatively large compared with those of the higher-order modes because of the even field pattern and small absorption. Also, the TE_4 mode (1.67-THz cutoff frequency) has a different oscillation frequency than the TE_3 mode. There are a total of 9 modes up to the 4-THz frequency range. Because of high absorption and the slow group velocities, the higher-order modes are difficult to observe in the measured spectral domain.

2.5 Mode analysis

We measured the multi-modes data with a 360-µm air gap. But we can not get the informations what modes and percentages exist each in the signals. So, in this section, using the properties which each modes have the different group velocities, we bring a spectrocronography method to find what modes exist in the signals [42]. And by fitting, we can get what percentages of each modes exist in the pulses.

2.5.1 Spectrocronography
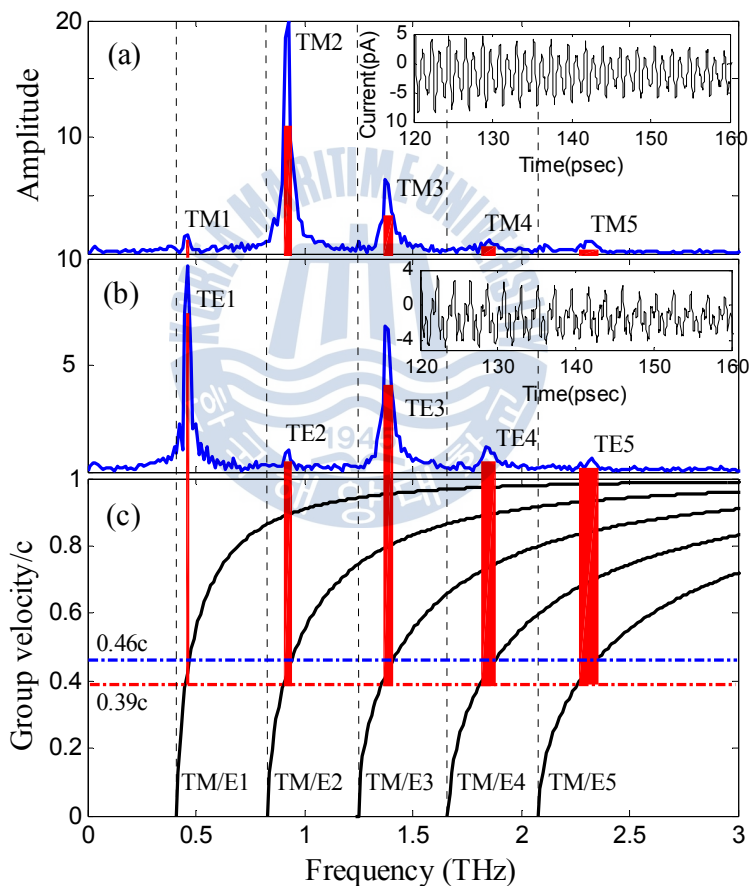
Figure 2.13   Amplitude spectrum of the measured THz pulse from 120 psec to 160 psec (inset) at a 360-µm plate separation: (a) TM modes and (b) TE modes. (c) Group velocities for the first five TM and TE modes. The horizontal dashed lines indicate the velocities for 120 psec (0.46c) and 160 psec (0.39c). The widths of the (red) columns indicate the resonance bandwidths of the spectra.

In order to reveal the major higher-order modes in frequency domain, a spectrochronography method, which an efficient tool to extend the THz time domain technique [42], is used. The insets in Fig. 2.13 show THz pulse data from 120 psec to 160 psec for the TM and the TE modes. The resonance spectra for the limited data are shown in Figs. 2.13(a) and (b). The amplitude of each resonance indicates mode coupling to the waveguide. As explained for the 103-µm air gap, only even field patterns, such as TM_2, TM_4, ⋯ and TE_1, TE_3, ⋯ modes, can be detected on the waveguide. However, there are small TM_1, TM_3, TM_5 modes and TE_2, TE_4 mode components because the system is not perfectly aligned. The alignment of the cylindrical lens to the parallel-plate gap and the alignment of the PPWG to the THz beam propagating through are not complete, small amplitude of odd modes are detected in the data. The odd mode components are very small compared with the signal from the even field pattern. And the amplitude of the TM_3 mode is relatively large compared with those of other odd-mode components, such as TM_1 and TM_5. But the TM_3 component is only 1.52% (in Chapter 2.5.2) for the total time data (see Table 2.1 / p.33). Because the THz pulse of the TEM mode is located at 5 psec, as shown in Fig. 2.11(a), the TEM mode does not show up. The 120 psec and 160 psec correspond to 0.46·c and 0.39·c delays from main pulse of TEM mode, and the delays are indicated to the horizontal dashed lines shown in Fig. 2.13(c). Each resonance bandwidth is determined by the cross section between the group velocity curves and the 0.46·c and the 0.39·c lines. The (red) column indicates this relationship. The column width is small in the low-frequency range because the group velocity curve is much deeper at low frequencies.

2.5.2 Fitting

In the previous section, we could get the existed modes in the pulse. In this section we try to get the energy ratio of each modes. The total detected complex amplitude spectrum, $E_{out}(\omega)$ is obtained from the given complex reference spectrum, $E_{ref}(\omega)$, the transmission and coupling coefficients, the absorption, and the dispersion for each mode to the waveguide. The relationship to the parameters for multi-mode propagation is given by

$$E_{out}(\omega) = E_{ref}(\omega) \sum_m T_m C_m^2 e^{-j(\beta_{g,m} - \beta_0)L} e^{-\alpha_m L} \tag{33}$$

where T_m and C_m are the total transmission and coupling coefficients to the entrance and the exit waveguide, respectively, α_m is the amplitude absorption constant, $\beta_{g,m}$ is the propagation constant and β_0 is the phase constant. The mode- and the frequency-dependent absorption and dispersion have already been shown in Fig. 2.10. Because of the multi-mode propagation to the waveguide, the parameters are mode dependent. Therefore, each mode component should be added to get the detected complex amplitude spectrum $E_{out}(\omega)$. The dashed (red) curves in Figs. 2.14(b) and (d) show the theoretical calculations. There are slight differences between the calculation and the measurement because of the limitation of the measured data. The THz pulse's reflection takes place after 160 psec in the measurement, that is, from reflection of the cylindrical silicon lens. Therefore, the data take until 160 psec, but the multi-mode oscillations go on after 160 psec because of the very low group velocities. However, in the fitting, the periodic oscillation and the relative amplitude in the high-frequency range are well fitted in the frequency domain. Using inverse fast-Fourier transformation, the calculated THz

pulses are fitted well to the measured THz pulses along the time domain. Because of the good fit to the measurements, only expanded scales from 40 psec to 55 psec and from 5 psec to 20 psec for the TM and TE modes are shown in the insets of Fig. 2.14(a) and (c), respectively. In this calculation, the total contributed power in each mode is indicated in Table 2.1. The dominant TE mode is 97.96% TE_1 mode and 1.73% TE_3 mode. The other odd modes or higher modes have very small contributions to the total coupled power. The dominant TM mode is 81.61% TEM mode and 16.23% TM_2 mode. The majority dominant mode is the lowest order mode as TE_1 and TEM (TM_0) modes because of the small absorption.

Mode	0(TEM)	1	2	3	4	5
TM	81.61	0.51	16.23	1.52	0.1	0.03
TE	(%)	97.96	0.16	1.73	0.14	0.01

Table 2.1   Percentage of the coupled power in each mode.
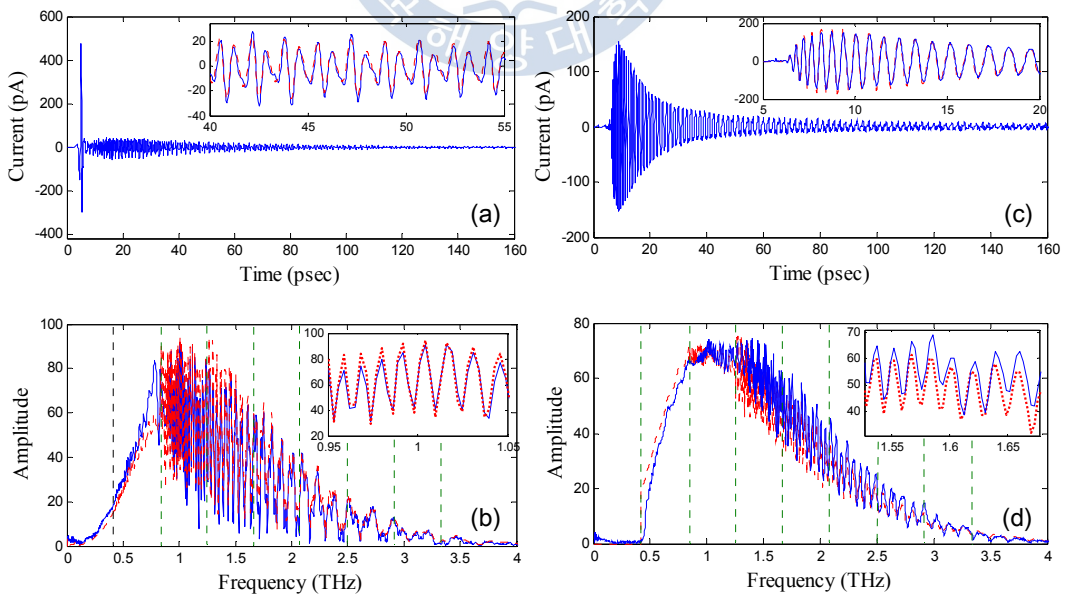
Figure 2.14   (Fig. 2.7 and 2.8.) The dashed (red) curves show the theoretical calculations.

Chapter III.   THz Filter Using the TE_1 Mode of PPWG

In the previous Chapter, we implemented single- and multi-mode THz propagation through a PPWG with the experimental and theoretical explanations. The field will create TE or TM modes depending on the polarization of the incoming field. The cutoff frequencies caused by the gap size of the PPWG exist in the TE and TM modes. And the extreme group velocity dispersion near the cutoff frequency induces the excessive broadening of sub-psec THz pulses. But, THz pulses would not broaden for the TEM modes (known as "TM_0 mode") of the two-wire coplanar line, coaxial line, and PPWG because the TEM mode does not have a cutoff frequency.

In this section, among the various THz guding modes, we will apply the lowest-order TE_1 mode of PPWG for a high pass filter. Fisrt, TEM and higher TM modes are generated via perpendicular polarization between the incident THz beam and PPWG. And then, the generated low-frequency component of the modes are filtered by the TE_1 mode that the THz wave is totally absorbed below the cutoff frequency.

3.1 Experimental setup
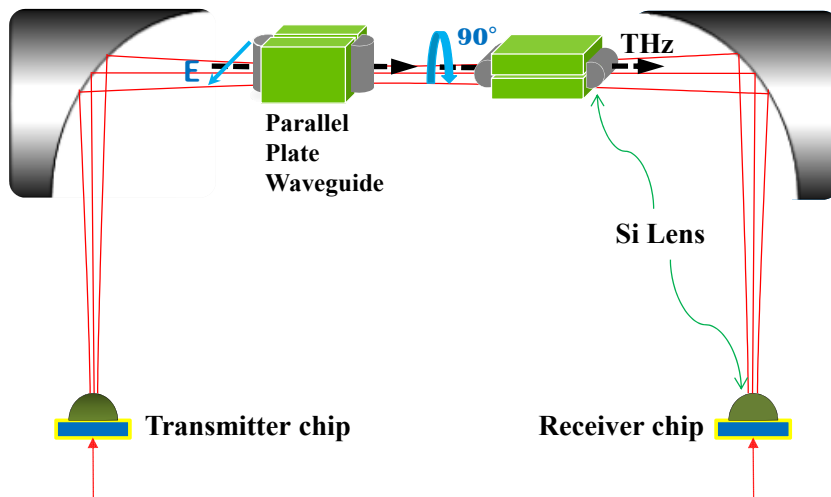
Figure 3.1 Schematic diagram of the THz parallel-plate waveguide system.

Two sets of PPWGs were inserted between two paraboloidal mirrors to generate TM and TE modes, as shown in Fig. 3.1, where the THz wave is horizontal-polarized. Since the cylindrical silicon lens used is 15 mm long, 7.07 mm height, and had a 5 mm radius, only the 15×10-mm cross-section of the THz field was open to the PPWGs. Since much of the THz field energy and most of the high-frequency components were concentrated at the center of the THz beam, the opened cross-section was enough for measurement purposes. The first and third silicon lenses placed the line focus of the incoming THz beam on the gap of the PPWG, and the second and fourth silicon lenses produced parallel propagation to the outgoing THz beam where the size of each PPWG was 29.7×40×10 mm.

The cutoff frequencies of the TM and TE modes are given by Eq. (18) $f_c = \frac{mc}{2d}$, where m is the number of high-order modes, c the speed of light, and d the plate separation of the PPWGs. The first PPWG (with 355 µm plate separation) was set perpendicular to the polarization of the incoming THz wave to generate the TM modes. Therefore, the propagated THz pulse had a TM_0 (TEM) mode with

low loss and negligible group velocity dispersion. The THz pulse also had higher even modes, such as TM_2 and TM_4, with 0.845 and 1.69 THz cutoff frequencies, respectively. As the input pulse had Gaussian field distribution, TM_1 and TM_3, which had odd field patterns, could not be easily coupled. Moreover, the dipole receiver antenna can detect even field patterns; it cannot detect the odd modes in the system.

3.2   Experiment result : TM modes
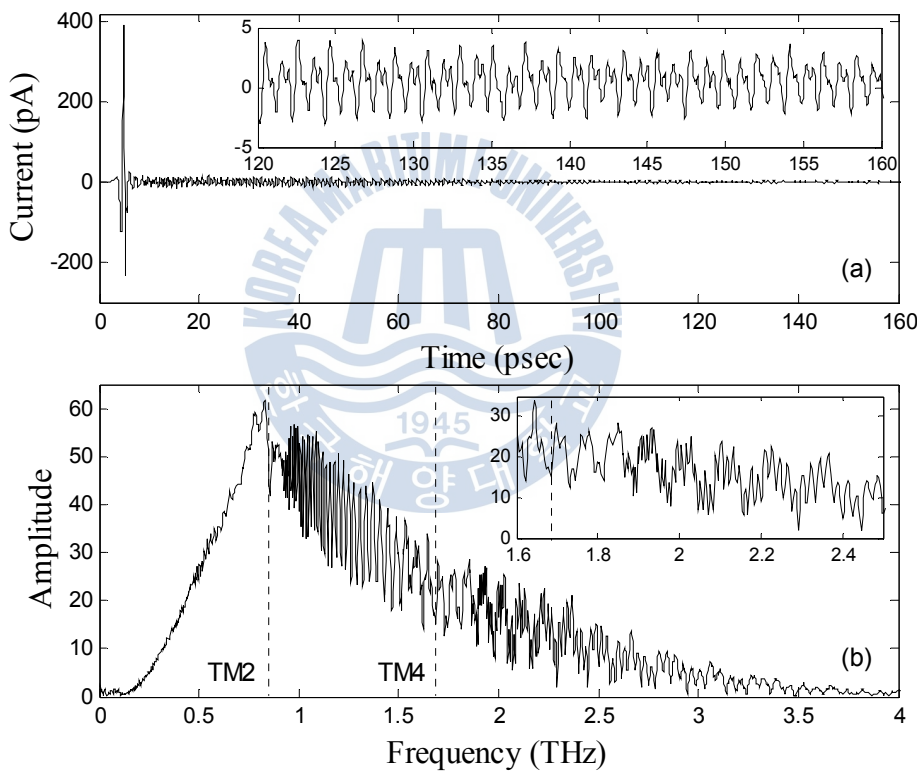
Figure 3.2   Measurements for the TM mode with 355 µm plate separation. (a) TM mode THz pulse in the time domain. The inset shows an extension of the oscillation from 120 psec to 160 psec. (b) Amplitude spectrum of the TM mode THz pulse. The envelope of the amplitude spectrum indicates the TM_0 mode. The inset shows the spectrum from 1.6 THz to 2.5 THz. The cutoff frequencies for the TM modes are indicated by the dotted vertical lines.

Figure 3.2(a) and (b) show the measured THz pulse and spectrum. The first THz pulse shown indicates the TEM mode, and the delayed oscillations indicate higher TM_2 and TM_4 modes because of their slow group velocities. The inset figure shows an extension of the oscillation from 120 psec to 160 psec. The amplitude of each oscillation was continuously reduced with increasing time because the low-frequency components had slow group velocity and a high absorption coefficient. The slow-group-velocity components continually oscillated after 160 psec, but they could not be measured because of the THz pulse reflected from the cylindrical silicon lens. Most of the THz TM modes, however, were within 160 psec. The spectrum clearly shows the modes' components. The envelope of the amplitude spectrum indicates the TEM mode. The TM_2 and TM_4 modes were observed with the oscillation starting at the cutoff frequencies of 0.845 and 1.690 THz, respectively. The TM_6 mode with 2.535 THz cutoff frequency was not clearly shown because of the limited THz beam power. The inset figure shows the spectrum oscillations near the TM_4 mode. The tail part of the TM_2 mode had large periodic repetition while the head part of the TM_4 mode had short periodic repetition starting at the 1.690 THz cutoff frequency. In this study, an attempt was made to remove the signal below 1.5 THz (cutoff frequency), using a TE_1-mode-type high-pass filter.

3.3   Experiment result : TE$_1$ mode
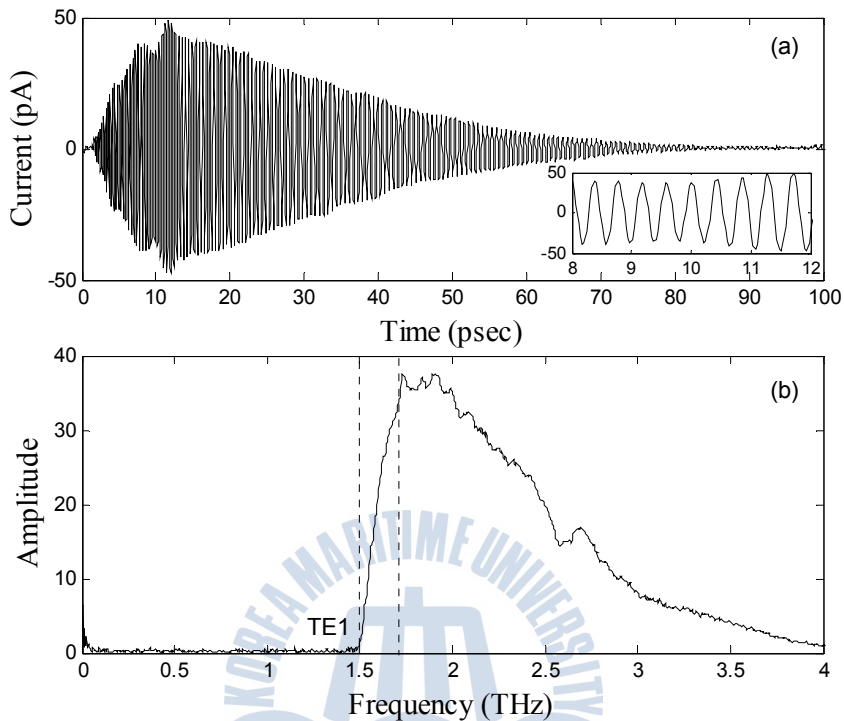
Figure 3.3   Measurements for the TE mode with 100 µm plate separation. (a) TE$_1$ mode THz pulse in the time domain. The inset shows the extension of the oscillation from 8 psec to 12 psec. (b) Amplitude spectrum of the TE$_1$ mode THz pulse.

The second PPWG with 100 µm plate separation was set parallel to the polarization of the incoming THz wave to generate a TE mode that determines the 1.5 THz cutoff frequency for the TE$_1$ mode. Since the TE$_2$ mode (3 THz cutoff frequency) had an odd field pattern, the system cannot be easily coupled and detected. The group velocity dispersion of the TE mode was very high after the cutoff frequency and slowly approached the speed of light with increasing frequency. The high-frequency components of the pulse arrived first, and the low-frequency components after the cutoff frequencies were delayed. Therefore, the

- 38 -

time domain pulse was stretched and expanded to more than 100 psec, with a negative chirp, as shown in Fig. 3.3(a). As there was no TEM component, only the oscillation of the TE_1 mode component was detected in the time domain. The oscillation after 100 psec was ignored because its magnitude was too small compared to the maximum magnitude of the oscillation around 10 psec. The inset figure shows the extension of the oscillation by the group velocity dispersion for the head parts of the oscillation. Figure 3.3(b) shows the spectrum of the time domain THz pulse. The low frequency was truncated at the cutoff frequency, and the spectrum extended up to 4 THz. The spectrum response was a high-pass filter with frequency-dependent gain. The stop-band and pass-band edges were 1.5 and 1.72 THz, respectively, as shown by the dashed vertical lines. Therefore, the transition bandwidth (rising frequency) was about 0.22 THz. The transition bandwidth usually depends on the alignment of the PPWG. Bad alignment of the PPWG has a large transition bandwidth. When PPWG1 and PPWG2 are in a series setting, as shown in Fig. 3.1, the spectrum of the TM mode is filtered by the TE_1 mode.

3.4 Analysis : High pass filter using TE$_1$ mode

The analytic expressions of phase velocity $V_{p,m}$ and group velocity $V_{g,m}$ are given by (section 2.2.5)

$$v_{p,m} = \frac{v_p}{\sqrt{1-(\frac{\lambda}{\lambda_{c,m}})^2}}, \tag{25}$$

$$v_{g,m} = v_p \sqrt{1-(\frac{\lambda}{\lambda_{c,m}})^2} , \tag{27}$$

where $v_p = \frac{1}{\sqrt{\mu\varepsilon}}$ and $\lambda_{c,m}$ is the wavelengths at the cutoff frequency. The speed of light can be expressed as $v_p = \sqrt{v_{p,m}{\cdot}v_{g,m}}$. The magnitude of $v_{p,m}$ in a given mode is infinite at the cutoff frequency because the denominator is zero, as shown in Eq. (25). Moreover, the magnitude of $v_{g,m}$ in a given mode is zero at the cutoff frequency, as shown in Eq. (27). The velocities of $v_{p,m}$ and $v_{g,m}$ before the cutoff frequencies are infinite and zero, respectively, and the velocities approach the speed of light after the cutoff frequencies, with increasing frequency. The combined phase or group velocities for the TM and TE modes can be obtained using the equation

$$v_{p,g,TMTE} = \frac{2{\cdot}(v_{p,g,TM}{\cdot}v_{p,g,TE})}{(v_{p,g,TM}+v_{p,g,TE})}, \tag{34}$$

where $v_{p,g,TM}$ and $v_{p,g,TE}$ are the phase or group velocity for the TM and TE modes, respectively. Fig. 3.4(a) shows the phase and group velocity of the combined TM and TE modes. Fig. 3.4(b), on the other hand, shows the absorption coefficient of the combined TM and TE modes. The vertical dashed lines indicate the cutoff frequency of the TE$_1$ mode. The even modes detected by the first PPWG were TM$_0$, TM$_2$, and TM$_4$, and the odd mode detected by the second PPWG was TE$_1$ until 4 THz bandwidth, whereas v_p and v_g of the TM$_0$ mode were constant at the speed of light. Therefore, the TM$_0$+TE$_1$ mode is the same as

- 40 -

the TE_1 mode, as shown by the thick solid lines, and the other combined components were the even TM modes+TE_1 (TM_2+TE_1, TM_4+TE_1, TM_6+TE_1, etc.), as shown by the thin solid lines in Fig. 3.4(a). The dashed lines indicate the odd TM modes+TE_1 combinations. The combined mode lines diverged farther away from each other with increasing frequency because $v_{p,m}$ and $v_{g,m}$ of TE_1 mode approached the speed of light.
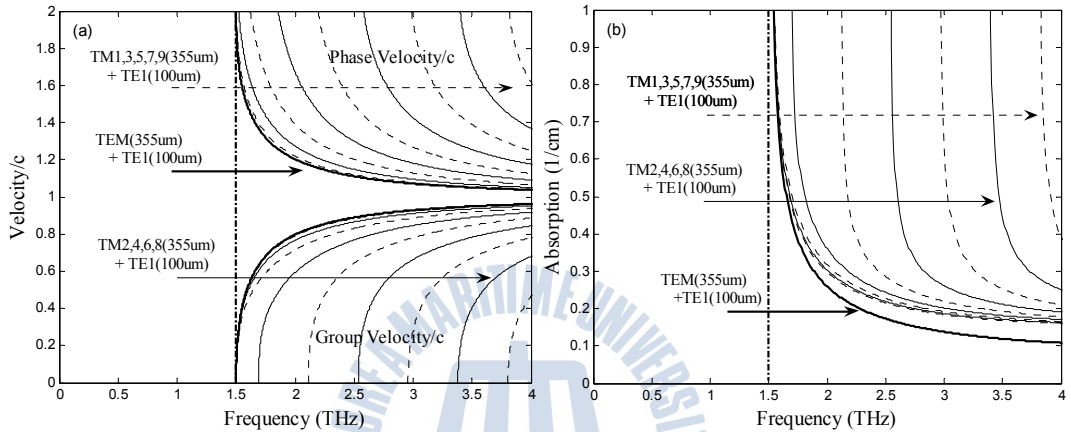
Figure 3.4 Combined TM and TE modes. The dashed curves indicate the combined odd TM modes and TE_1 mode, and the solid curves indicate the combined even TM modes and TE_1 mode. (a) Phase and group velocities for the TM_m+TE_1 modes. (b) Field absorption for the TM_m+TE_1 modes. The cutoff frequency for the TE_1 mode with 100 µm plate separation is shown by the dashed vertical lines.

Since the absorption coefficient of the TE_1 mode was infinite before the cutoff frequency, the combined spectrum with the TM modes was truncated up until the cutoff frequency. The thick solid line in Fig. 3.4(b) indicates the combined TM_0+TE_1 mode. The dashed and solid thin lines indicate the odd and even TM modes combined with the TE_1 mode, respectively. As the absorption coefficient of the TM_0 mode slightly increased with increasing frequency, the margin between the thick solid line and the first thin dashed line also increased with increasing frequency. Since the absorption coefficient of the TE_1 mode after the cutoff frequency slowly decreased, unlike the TM modes, the combined lower modes approached each other.
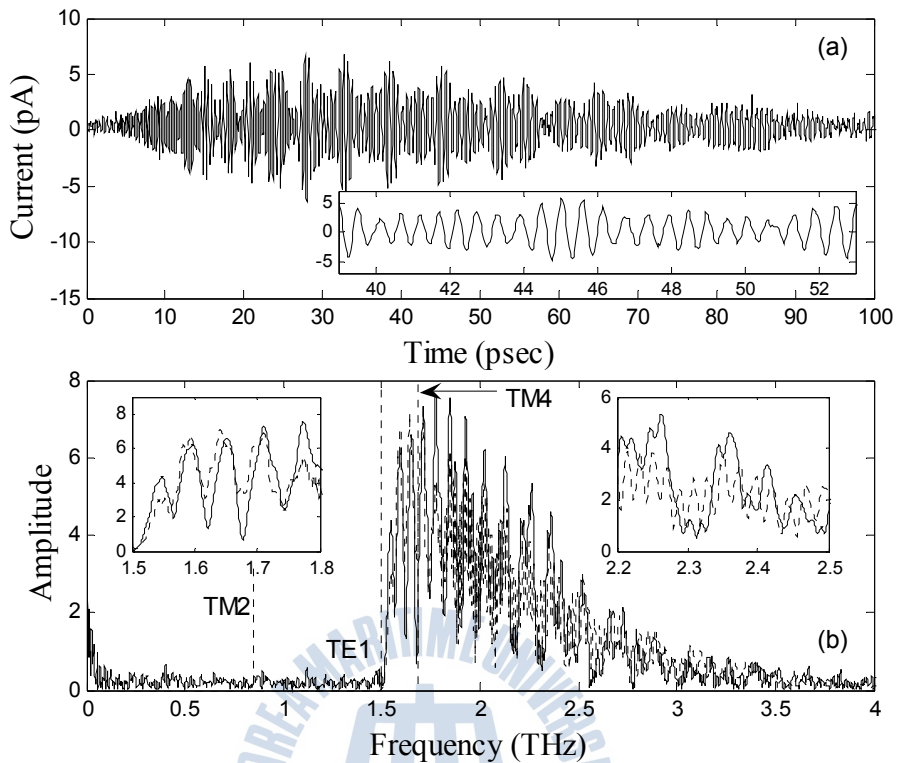
Figure 3.5   Measurements (solid lines) and theoretical predications (dots) for the parallel-plate waveguide at TM_m+TE_1. (a) TM_m+TE_1 mode THz pulse in the time domain. The inset shows an extension of the oscillation from 39 psec to 53 psec. (b) Amplitude spectrum of the TM_m+TE_1 mode THz pulse. The envelope of the amplitude spectrum indicates the TE1 mode. The inset shows an extension of the spectrum from 1.5 THz to 1.8 THz and from 2.2 THz to 2.5 THz.

The THz wave propagated through PPWG1 and PPWG2 is shown in Fig. 3.5(a). The inset shows the extended THz wave from 39 psec to 53 psec. The main THz pulse disappeared, and the amplitude of each oscillation was irregular because of the combination of TM and TE modes. The main THz pulse, which corresponds to the TM_0 mode, went out first from PPWG1 because its group velocity is equal to the speed of light. When the TM_0 mode came into PPWG2, it was converted to

the TE_1 mode. Therefore, the outgoing THz wave from PPWG2 did not have the main THz pulse. Fig. 3.5(b) shows the spectrum that clearly shows the filtering of the low-frequency component. The spectrum was truncated before the cutoff frequency of the TE_1 mode. Part of TM_2 and TE_1 was detected because the cutoff frequency of TE_1 was at the TM_2 mode bandwidth. Moreover, $(TM_2+TM_4)+TE_1$ can be detected by the system.

The spectrum of the outgoing THz wave from PPWG is given by

$$E_{out\,TM_n\,TE_1}(\omega) = E_{ref}(\omega) \sum_{m=0}^{TM_n} K e^{-j(\beta_{g,m}-2\beta_0)L} e^{-\alpha_m L}, \tag{35}$$

where T_m and C_m are the total transmission and coupling coefficient of the entrance and exit waveguides, respectively. The constant $K = T_{TM_m} C_{TM_m}^2 T_{TE_1} C_{TE_1}^2$ parameter was used for fitting. $\alpha_m = \alpha_{TM_m} + \alpha_{TE_1}$ is the amplitude absorption coefficient shown in Fig. 3.4(b). $\beta_{g,m} = \beta_{g,\,TM_m} + \beta_{g,\,TE_1}$ is the propagation constant related to the phase and group velocities shown in Fig. 3.4(a), and β_0 is the phase constant. Using theoretical calculation, the obtained spectrum is shown by the dashed line in the inset figures. The measured oscillated components of the combined modes (after the cutoff frequency) agree well with the calculation result. The amplitudes of the oscillations are not in agreement, though, especially for the high-frequency component, due to the coupling constant. The filtering effect on the spectrum domain was well observed, however, not only in the experiment but also in the theoretical results.

Chapter IV. Bragg resonance of terahertz surface waves in photonic crystals

In the above Chapter, we showed that sub-picosecond THz pulses have been guided between two metal plates using a PPWG. Recently, using a PPWG, THz Zenneck [43] surface wave in THz frequency were demonstrated on aluminum plate so PPWGs are proved as a good coupling tool to generate surface plasmon on metal surface. If the designed photonic crystals are located near the exit of PPWG, the strong interaction between THz SP waves and photonic crystals will happen which results in the Bragg reflection by a sequence of slits. In this chapter, we investigate, experimentally and theoretically, THz surface-bound waves propagating on periodic plasmonic structures such as rectangular and slit apertures. And we successfully measured the reflected *SP Bragg reflection* using PPWGs and estimated the *value of reflection coefficient of each slit*.

4.1 THz surface wave propagation on rectangular aperture arrays
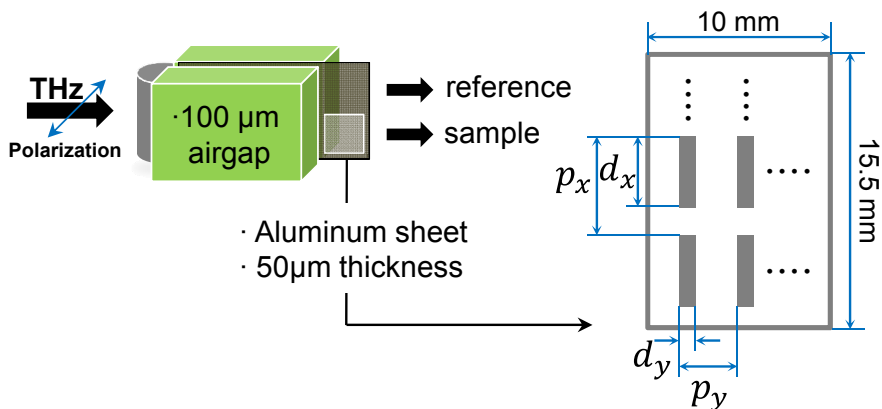
Figure 4.1   Schematic of a PPWG with sample inside.

The experimental apparatus is illustrated schematically in Fig. 4.1. A PPWG is used to couple the air traveling THz pulses on the Al sheet which is located between the two Al PPWG blocks. Figure 4.1 shows the schematic of PPWG which has perforated sample inside a 100 µm air gap. Rectangular aperture arrays on aluminum sheet with a 50 µm thickness can be expressed as *px*, *py*, *dx*, and *dy*. Silicon lens makes THz wave form a line focus to the air gap and THz wave propagates inside the air gap. Near the exit of PPWG, sample is located so THz wave propagates through the samples.

As shown the Table 4.1, the 9 different samples are designed to investigate the effects of THz propagation by each *px*, *py*, *dx*, and *dy* with corresponding lengths.

No.	1	2	3	4	5	6	7	8	9
px	400µm	330	470	400	400	400	400	400	400
py	400	400	400	330	470	400	400	400	400
dx	250	250	250	250	250	200	300	250	250
dy	80	80	80	80	80	80	80	140	200

Table 4.1   Dimensions of each rectangular aperture. Each sample has 20 aperture.

4.1.1 Analysis of the propagated THz waves through samples

• Change in spectrum as the different *px*, *dx* lengths

First, we compared two groups of samples to check the effect of period (*px*) and ratio (*dx*) of rectangular holes in the perpendicular direction to THz propagation. Figure 4.2 show the spectrum of measured THz waves through (a) sample No.1-2-3 to compare the different *px* lengths (period) and (b) sample No.1-6-7 to compare the different *dx* lengths (ratio).

1) All sample have same resonance frequencies, so *px*, *dx* lengths don't seem to affect the resonance frequencies.

2) But peak directions of each resonance are different each other, it looks having the direction of up, down, and up-down ⋯.

3) Amplitude of resonance peak has some trend as the ratio of rectangular aperture (*dx*) to metal surface (*px*). When the ratio is high, most THz wave propagates through rectangular aperture, the peak amplitude becomes high.
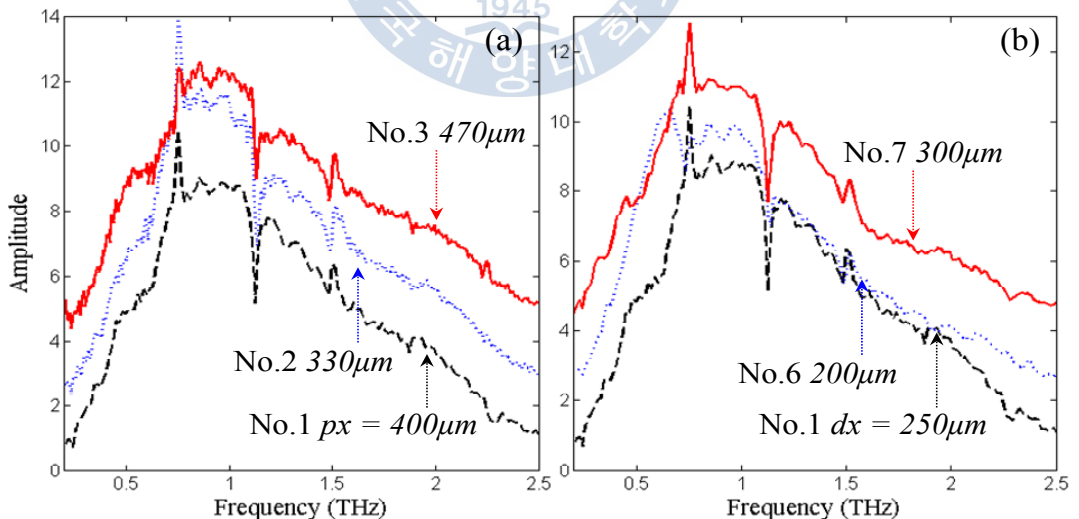
Figure 4.2   Comparison of spectral resonance for different *px* and *dx* in rectangular hole arrays.

• Change in spectrum as the different *py, dy* lengths

Second, we compared two groups of sample to check the effect of period (*py*) and ratio (*dy*) of rectangular holes in the parallel to the direction of THz propagation. Figure 4.3 show the spectrum of measured THz waves through (a) sample No.1-4-5 to compare the different *py* lengths (period) and (b) sample No.1-8-9 to compare the different *dy* lengths (ratio).

1) Figure 4.3(a) shows the different resonance position related with the *py* lengths (period). But it doesn't seem to affect the amplitude of the resonance peak.
2) But Fig. 4.3(b) have same resonance frequencies with the various peak directions but amplitude of resonance peak has the opposite trend compared with *dx* case, which is in inverse proportion to the *dy* lengths (ratio).
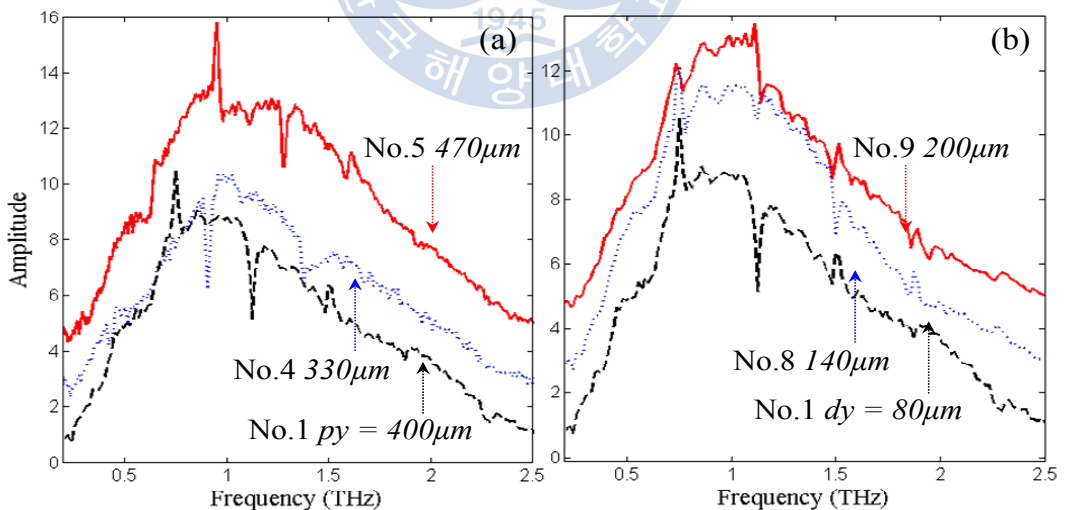
Figure 4.3   Comparison of spectral resonance for different *py* and *dy* in rectangular hole arrays.

4.1.2 Analysis of the resonance phenomenon

In this study, we showed that the resonance phenomenon is generated using the rectangular aperture arrays on metal sheet by the interaction with THz surface wave propagation.

1) Peak amplitude of resonance is affected by *px*, *dx*, and *dy* of rectangular size, except *py*. So, to maximize the peak amplitude, each lengths should be satisfied the following conditions that the ratio of *dx* to *px* lengths is high and *dy* length is small. So, if the rectangular holes arrays change to the slit arrays (ratio is 1) with small *dy* length, peak amplitude can be maximized. (Table 4.2)

2) And only *py* length (period) is related to the resonance frequency which is parallel direction to THz propagation. The peak position is related to the Bragg resonance which is well known, but the direction (shape) of peak is extraordinary. (Table 4.2)

To gain more knowledge about this phenomenon, we accomplish the additional experiment with the precise measurement in the following Chapter 4.2.

	Resonance Magnitude	Resonance Frequency
px	○	
dx	○	
py		○
dy	○	

Table 4.2   The effects of resonance magnitude and frequency as the length of *px*, *dx*, *py*, and *dy* of rectangular hole arrays.

4.2 Bragg reflection of THz surface wave propagation
on slit aperture arrays
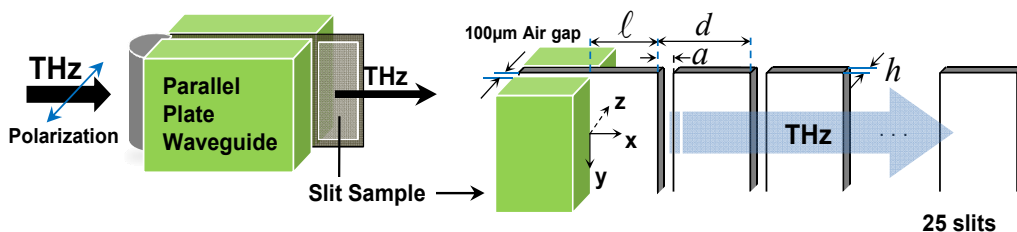
Figure 4.4   Experimental setup and geometry of the slit apertures.

Figure 4.4 shows the schematic of the additional experiment. As mentioned before, to increase the resonance phenomenon and research the arbitrary resonance peak shape, slit aperture arrays is substituted for rectangular aperture arrays.

A PPWG is used to couple the air traveling THz pulses to the Al sheet which is located between the two Al PPWG blocks and generate only TEM mode with a 100-µm air gap. The coming out THz radiation is composed of a free space wave and bounded surface wave (Zenneck wave) on the Al sheet [43]. Most of the free space THz wave propagates close the Al surface, but slowly increasing $-z$ distance as it advances. The distance from the surface at the end of Al sheet to the center of the free space wave is about 3mm by FDTD simulation. Since the most of field intensity of the free space wave is radiated in the air, the free space wave effect was not explicitly considered in analysis. The Al sheet extends outside of the waveguide block. The slit array is located at ℓ = 480 µm away from the edge of the waveguide block, with each slit having a 80 µm width (a), 10mm length (that we consider as infinite), 50 µm thickness (h), and 400 µm slit-to-slit separation (d). The array is comprised by 25 slits perforated in the Al sheet. THz wave moved out propagate on the slit array and radiate into air at the end of Al sheet. The generated THz surface waves propagate on the slit array and radiate into air at the end of Al sheet. Because of the easy coupling of THz surface wave pulses into

freely propagating radiation, these can be detected by the THz time-domain spectroscopy system as shown in the Chapter 1.4.

4.2.1　Measurements and analysis : Numerical fitting
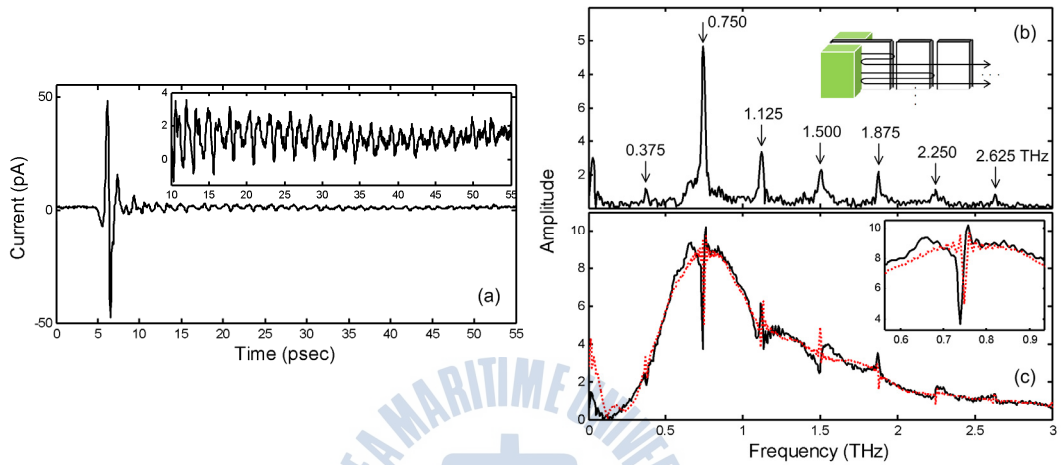
Figure 4.5　(a) THz pulse propagates on 1D array of slits. The inset shows the expanded data from 10 to 55psec. (b) Spectrum amplitude of reflection corresponding to the 10 to 55psec data. (c) Solid line renders the spectrum amplitude obtained using the whole measurement and the dashed red line indicates the theoretical calculation. The inset shows the spectrum expanded at the resonance near 0.75THz.

Measurements of the THz surface waves radiated at the end of the Al sheet are shown in Fig. 4.5(a). The main THz pulse caused by the free space wave and THz surface plasmon (TSP) without slits effect. The well defined oscillation pulses caused by the slits appear after the main TSP pulse. We note that the quasi-period of the long-term oscillation is about 2.66ps, which corresponds to the round-trip time over the array period (400 μm), suggesting Bragg-reflection effects. Indeed, Fig. 4.5(b) shows the Fourier-transform of later-time traces from 10ps to 55ps, displaying now prominent spectral peaks that is spaced by $0.375\,THz \approx \dfrac{c}{2d}$.

The physics behind the appearance of these frequency components is as follows: when the main TSP pulse propagates through a slit, the majority of the THz surface wave pulse keeps travelling along the forward direction while a small fraction is reflected by the slits. The reflected wave travels backward and is then strongly reflected by the waveguide block, again propagating forward. The interference between many of these events leads to the measured spectrum, shown in the inset of Fig. 4.5(b). Thus, the measured THz TSP spectrum can be expressed as

$$E(\omega) = E_{ref}(\omega)[1 + R \cdot e^{-jk2\ell}(\frac{1 - e^{-jNk2d}}{1 - e^{-jk2d}}) + \textit{higher order terms in } R] \quad (36)$$

where $k = \dfrac{\omega}{c}$ and N = 25. R is reflection coefficient of the incoming plane wave by a single slit. Note that $E_{ref}(\omega)$ in Eq. (36) provides a broad spectral background originated from the single-cycle nature of the source field, whereas the $R \cdot e^{-jk2\ell}(\dfrac{1 - e^{-jNk2d}}{1 - e^{-jk2d}})$ term supplies the multiple-resonance features spaced by a frequency interval of $\approx \dfrac{c}{2d}$. The interference of these two contributions results in the multiple Bragg resonance-like features shown in Fig. 4.5(c) that are composed of a maximum and a nearby minimum, very similar to Fano-like features [44]. Up to 55 psec time domain data are used to calculate the spectrum. The background spectrum noisy is from unknown reflected pulses from the THz system especially around 1.2 THz frequency range. It is remarkable the good agreement between the experimental data and the theoretical fitting using Eq. (36), shown in dashed line in Fig. 4.5(c). As R is very small, we neglect the higher order terms in Eq. (36), which describe the reflection by two or more slits. The calculated THz spectrum merits further comments. Through the fitting procedure, ℓ and R can be estimated to be 506 μm and 0.017 ± 0.002, respectively. Note the good agreement between the measured ℓ (480μm) and the fitted result.

4.2.2 Measurements and analysis : Interference phenomenon
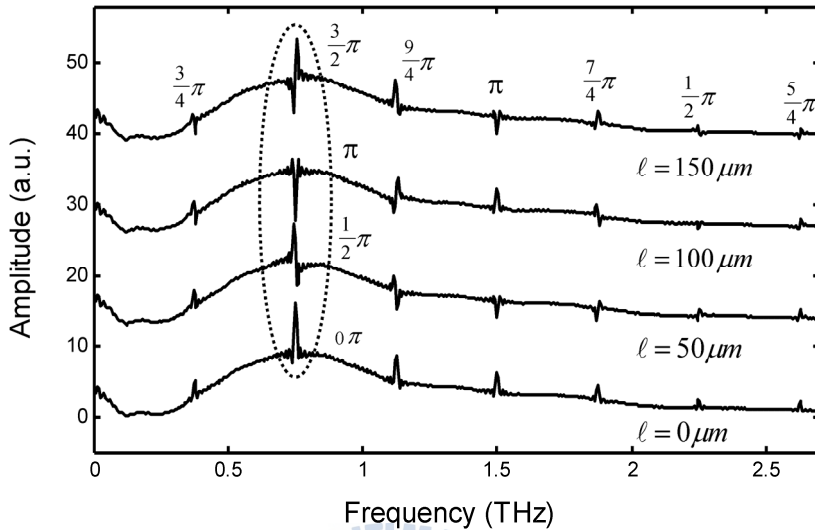
Figure 4.6 Theoretical calculation with different length ℓ for a 400 μm slit period.

The distance between the block and the first slit governs the overall sign of the multiple-path interference term in Eq. (36) through the exponential $e^{-ik2\ell}$. In order to show the role played by this parameter, we display in Fig. 4.6 the field amplitude obtained from Eq. (36) for R = 0.017 with different ℓ. The measured THz spectrum without the slits in the Al sheet is used for $E_{ref}(\omega)$. The numerator (e^{-iNk2d}) of Eq. (36) corresponds to small oscillation near the resonance. Therefore the background spectral noise shows up in the spectrum. The phase of the resonances depends on the resonant wavelength and ℓ. It is important to note that when ℓ is set to 0, all the resonances have the same sign (constructive interference as shown in bottom panel of Fig. 4.6). As we increase the length by 50 μm intervals, Fano-like features indeed appear. At 0.75 THz (λ=400 μm), indicated by a dashed circle in the figure, each increment of ℓ in 50 μm leads to a resonance phase shift of π/2. When ℓ is equal to 150 μm (top of Fig. 4.6), the phase of each resonance relative to the background depends on the frequency, and therefore,

- 52 -

each resonance displays distinctive features. The broad background band is needed to display not only the constructive interference but also the distinctive interference.
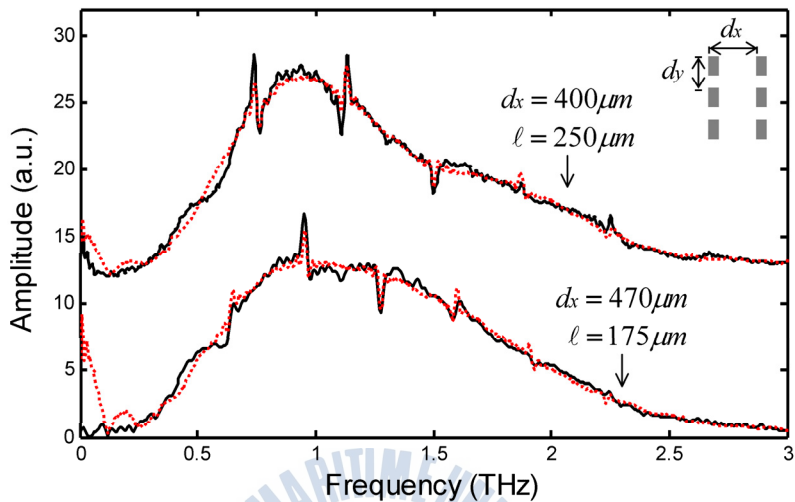
Figure 4.7   Comparison of spectral resonances for different ℓ and d in rectangular hole arrays. Solid and dashed lines indicate experimental and theoretical results, respectively.

We now discuss similar spectral features in THz waves propagating on rectangular hole arrays. When THz surface waves travel along a periodic arrangement of rectangular holes, the Bragg reflection induced Fano-type spectral features are also observed as shown in Fig. 4.7. The holes are 80 µm-width and 250 µm-length, and the thickness of the sheet is 50 µm. The upper panel shows the spectrum for a hole array whose period along the direction of propagation is dx = 400 µm and along the transversal direction dy = 330 µm. The lower spectrum corresponds to another sample with dx = 470 µm and dy = 400 µm. The lengths ℓ of the upper and the lower spectra are 250 µm and 175 µm, respectively. The dashed lines indicate calculated spectra showing good agreement with experiments. As a result of the fitting of our experimental data, we find that the reflection coefficient, R, of a single aperture (for both slits and rectangular holes) is also equal to 0.017 ± 0.002.

4.2.3 Theoretical calculations of the reflection coefficient
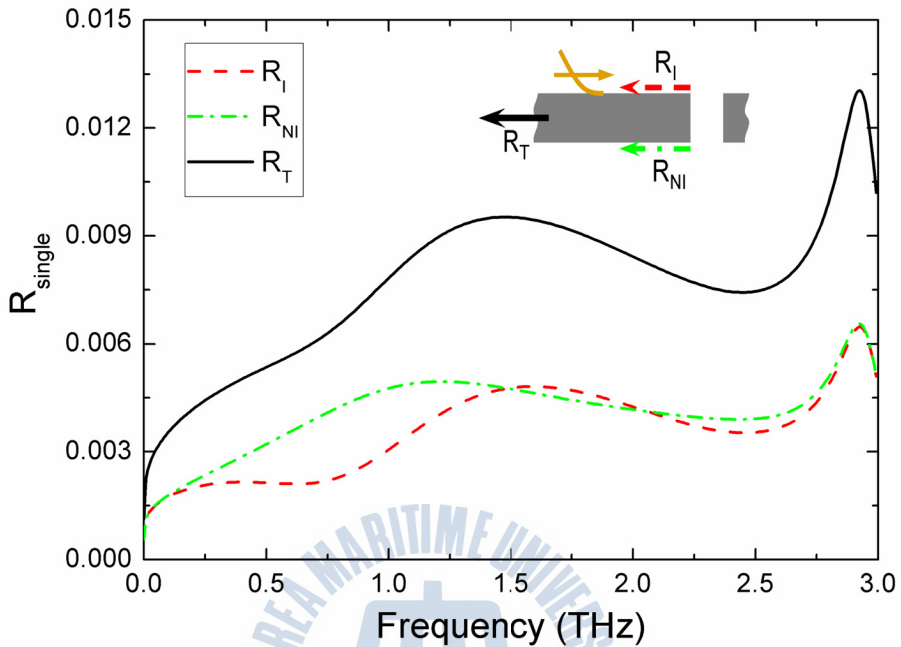
Figure 4.8   Modulus of the reflection coefficients calculated with the modal expansion technique. R_I and R_{NI} denote the reflection coefficients for the illuminated and nonilluminated faces of the aluminum sheet, respectively. R_T is defined as the sum of the modulus of R_I and R_{NI}.

In order to check the value of R obtained from the fitting of our measurements to Eq. (36), we have carried out modal expansion calculations [45] of the scattering of THz SSPs by a single slit with the same geometry as considered in the experiments. The dielectric properties of the aluminum sheet are modeled through the surface impedance boundary conditions [40], which are an excellent approximation at THz frequencies. Two distinct coefficients are calculated, R_I and R_{NI} (see input Fig. 4.8), which describe the reflection of the SPPs at the illuminated, and non-illuminated side of the sheet, respectively. Figure 4.8 renders the modulus of these two reflection coefficients as a function of frequency within

Collection |

the spectral range considered in the experiments. We have introduced another magnitude, R_T, which is defined as the sum of the modulus of the previous coefficients. R_T can be compared with the experimental value for R, as radiation coming from both sides of the film contributes to the signal measured in the far-field. Note that the reflection coefficient in Fig. 4.8 shows a strong peaked feature at 2.8 THz. It is associated to the formation of Fabry-Perot like resonances inside the slit and along its depth. To a first approximation, the lowest resonant frequency is given by $f = c / 2h = 3.0$ THz , which is in good agreement with the spectral location of the maximum obtained through modal expansion calculations. It is also remarkable the reasonable agreement between the measured frequency independent reflection coefficient and the theoretical spectrum shown in Fig. 4.8. The small discrepancy between the two magnitudes can be due to the approximations performed in Eq. (36), which does not take into account aspects such as higher order reflection waves, the coupling of through the slits, or the scattering out of plane of the TSP at the PPWG blocks.

We finally note that the sample parameters reported here are not conducive to observe strong features of designer surface plasmons. Due to the fact that the metal films considered in this experimental study are extremely thin, the flat part of the dispersion relation of the designer surface plasmons appears at very high frequencies and, therefore, the propagation characteristics of the TSPs are dominated by diffraction effects. Nevertheless our experimental and theoretical study provides the solid existence of Bragg reflections which will, with further analyses varying the geometrical parameters, lead us to observe more striking features in the future.

Chapter V.   Improvement of THz coupling
using a tapered parallel-plate waveguide

In general, to achieve the TEM mode, the air gap between the two parallel plates must be less than 100 µm if the bandwidth is about 3 THz, which is also the cutoff frequency of the TM_2 mode. Because the plate separation is very small, plano-cylindrical silicon lenses are attached to the input and output side of the PPWG to create a line focus and to propagate the THz wave to the air. Because of the high refractive index of the silicon (n = 3.412), however, about 30% THz beam is reflected from each lens (Fresnel transmission, $\simeq$ 0.7). Consequently, there is about a 50% total loss from the two silicon lenses. This reflection loss induces a low coupling efficient. Recently, large plate separation at a scale of a few millimeters has been studied to achieve the transverse-electric (TE_1) mode without using silicon lenses. A high THz energy concentration in a hundred-micron plate separation of the PPWG is still attractive, however, for many useful applications.

To concentrate freely propagated electromagnetic beams, tapered-structure waveguides were used in the microwave [46,47] and X-ray [48] regions. Recently, numerical simulations have shown that micro-nano-size tapered waveguides can concentrate THz energy and improve the spatial resolution and the signal-to-noise ratio [49]. Also, THz quantum cascade laser operating with a micro-TEM-horn emitter antenna has been demonstrated [50,51]. An adiabatically compressed parallel-plate metal waveguide was used to enhance the sensitivity of waveguide THz time-domain spectroscopy [19]. In this chapter, we report a TPPWG without silicon lenses which have a higher THz coupling efficient than PPWG, using experimental and theoretical calculations.

5.1 Experiment setup : Tapered waveguide specimen
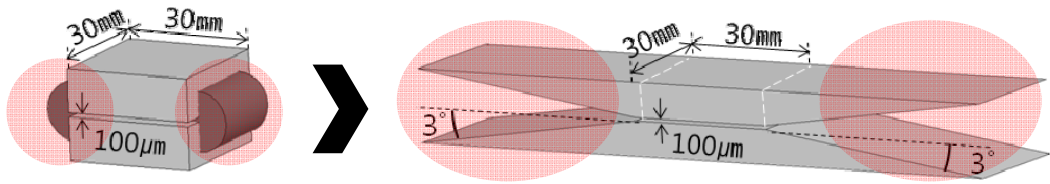
Figure 5.1   Schematic of a PPWG with Si lenses and tapered PPWG.

The waveguides were set up in the middle of two parabolic mirrors as described in chapter 1.4. All the waveguides used in this research were made of aluminum. Also, a computer numerical controlled end mill was used to make tapered structures of the waveguides as shown in Fig. 5.1. The incoming THz beam was vertically polarized, and the waveguides were horizontally set up to achieve the TEM mode with 100 µm plate separation. All the waveguides that were used in the experiment had the same flat plate dimensions of 30 mm (width) × 30 mm (length). The high-resistivity plano-cylindrical silicon lens of the input side formed a line focus to the incoming THz beam along the plate separation. Since the 1/e amplitude of the line focus at the beam waist was about 200 µm, the entire THz beam could not couple to the waveguide gap. Moreover, there was a reflection loss from the silicon lens surface.

5.2　Experiment results : One-sided TPPWG with the different angles
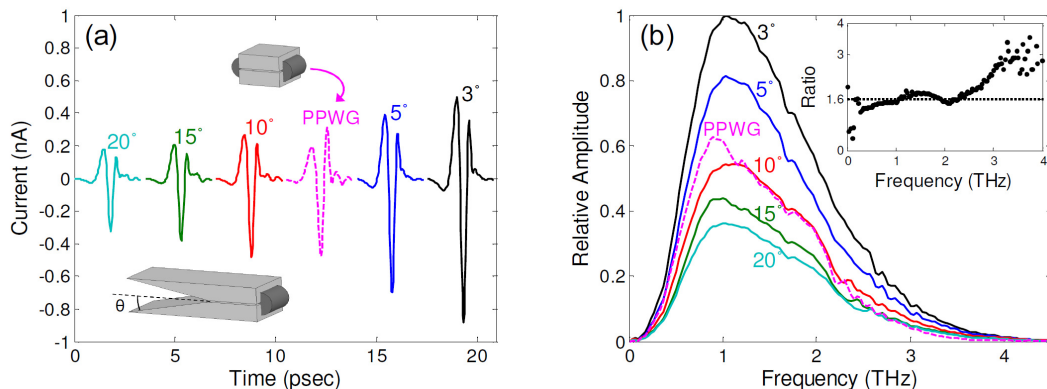
Figure 5.2　(a) Measured THz pulses of the TPPWG with different slop angles, and dotted THz pulses for the PPWG. (b) Corresponding amplitude spectra for the THz pulses. The inset shows the amplitude ratios of the PPWG and the 3° TPPWG.

To prevent reflection loss and to concentrate the THz beam on the air gap of the plate separation, the structure of the input side of the PPWG was changed into a tapered structure (a one-sided TPPWG), as shown in the Fig. 5.2(a). The incoming THz beam was guided by the tapered structure and naturally formed a line focus to the air gap, as did the plano-cylindrical silicon lens. The five different slop angles of the tapered part—i.e., 20°, 15°, 10°, 5°, and 3°—were used to get the THz pulses. Therefore, the opening angle of the TPPWG was twice the slop angle, and the length of the tapered part increased with the decrease in the angle to retain the input cross-section. Figure 5.2(a) and (b) show the measured THz pulses and their spectra for the TPPWG and the PPWG. The peak-to-peak amplitude of the THz pulse at the 3° slop angle was 1,380 pA, which was about three times bigger than that of the 20° slop angle. The peak-to-peak amplitude of the PPWG was 788 pA, similar to that of the 10° TPPWG. The spectrum bandwidth extended to almost 4 THz for both waveguides. Moreover, the spectrum of the PPWG was

similar to that of the 10° TPPWG. The inset in Fig. 5.2(b) shows the amplitude ratio between the PPWG and the 3° TPPWG. The spectrum amplitude of the 3° TPPWG at 1 THz increased about 60%, unlike that of the PPWG. As the slop angle of the TPPWG decreased, the amplitudes of the THz pulses were enhanced. Had the slop angle been smaller than 3°, the measured THz pulse would have been enhanced more. In such a case, however, the length of the TPPWG would dramatically increase to retain the cross-section for the input THz beam.

5.3 FDTD simulations and measurements : Round and non-round TPPWG
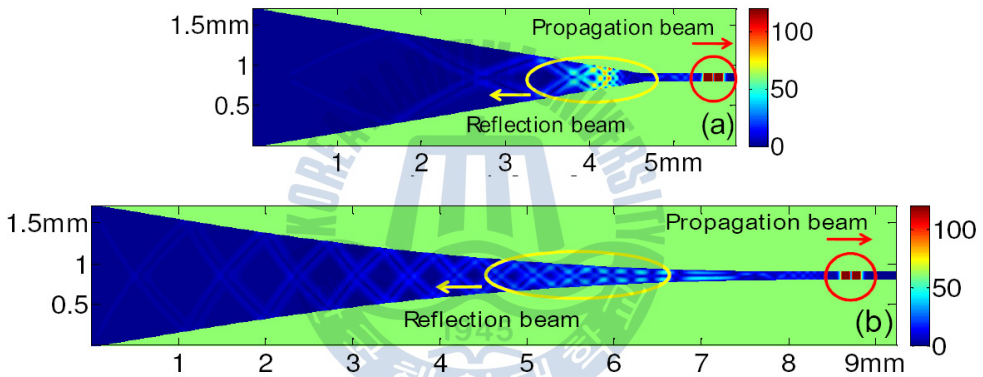
Figure 5.3 Calculated input-side magnitude of THz field distribution. (a) 10° non-round TPPWG. (b) 10° round TPPWG with an 80mm-diameter circular arc.

When the THz beam was propagated on the metal surface, the discontinuous boundary surface engaged its reflection. The discontinuous boundary between the tapered and flattened surfaces also engaged the THz reflection. To reduce the reflection, the discontinuous boundary made a continuously changing surface (round) with an 80 mm-diameter circular arc, wherein the area of the flat surface kept identical to that of the TPPWG. If the circular arc is getting large, the length of the waveguide should be dramatically long to keep the same input cross section. Therefore, the 80mm-diameter arc round taper was chosen to optimize waveguide

length and to remove the discontinue boundary. In this study, the magnitude of electric field propagation of 10° TPPWG with and without a round taper was calculated via FDTD numerical simulation, as shown in Fig. 5.3. The linearly polarized THz pulses, wherein central frequency was 1 THz, were modeled as a plan wave with a magnitude of electric field that was incidence in perpendicular to the beam propagation. The waveguide blocks are defined as perfect electrical conductors with a mesh size of 1×1 µm. Because of the limited computer memory size, the width of both opened tapers was only 1.71 mm. However, the important round part was covered in the simulation. The reflected THz field from the discontinuous boundary was stronger than that of the continuous boundary (round). The figures show that the strong main magnitude of THz fields were in the parallel plate gap and went forward, and that the reflected THz waves were in the tapered area and went towards the backward direction. To clearly show the reflected THz beam, the maximum magnitude of the field bar was shown as only 120. Therefore, the THz field in the parallel plate gap was saturated with the maximum magnitude. The maximum magnitude of THz field in the parallel plate gap without the saturation were 292 and 276 for the round and non-round TPPWG, respectively. Because of the continuous boundary (the round tapered surface), the THz field coupling to the parallel plate gap was bigger than that of the discontinuous boundary, and it had a small reflection loss.
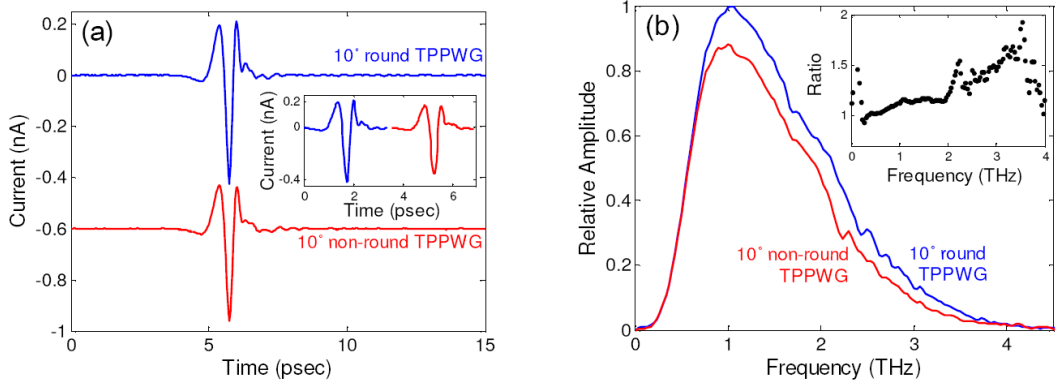
Figure 5.4   (a) Measured THz pulses for the 10° round TPPWG (upper pulse) and the 10° non-round TPPWG (lower pulse). The inset shows the comparison of the pulses. (b) Corresponding amplitude spectra for the THz pulses. The inset shows the amplitude ratio.

The measured THz pulses and spectra of the 10° round TPPWG and the 10° non-round TPPWG are shown in Fig. 5.4. The peak-to-peak THz pulse of the round TPPWG increased about 15%. The spectrum of the 10° round TPPWG was also enhanced in the measured bandwidth. The inset in Fig. 5.4(b) shows the spectra ratio. The round TPPWG was enhanced by about 13 % at the 1 THz frequency. The spectrum of the round TPPWG improved in the high frequency range. Only the 10° round and non-round TPPWGs were measured because the smaller tapered slop angle, especially 3°, had almost the same THz field in simulation for the round and non-round TTPWG.

5.4 FDTD simulation : Output tapered structure for two-sided TPPWG
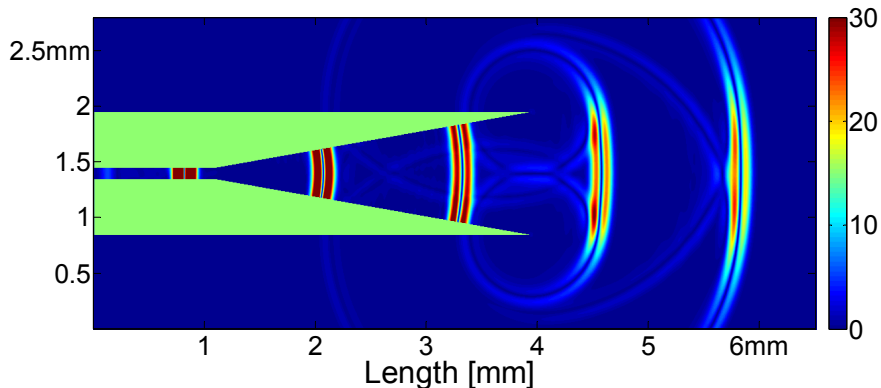
Figure 5.5   Calculated the magnitude of THz field propagations to the air by the output tapered structure at a 10° angle. The magnitude of THz field shows by a snapshot every 1.25 mm period.

Figure 5.5 shows the magnitude of THz field propagations to the air by the output tapered structure at a 10° angle. The continuous propagating magnitude of THz field shows by a snapshot every 1.25 mm period to the propagation direction. The THz field was well guided by the tapered surfaces in the inner area, in the same way the input side was. After this, much of the THz field was propagated to the open air at the same speed. There was only a slight refraction at the edge of the tapered structure. Because the output tapered structure operated as a cylindrical silicon lens, the output-side silicon lens of the TPPWG was replaced by the tapered structure. Therefore, the coupling of two-sided TPPWG will be enhanced by the structure since no silicon lenses are needed.

5.5 Measurements and analysis : Two-sided TPPWG
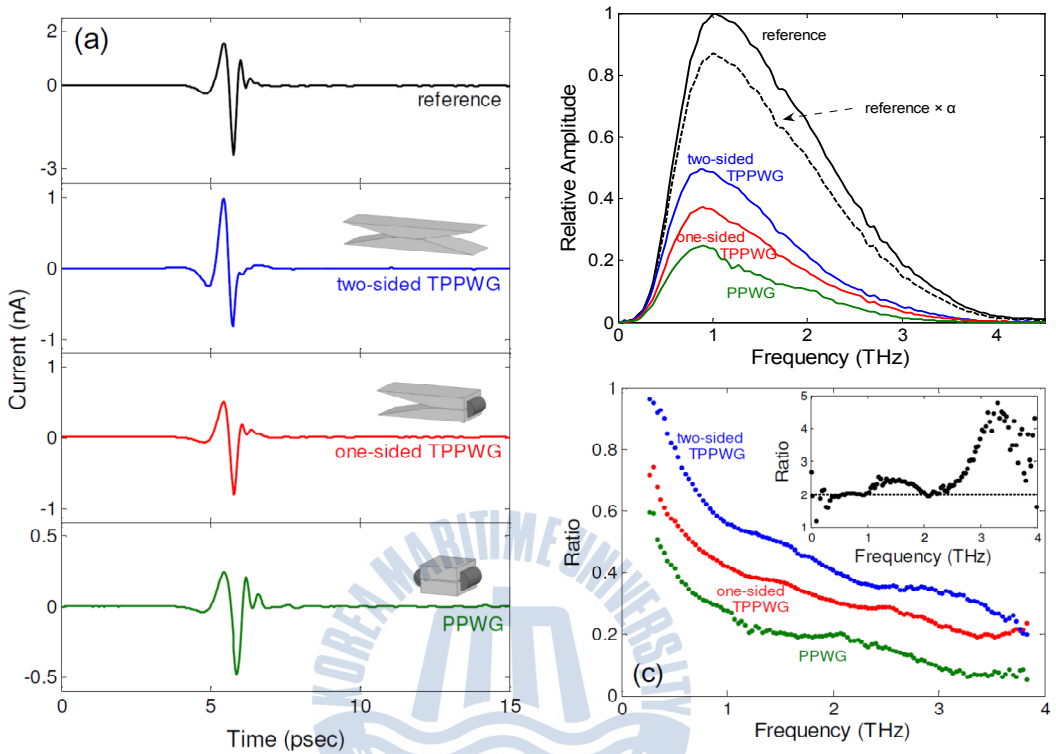
Figure 5.6   Comparison of the PPWG and the one-sided and two-sided TPPWGs with 3°
slop angles. (a) Measured THz pulses. The measured reference pulse is shown in the
upper pulse. (b) Corresponding amplitude spectra for the THz pulses. (c) The amplitude
ratios of reference $\times$ α and the measured spectra. The inset shows the amplitude ratios
of the PPWG and the two-sided TPPWG.

Figure 5.6(a) compares the PPWG with the cylindrical silicon lens and the
one-sided and two-sided TPPWGs with a 3° slop angle. The THz pulses obtained
by the waveguide were time shifted for comparison. All the waveguides had 100-μ
m plate separations and lengths of 30-mm, 90-mm, and 180-mm total, in order to
retain the THz input cross-section. The peak-to-peak THz amplitude of the
two-sided and one-sided TPPWGs improved by 138% and 38%, respectively,

compared to the PPWG. Since the two-sided TPPWG had almost no impedance mismatch between the freely propagating wave and the guided wave, most of the freely propagating THz wave coupled in and out of the TPPWG gap. The reference pulse shown in the upper pulse in Fig. 5.6(a) was obtained by removing the waveguides. In other words, the THz beam went through an aperture only. The reference spectrum had the biggest amplitude, as shown in Fig. 5.6(b).

The frequency-dependent absorption for the TEM mode is given in the following equation [41]:

$$\alpha = \frac{1}{d}\frac{R}{\zeta} \tag{30}$$

wherein d is the gap between the parallel plates, R is the characteristic resistance, and ζ is the intrinsic impedance of the medium (air). The calculated absorption constant was 0.092 cm^{-1} at the 1 THz frequency. When the THz pulse was propagated to the parallel plate area (3 cm long) with the 100-µm air gap, a 13% attenuation loss at the 1THz frequency was observed. The dashed spectrum in Fig. 5.6(b) shows the new reference spectrum for the measured frequency range with neglected the attenuation loss by the 3 cm long parallel plate area.

Therefore the new reference spectrum indicates 100% coupling to the waveguide. When the attenuation loss is neglected, the two-sided TPPWG, the one-sided PPWG, and the PPWG recorded a coupling of 56%, 42%, and 27% at 1 THz, respectively as shown in Fig. 5.6(c). The inset figure shows the improved ratio with the use of the two-sided TPPWG over PPWG. Coupling of the two-sided TPPWG improved the measured frequencies by over 100%, unlike the cylindrical silicon used in the PPWG. It is expected that the strong THz signal will be useful for many PPWG applications including sensing and spectroscopy.

Chapter VI.　THz band gap properties
by using metal slits in TPPWG

In Chapter III, we showed the interaction with THz propagation and photonic crystal structures of rectangular and slit aperture arrays perforated on metal sheet placing outside PPWG. And Chapter IV explored the PPWG structure to increase the coupling efficiency and to make a PPWG setup easy which results in the tapered structure. In this Chapter V, our studies are carried out by using metal slit arrays positioned at the center of the air gaps in TPPWGs. This 1-D photonic structure induces several interesting band gaps which have the different origin in forming mechanism, whereas Chapter III showed only the effect of Bragg reflection. We analysis the *properties of induced band gaps* by experimental and FDTD simulation studies.
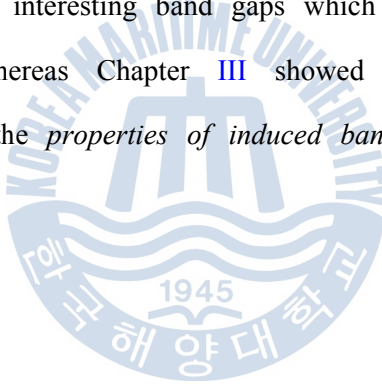
6.1 Experiment setup
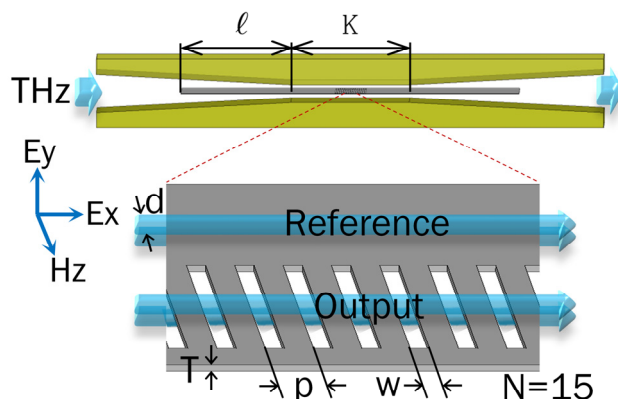
Figure 6.1   Diagram of TPPWG and slit sample.

The experimental setup is illustrated schematically in Fig. 6.1. The stainless steel slits have width w=60 µm, period p=150 µm, and thickness t=30 µm where the propagated THz beam width on the slits is d=5 mm. The slits are made by micro-photochemical etching. The total number of slits is 15 and the total length of the stainless steel sheet is 20 mm. The slit surfaces are separated from the upper and lower plates of the waveguide, which maintain a constant air gap (g). We uesd two different air gaps, g=29 µm and g=94 µm, to study the properties of Bragg and non-Bragg band gaps. As shown in Fig. 6.1, the slits are installed on only one side. As the waveguide is moved a unit in the z direction, the reference and output THz pulses can be detected without any optical or mechanical adjustment. The angle of the tapered part is 3°; it has twice the coupling coefficient of the cylindrical silicon lens used in PPWG (Chapter 5). Moreover with no silicon lenses in the waveguide, multiple reflections are eliminated from the measurement. The total length of the flat surface of the TPPWG is k=6 mm. The protruded length of the stainless steel sheet in the tapered part is ℓ =7 mm, and this can separate the incoming THz beam into two parts. Although the stainless steel sheet is located at the vertical center of the incoming THz beam, the measured spectrum has no

distortion. This is because of the thickness of the metal sheet and because the THz beam is not fully focused at the beginning of the protruded sheet. Since the polarization of the incoming THz beam is perpendicular (y-direction) to the slit surface, only TM modes exist.

6.2   Experiment results
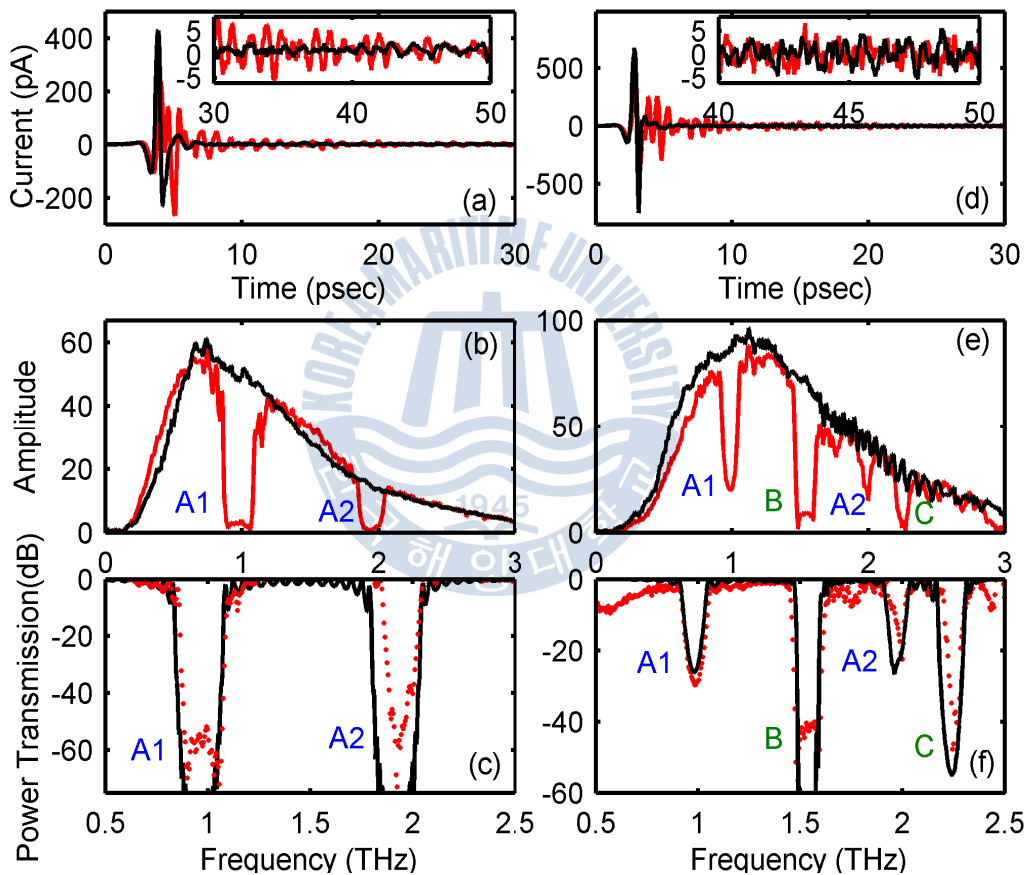
Figure 6.2   (a) Reference (black line, without slits) and output (red line, with slits) THz pulses for a 29-µm air gap. (b) Amplitude spectra of the reference and output. (c) Comparison of power transmission spectrum between measurement (dots) and FDTD simulation (solid line). (d), (e), and (f) are the same as (a), (b), and (c) but for a 94-µm air gap.

Measurements of THz pulses with 29-µm and 94-µm air gaps are shown in Figure 6.2(a) and 6.2(d). The inset in each figure shows the ringing structure caused by the slits. The measured pulse trains have been truncated to about 66 ps in the measurement. Because of a high order mode, the inserted reference signal of Fig. 6.2(d) shows a larger ringing signal than that seen in Fig. 6.2(a). The reference spectrum shown in Fig. 6.2(e) has oscillation from about 1.59 THz, which indicates the cutoff frequency of the TM_1 mode. The generated reference and output TM_1 modes by the upper and lower symmetric air gaps are coupled at the exit end of the stainless steel sheet. Therefore, the receiver can detect the coupled signals. The magnitude of the TM_1 mode has little effect on the result because of its small amplitude. Also, the output spectrum has the same TM_1 mode. Figures 6.2(b) and 6.2(e) show the spectra of each measured THz pulse. The upper black curves indicate the reference pulse spectrum without slits on the stainless steel sheet. Although the reference and output samples are one unit, there are system errors to the measured signals, especially the small air gap measurement. In addition, the attenuation of reference, which has two 29-µm air gaps, is bigger than that of the output, which has an 88-µm air gap between two waveguide plate surfaces. Therefore, the reference amplitude is lower than the signal amplitude in some frequencies at the 29-µm air gap. Because of the very small amplitude of the output signal at the stop bands, the power transmission of the stop bands (A1 and A2) is noisy as shown in Fig. 6.2(c). Because of the periodic slit array, the Bragg stop bands are given by $f_{Bragg} = (m \cdot c)/(2 \cdot p)$, where c is the speed of light and m is an integer. For a 150-µm slit period, the Bragg stop bands (A1 and A2 in the figures) occur at 1 and 2 THz for m=1, 2 as shown in Fig. 6.2(b) and 6.2(e). Figure 6.2(e) shows not only the Bragg stop bands but also the non-Bragg stop bands (B and C in the figure). The stop bands are clearly observed from the power transmission as shown in Figs. 6.2(c) and 6.2(f). The dots and solid line

indicate the experimental and FDTD simulation results, respectively, and the results are in good agreement. When the air gap is small, the electric field strongly couples between the waveguide plates and the slit surfaces. Therefore, the dynamic ranges of the Bragg band gap become strong (and form a stop band). When the air gap increases, the reflected THz beam from each slit becomes small and forms a weak band gap. The dynamic range of the power transmission of the A1 Bragg stop band at the 94-µm air gap is reduced to approximately 12.5 dB as shown in Fig. 6.2(f). The dynamic range decreases with an increase in the air gap, which means that the THz beam propagated to the exits also increases. However, the dynamic ranges of the non-Bragg stop bands are stronger than those of the Bragg stop bands as shown in Fig. 6.2(f). To understand the properties of the Bragg and non-Bragg stop bands, we performed FDTD simulations.

6.3 FDTD simulations : A1, A2 - Bragg stop band
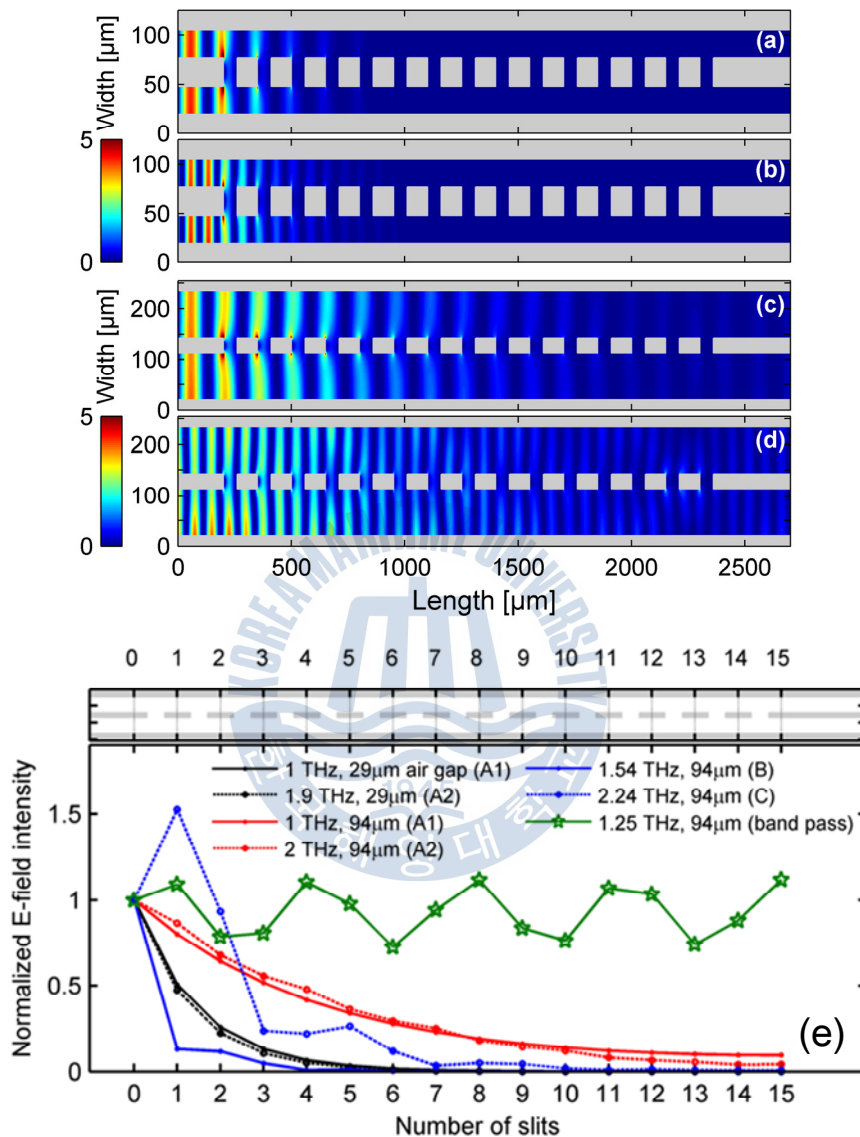
Figure 6.3   E field intensity distribution for the Bragg stop bands with different frequencies and air gaps. (a) 1 THz (A1 stop band frequency) with 29-µm air gap, (b) 1.9 THz (A2 stop band frequency: measured central frequency) with 29-µm air gap, (c) 1 THz (A1 stop band frequency) with 94-µm air gap, (d) 2 THz (A2 stop band frequency) with 94-µm air gap. (e) Comparison of power transmission for normalized time-averaged E field intensity according to the number of slits. The position of the measured average E field intensity is between slits (on the metal surface).

Figures 6.3(a) and (b) show the E field intensity distribution for the first and second measured central Bragg stop-band frequencies, which are 1 THz and 1.9 THz with g=29 µm. The intensity of the E field dramatically decreases with propagation along the slits. The FDTD computation shows that the E field transmittance at the first slit is about 50%. After the input E field has propagated through 15 slits, only 0.01% of the E field intensity remains. Thus, the dynamic range of the power transmission is approximately 90 dB, which is larger than the experimental result (60 dB). However, both results are small enough to be compared to the dynamic range of the non-stop-band frequency (pass band), for example 0.185 dB at 1.25 THz (29-µm air gap). Most of the Bragg reflections are performed in the initial section of the slits. The input THz E field intensity is only 27% (35%) after passing the second slit at 1 THz (1.9 THz). Figures 6.3(c) and (d) show the E field intensity distribution for the first and second measured central Bragg stop-band frequencies, 1 THz and 2 THz with g=94 µm. Some of the E field propagates to the end of the slit. Because of the large air gaps, the E field transmittance is increased to about 80% at the first slit. The simulation results show that the dynamic range of the power transmission for 15 slits is 24.2 dB (20.2 dB) at 1 THz (2 THz). This is in good agreement with the experimental results: 28 dB (22 dB) at 1 THz (2 THz).

6.4   FDTD simulations : B, C – non-Bragg stop band
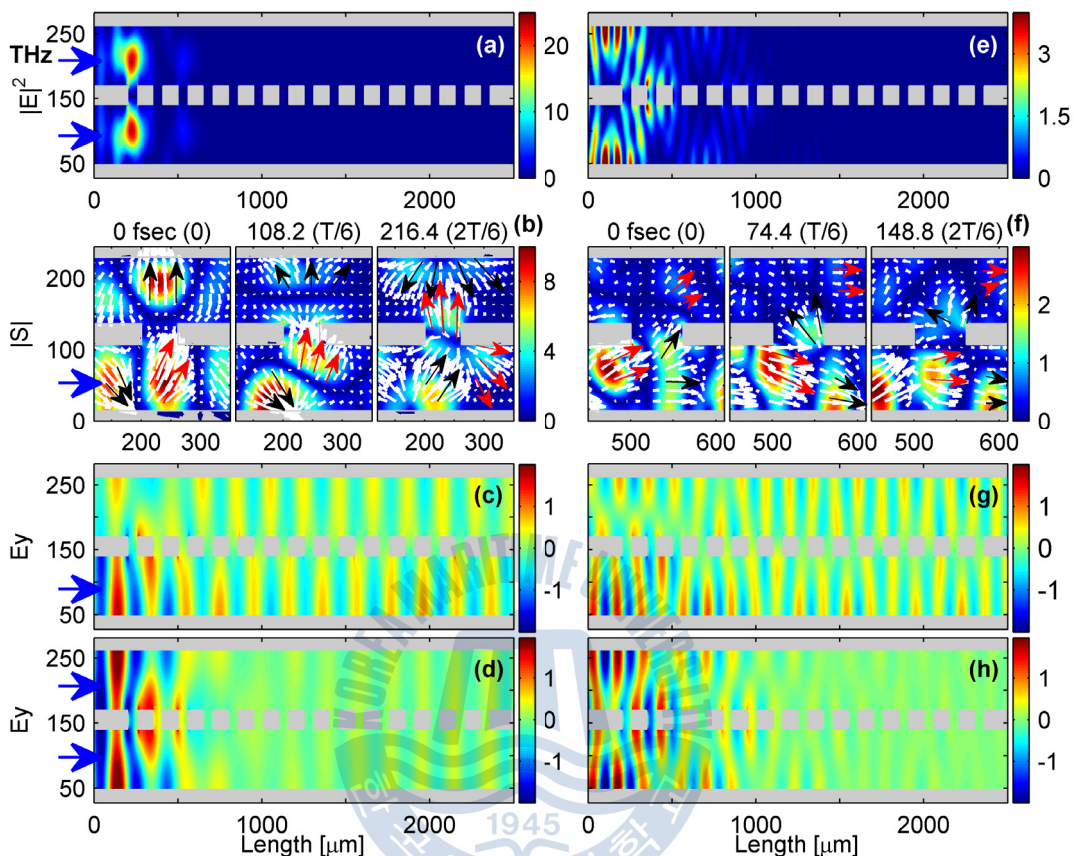
Figure 6.4   FDTD simulation with a 94-µm air gap. The left-hand figures illustrate the B stop-band frequency (1.54 THz), and the left arrowhead indicates THz beam entry to the air gaps: (a) E field intensity distribution; (b) Poynting vectors around the first slit (black and red arrows indicate π radian phase difference); (c) Ey field distribution. The right-hand figures illustrate the C stop-band frequency (2.24 THz): (d) E field intensity distribution; (e) Poynting vectors around the third slit; (f) Ey field distribution.

Figure 6.4(a) shows the E field intensity distribution of the B stop band at 1.54 THz and a 94-µm air gap. Most of the E field concentrates at the first slit. The FDTD computation shows that the E field transmittance is only 13.3% at the first slit. When the E field propagates to the first slit, some leaks into the slit gap. The

leaked E field comes out from the opposite slit exit and radiates. Most of the radiated field is reflected from the surface to the opposite waveguide plate as shown in Fig. 6.4(b), which shows the poynting vector around the first slit. Figure 6.4(b) shows the situation after 108.2-fs time intervals, each corresponding to 1/6 of the time period of T which is 1/wavelength. Figure 6.4(c) shows the Ey field distribution. The polarities of the Ey field in the upper and lower air gaps are out of phase except at the front part of the slit. When the E field appears on both sides of air gap (upper and lower), the Ey fields that leak from the slit and propagate from the other input side are out of phase. Therefore, the two Ey fields vanish in the air gap. After the input E field has propagated through 15 slits, the dynamic range of the power transmission in the simulation is approximately 33 dB. As shown in Fig. 6.2(f), the measured dynamic range is about 19 dB. To compare the dynamic ranges, we set the pass band frequency to 1.25 THz. The dynamic range of the power transmission is only 0.12 dB at the pass band. Figures 6.4(d), (e), and (f) are as for Figs. 6.4(a), (b), and (c) but for the C stop band. Figure 6.4(e) shows the poynting vector around the third slit, illustrating the situation after 74.4-fs time intervals, each corresponding to 1/6 of the time period of T. This is the same mechanism seen for the B stop band, but now only a few front slits were needed to make the fields out of phase.

6.5 FDTD simulations : 3-D THz power transmission
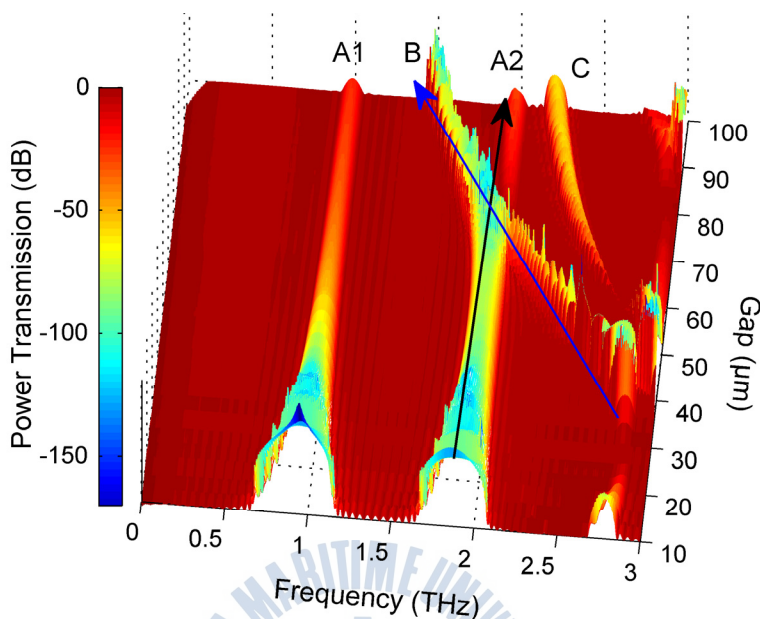
Figure 6.5   3-D THz power transmission graph for Bragg (A1 and A2) and non-Bragg (B and C) stop bands with different air gaps.

The air gap changes from 10 µm to 100 µm on the 3-D absorbance graph shown in Fig. 6.5. Because the Bragg stop bands (A1 and A2 in the figure) depend only on the period of the slits and not on the air gap variations, the stop bands always exist at 1 and 2 THz. The magnitude and width of the A1 and A2 stop bands are reduced and narrowed with an increase in the air gap. This is caused by weak coupling between the waveguide plates and the metal surface of the slit. Meanwhile, the non-Bragg stop bands are caused by the wavelength/2 delay (out of phase) between the leaked Ey field by the slit and the propagated another Ey field. This means that the frequency of the non-Bragg stop band is in inverse proportion to the air gap and the smallest air gap exists around wavelength/2 of the measured maximum frequency. Therefore the B and C stop bands are enhanced and shifted to lower frequencies with an increase in the air gap.

- 74 -

Chapter VII. Photonic band anti-crossing in a coupled system of a THz plasmonic crystal film and a metal air-gap waveguide

Periodic dielectric structures (called photonic crystals) exhibit photonic band gaps that are Bragg reflection bands for EM waves [52,53]. Photonic band gaps have been utilized in implementing THz wave devices such as mirrors, filters, cavities, super-prism, and so on [22,33,35,54-56] In the previous Chapter VI, our studies are carried out by using metal slit arrays positioned at the center of the air gaps in TPPWGs. This 1-D photonic structure induces the forbidden band gaps, but they are quite different from typical photonic band gaps. The forbidden frequency gaps strongly depend on the air-gap size and have very steep gap edges.

In this Chapter, we show that the strong mode coupling of a metal air-gap waveguide assisted by a grating vector of a 1D plasmonic crystal film, *photonic band anti-crossing*, gives rise to the forbidden frequency gaps, showing that they are different from photonic band gaps of photonic crystals. The crossing frequencies derived from the *photonic band anti-crossing model* explain well the dependence of the center frequencies of the forbidden gaps on the air-gap size and the period of the plasmonic crystal.

The forbidden frequency gap with steep gap edges could be useful in detecting the refractive index variation due to a chemical or a bio-chemical reaction in a THz range.

7.1   Experiment setup
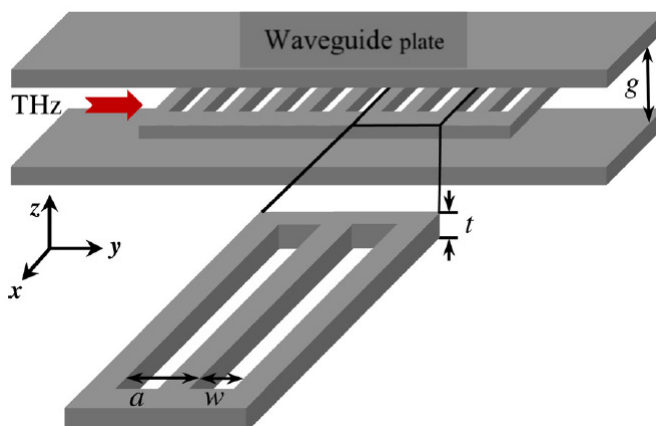
Figure 7.1   Schematic of a coupled system of a 1D plasmonic crystal film and a metal air-gap waveguide. Dark gray regions indicate a metal which is considered as a perfect electric conductor in this study.

Figure 7.1 illustrates the geometry of a 1D plasmonic crystal film, a perfect metal film with a periodic array of slits, in a metal air-gap waveguide considered in this study. The plasmonic crystal film with a period $a = 150$ µm, thickness $t = 30$ µm, and width $w = 60$ µm is positioned at the center of the air-gap waveguide. We only consider the even modes excited by the incoming Gaussian THz waves.

7.2   FDTD simulations and experiment results

Figure 7.2 shows transmission spectra and photonic band structures of even modes of the coupled system of a 1D plasmonic crystal film and a metal air-gap waveguide for the two different values of the air-gap size, (a) $g = 88$ µm and (b) $g = 218$ µm, which were obtained by FDTD simulations. The transmission spectra were simulated when a 1D plasmonic crystal film is composed of 10 air slits. The photonic band structures describe well the transmission spectra of THz waves

- 76 -

through the coupled system of a 1D plasmonic crystal film and a metal air-gap waveguide. When g = 88 µm, there are two photonic band gaps, A1 and A2, at band edges π/a and k = 0 that correspond to *Bragg reflection bands* positioned around $pc/2a$, where c is the speed of light in air and p = 1 and 2. Interestingly, as g increases to g = 218 µm, there are new frequency band gaps of B and C opened at k = 0.263 $\times$ $(2\pi/a)$ and k = 0.134 $\times$ $(2\pi/a)$, respectively, *not Bragg reflection bands*. Note the band edges of B band are much steeper than those of A1 and A2 bands.
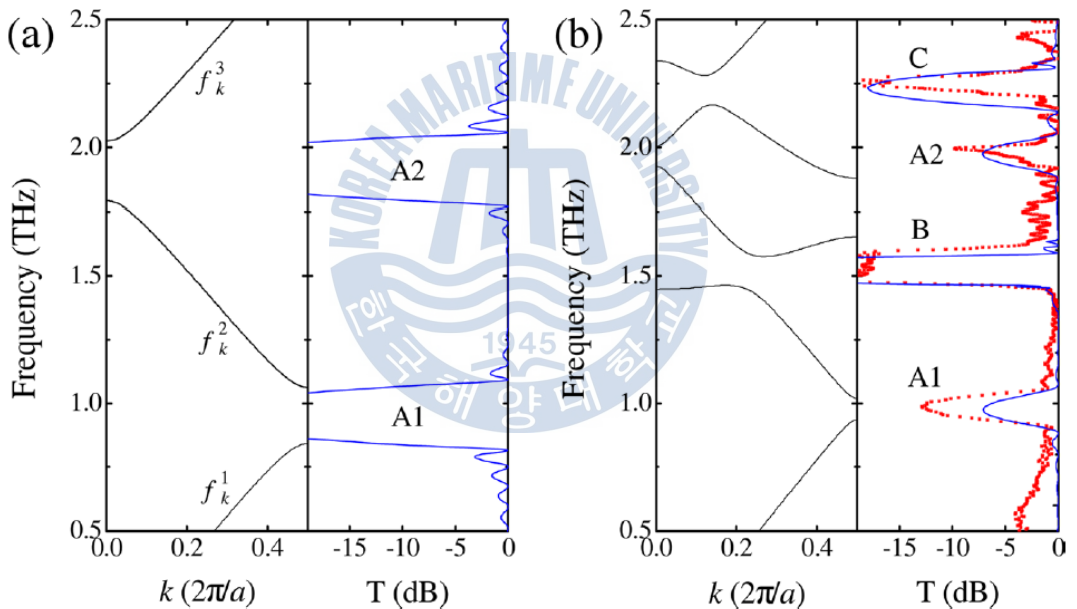
Figure 7.2 Simulated photonic band structures and transmission spectra of a coupled system of a 1D plasmonic crystal film and a metal air-gap waveguide for the different values of the air-gap size, (a) g = 88 µm and (b) g = 218 µm. Photonic bands are labeled as f_n^k where n is a band index and k is a wavevector in irreducible Brillouin zone. A1 and A2 denote the Bragg reflection bands and B and C denote the non-Bragg reflection bands, respectively. Measured transmission spectrum (dotted line) agrees well with the FDTD result (solid line).

7.3   Analysis : Anti-crossing model

To explain the existence and the properties of the non-Bragg frequency band gaps, we first study guiding modes of a metal air-gap waveguide. The dispersion relation of TM modes of a metal air-gap waveguide with the air-gap size of g is given by

$$f(m,K) = \frac{c}{2\pi} \sqrt{K^2 + \left(\frac{m\pi}{g}\right)^2} \tag{37}$$

$m = 0, 2, 4 \cdots$ for even modes, and $m = 1, 3, 5 \cdots$ for odd modes

where K is a wave vector of TM mode. Figure 7.3(a) shows the dispersion curves of the first and the second even modes of a metal air-gap waveguide obtained by the Eq. (37) under 2.6 THz when $g = 218$ µm. Insets show the magnetic-field
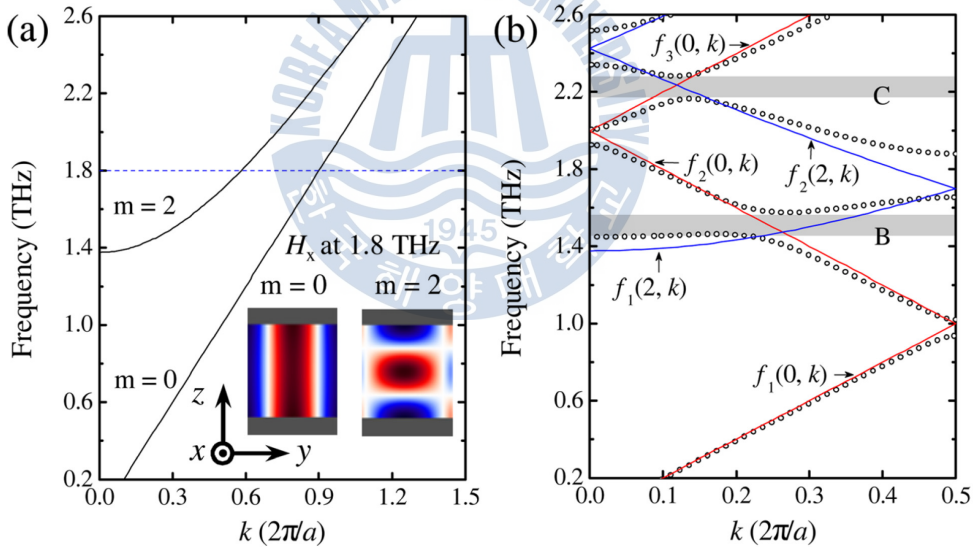
Figure 7.3   (a) Dispersion curves of a metal air-gap waveguide with $g = 218$ µm. Insets show the magnetic-field distributions of the first and the second even modes at a frequency f = 1.8 THz. Dark gray regions indicate metal waveguide plates (b) The photonic band structure of the coupled system of a 1D plasmonic crystal film and a metal air-gap waveguide (open circles) when $g = 218$ µm. Solid lines denote the folded bands of the first and the second even modes of a metal air-gap waveguide in the irreducible Brillouin zone. Gray regions denote the forbidden frequency gaps of B and C.

distributions of the modes at a frequency f = 1.8 THz. One can see that the first even mode cannot intersect with the second one.

To see the effect of introduction of a 1D plasmonic crystal film, it is convenient to fold dispersion curves of guiding modes into the irreducible Brillouin zone (BZ), $0 \leq k \leq \pi/a$. For example, relations of the lowest three folded bands and a unfolded dispersion curve at a wave vector k are given by

$$f(m, \pm k) = f_1(m, k) \tag{38}$$

$$f(m, \pm (2\pi/a - k)) = f_2(m, k) \tag{39}$$

$$f(m, \pm (2\pi/a + k)) = f_3(m, k) \tag{40}$$

where the subscripts 1−3 indicate index of band.

Figure 7.3(b) shows the folded bands of the first and the second even modes of a metal air-gap waveguide (solid lines) and a photonic band structure of a coupled system of a 1D plasmonic crystal film and a metal air-gap waveguide (open circles) when g = 218 μm. One can clearly see that the forbidden frequency gap of B (C) results from the mode splitting due to the anti-crossing of $f_1(2, k)/f_2(0, k)$ and $f_3(0, k)/f_2(2, k)$. Introducing a 1D plasmonic crystal film in a metal air-gap waveguide makes the strong coupling between even modes possible when their wave vector difference satisfies the condition, $|K_i - K_j| = q \times (2\pi/a)$ where K_i and K_j are parallel or anti-parallel to each other and q is a non-negative integer. Note the direction of the unfolded wave vector of $f_2(0, k)$, $K_1 = k - 2\pi/a$, ($f_3(0, k)$, $K_1 = k + 2\pi/a$) is anti-parallel to that of the unfolded wave vector of $f_1(2, k)$, $K^2 = k$, ($f_2(2, k)$, $K^2 = k - 2\pi/a$) and the magnitude of their wave vector difference is $2\pi/a$ ($4\pi/a$). It is well known that a strong interaction between electronic bands of semiconductors, the band anti-crossing, leads to a splitting of the bands. [57] However, the photonic band anti-crossing in typical photonic crystals has not been reported so far.

- 79 -
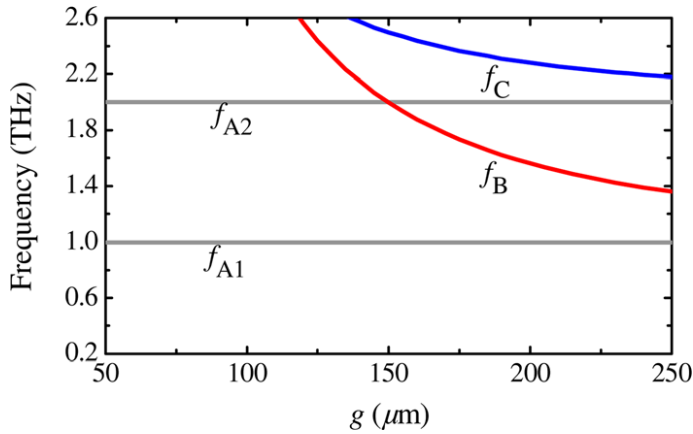
Figure 7.4 Dependence of f_B and f_C on the air-gap size g. f_{A1} and f_{A2} denote the center frequencies of the Bragg reflection bands of A1 and A2, respectively.

Analytical expression of the anti-crossing frequency can be useful in describing the dependence of the forbidden frequency gap on the period of the plasmonic crystal film and the air-gap size. The equations of $f_3(0, k)=f_1(2, k)$ or $f_2(0, k)=f_1(2, k)$ give f_B related to the position of band B and the equation of $f_3(0, k)=f_2(2, k)$ does f_C related to the position of band C,

$$f_B = \frac{c}{a}\left[\frac{1}{2}+\frac{1}{2}\left(\frac{a}{g}\right)^2\right],$$ (41)

and

$$f_C = \frac{c}{a}\left[1+\frac{1}{4}\left(\frac{a}{g}\right)^2\right],$$ (42)

Dependence of f_B and f_C on the air-gap size was shown in Fig. 7.4. f_{A1} and f_{A2} denote the center frequencies of the Bragg photonic band gaps of A1 and A2, respectively. f_B and f_C explain well the dependence of the positions of B and C on the air-gap size, observed experimentally in the previous study (Chapter VI). Note that the center frequencies of the forbidden frequency gaps depend on the ratio of the air-gap size and the period of the plasmonic crystal film a/g, while the center frequencies of Bragg reflection bands of A1 and A2 are independent of g.

- 80 -

Chapter VIII. Properties of defected one-dimensional THz plasmonic crystal films in a metal air-gap waveguide

Photonic crystals that are periodic dielectric structures can exhibit photonic band gaps which are frequency ranges where electromagnetic waves cannot propagate. Local defects introduced in a photonic crystal can create propagation modes in photonic band gaps, i.e., *defect modes* that are strongly localized around the local defects [53]. Thus the localized defect modes have been used in implementing optical devices such as filters, cavities, and waveguides [58,59]. In Chapter VI, we have reported that a 1D plasmonic crystal film inside a PPWG exhibits *photonic band gaps* in a THz frequency range because of strong THz wave confinement. Thus introducing local defects in a 1D plasmonic crystal film in a PPWG can create strongly localized modes at specific positions inside a PPWG. Since a PPWG has been widely employed to study spectroscopy in a THz range, the strongly confined electric fields of localized THz waves at a specific place inside a metal air-gap waveguide can be useful in sensing biomaterials or chemical reactions.

In this Chapter, we investigate properties of defect modes of a defected 1D THz plasmonic crystal film in a PPWWG. The plasmonic crystal film was fabricated by making periodic eleven air slits in a metal sheet. A defect was created by *varying the width of an air slit* at the center of the plasmonic crystal film. The *donor* (accept)-like defect modes were observed when the width of the defect air slit *increase* (decrease) from an initial width. Simulated spatial distributions of defect modes show Fabry-Pérot cavity-like resonant modes strongly localized inside the defect air slit. The Q factor of a defect mode can be tuned by the air-gap size. The high-Q defect mode can be used for THz sensor applications.

8.1   Experiment setup
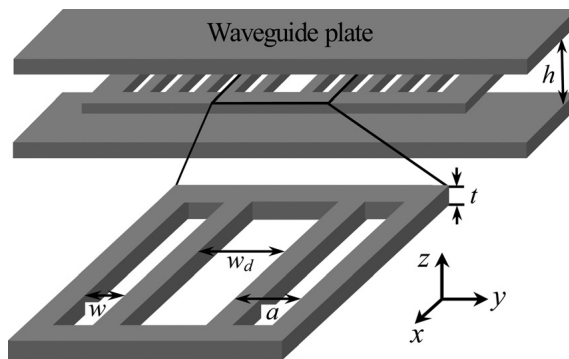
Figure 8.1   Schematic of a 1D plasmonic crystal film with a defect air slit of w_d in a metal air-gap waveguide. Dark gray regions indicate a metal which is considered as a perfect conductor in this study.

Figure 8.1 shows the schematic view and geometric parameters of a 1D plasmonic crystal film, a perfect metal film with a periodic array of slits, and a metal air-gap waveguide considered in this study. a and w are the period and the width of air slits, and t is a thickness of a perfect metal film. A defect is created by varying w_d, the width of a slit located at the center of the array. The plasmonic crystal film is positioned at the center of the air-gap waveguide with the air-gap size defined as the distance between two metal plates denoted by h in Fig. 8.1.

8.2   FDTD simulations : Defect modes

We first investigate frequencies and field distributions of defect modes by using FDTD simulations. Figure 8.2(a) shows that frequencies of defect modes when w_d varies. The white regions denote photonic band gaps of a 1D plasmonic crystal film in a metal air-gap waveguide when a = 150 µm, t = 30 µm, w = 60 µm and h = 82 µm, and solid circles represent the frequencies of defect modes as a function of w_d. Note there is no defect mode when w_d = 60 µm, denoting a vertical dashed line. One can see that frequencies of defect modes go down from the upper edges of photonic band gaps as wd increases from 60 µm, while ones of defect modes go up from the lower edges of photonic band gaps as w_d decreases

- 82 -

from 60 µm. In analogy of electronic defect states in semiconductors, air slits with w_d larger (smaller) than 60 µm show the behavior of donor (acceptor)-like defects. Figure 8.2(b) represents the spatial distributions of electric fields (E_z) of selected defect modes when w_d = 40, 120, 180, 240, and 300 µm. The selected modes are denoted by the circled numbers in Figs. 8.2(a) and (b). One can see that the defect modes show the characteristics of Fabry-Pérot cavity-like resonant modes.
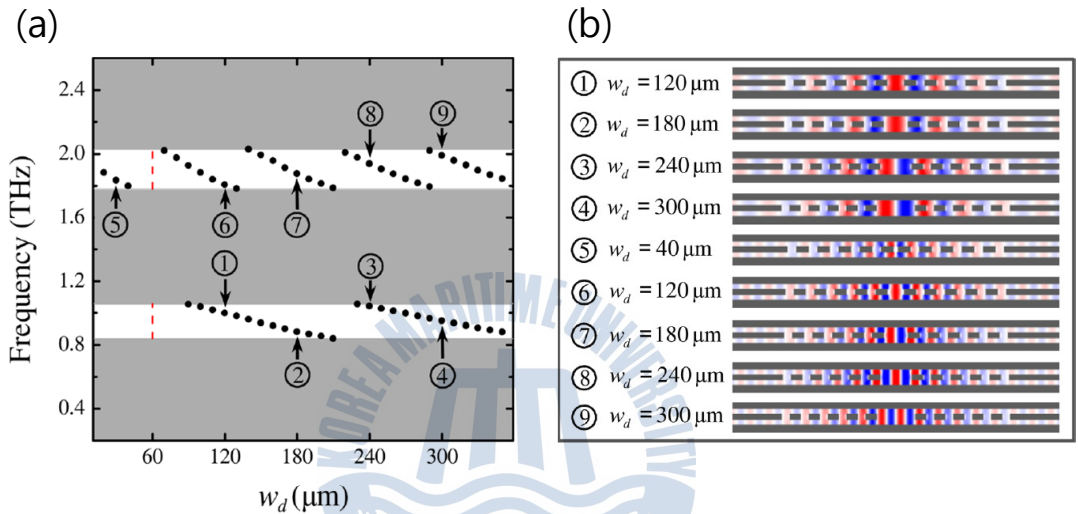
Figure 8.2 (a) Defect mode frequencies as a function of w_d and (b) spatial distributions of electric fields of selected defect modes denoted by the circled numbers in (a). The white regions denote photonic bandgap ranges of a 1D plasmonic crystal film in a metal air-gap waveguide when a = 150 µm, t = 30 µm, w = 60 µm, and h = 82 µm. A vertical red-dashed line indicates no defect modes when w_d = 60 µm.

8.3 FDTD simulations and experimental results

Figure 8.3(a) shows the measured (blue-thick lines) transmission spectra through the plasmonic crystal films with a = 150 µm, t = 30 µm, and w = 60 µm in a metal air-gap waveguide with h = 82 µm ± $\triangle h$ of 2 µm when w_d = 120, 180, 240, and 300 µm and the simulated ones (red-thin lines) with neglecting $\triangle h$, respectively. The samples were fabricated by making slits in stainless sheet made by micro-photochemical etching. And we used THz-TDS system described in chapter 1.4. The measured spectra show clearly transmission peaks in photonic band gaps.

The measured transmission peaks correspond well to frequencies of defect modes obtained by FDTD simulations in Fig. 8.2(a). The photonic band gap size of a 1D plasmonic crystal film in a metal air-gap waveguide decrease as h increases, while the photonic bandgap position is nearly independent of h. Thus it is interesting to investigate dependence of frequencies and Q-factors of defect modes on h. Figure 8.3(b) shows measured transmission spectra (blue-thick lines) through the defected plasmonic crystal with w_d = 300 µm when h = 80, 110, 140, 170, 200, and 230 µm ± $\triangle h$ of 5 µm and the simulated ones (red-thin lines) with neglecting $\triangle h$. One can see that the defect mode frequencies slightly decrease as h decreases as shown in Fig. 8.4(a). The difference between the measured and the simulated defect mode frequencies may come from the uncertainty of h.
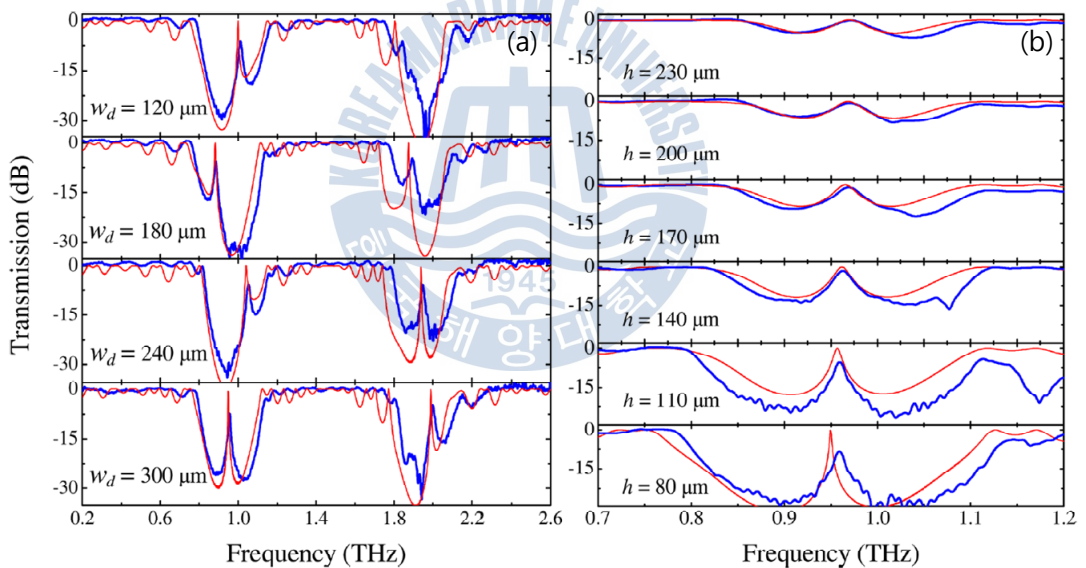
Figure 8.3   (a) Measured transmission spectra (blue-thick lines) through the plasmonic crystal films with a = 150 µm, t = 30 µm, and w = 60 µm in a metal air-gap waveguide with h = 82 µm ± $\triangle h$ of 2 µm when w_d =120, 180, 240, and 300 µm and simulated ones (red-thin lines) with neglecting $\triangle h$.
(b) Measured transmission spectra (blue-thick lines) through the defected plasmonic crystal with w_d = 300 µm when h = 80, 110, 140, 170, 200, and 230 µm ± $\triangle h$ of 5 µm and the simulated ones (red-thin lines) with neglecting $\triangle h$.
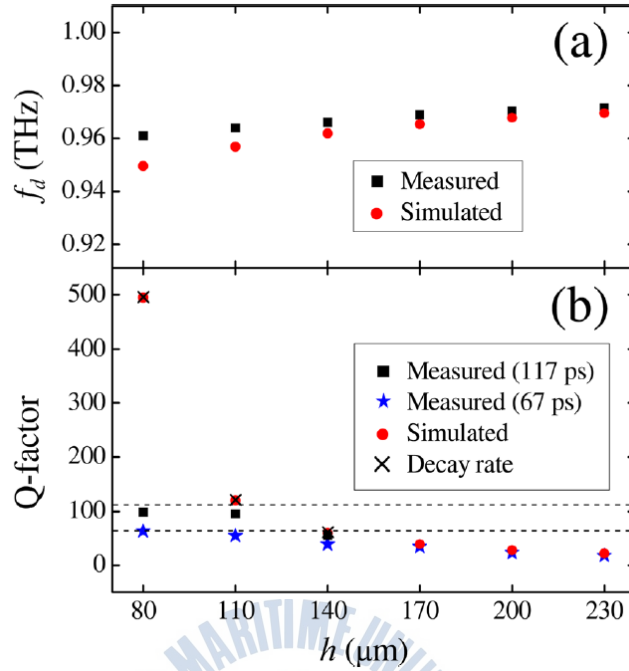
Figure 8.4 (a) Measured (■) and simulated (●) defect mode frequencies, f_d and (b) Q-factors of defect modes from the transmission spectra transformed from the measured 3500 (2000) data points time-domain wave forms [■(★)] and the simulated transmission spectra (●). Cross symbols (×) denote Q-factors calculated from the decay rates of defect modes. Dashed lines denote positions of Q-factors of 64 and 112.

Easily expected, the Q-factor of a defect mode which is defined as $f_d / \delta f$, where f_d is a defect mode frequency and δf is the full-width at half maximum, increase as h decreases as shown in Fig. 8.4(b) because the confinement of the z-direction electric field gets much stronger as h decreases. Note the high Q-factor (500) of the defect mode when h = 80 μm. To confirm the high Q-factor, Q-factors of defect modes, when h = 80, 110, and 140 μm, were obtained from time-domain simulations to calculate decay rates of the resonant defect modes corresponding to the number of periods for the energy to decay by $e^{-2\pi}$. The Q-factors from the decay rates [cross symbols (×)] were presented in Fig. 8.4(b). One can clearly see that the Q-factors from the decay rates are well agreed with those from the simulated transmission spectra.

- 85 -
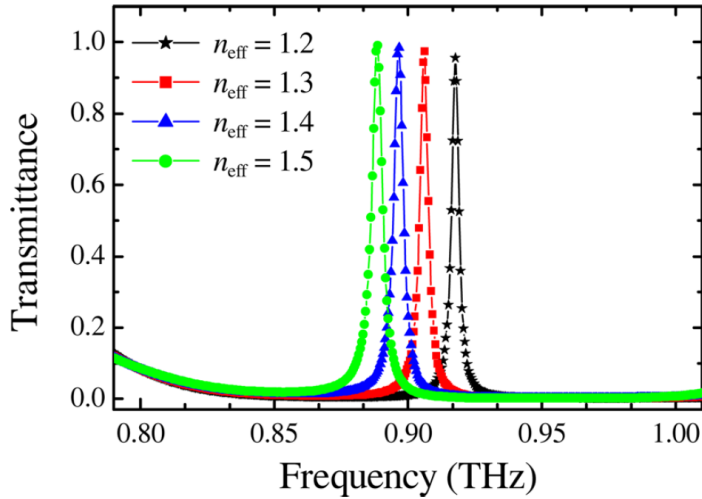
Figure 8.5   Transmission spectra around the first defect mode frequency when w_d = 300 µm and h = 82 µm. n_{eff} varies from 1.2 to 1.5. The averaged $\triangle f_d$ / $\triangle n_{eff}$ to mean refractive index sensitivity of the defect mode is about 100 GHz/RIU.

Figure 8.5 shows the transmission spectra around the first defect mode frequency when the effective refractive index is 1.2, 1.3, 1.4, and 1.5. The averaged $\triangle f_d$ / $\triangle n_{eff}$ to mean refractive index sensitivity of the defect mode is about 100 GHz/RIU (refractive-index-unit). Hence, a coupled system of a defected 1D plasmonic crystal and a metal air-gap waveguide could be useful for THz sensors.

In conclusion, we investigated characteristics of localized defect modes caused by a defect slit located at the center of a 1D THz plasmonic crystal film in a metal air-gap waveguide. As the width of the defect slit increases (decreases) from an initial width, the defect mode frequencies decrease (increase) from the upper (bottom) edges of photonic band gaps. As the air-gap size decreases, the Q-factor of the defect mode increases rapidly, while the defect mode frequency decreases slightly. The defect mode with a high Q-factor could be useful in realizing THz sensors for gas detection, chemical reactions, and biomaterials.

Chapter IX. Application for THz filters and Sensing based on band gaps properties by using metal slits in TPPWG

Due to the confined THz beam in the sub-wavelength region, the PPWG has not only played the role of coupling THz beams with a waveguide but has also been utilized to study potentially useful phenomena like THz filters. These THz filters will be useful in future research areas such as THz communication, sensors, and devices. In the recent past, a high Q factor based on defect-mode resonance and Bragg resonance was employed by a periodic metal structure on a metal plate using standard lithographic and metallization techniques [23,60]. Using TE_1 mode from the PPWG, a highly sensitive fluid refractive-index sensor [30], tunable universal THz filters [27,28] and a mechanically tunable THz notch filter [61,62] have been achieved. However, such studies have not been able to simultaneously satisfy conditions such as the *TEM mode, high Q factors*, *high signal-to-noise ratios*, and *tunable notch filters*.

The photonic crystal in PPWG inserted slit array in Chapters VI-VIII showed that the various band gaps can be formed. And the formation of band gaps and the mechanism of their formation as several sample conditions were analysed and understood. So, now we try to apply these properties for various applications with perfect their understanding. An easily installable notch filter satisfying the above conditions is implemented using the characteristics of the non-Bragg stop band. And an LPF, which cuts off high frequency regions using metal slit arrays having multiple Bragg stop bands, will be also implemented. Especially, a tunable notch filter with a good sensitivity and high Q factor will be simulated for gas sensor.

9.1 Experimental setup : Notch Filter
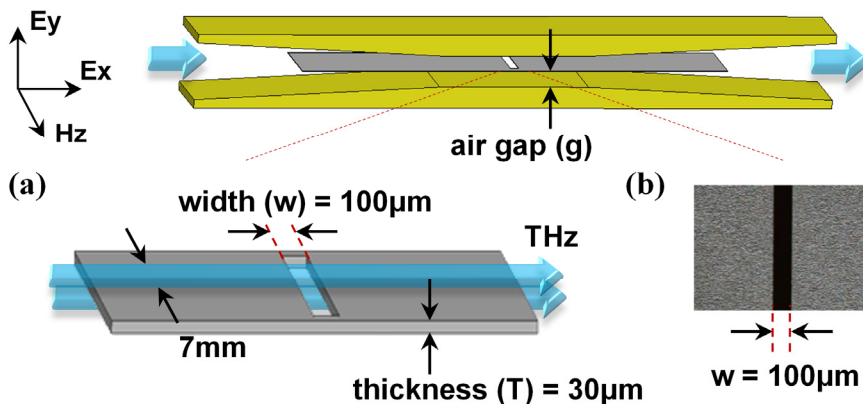
Figure 9.1 Diagram of TPPWG and slit sample. (a) THz beam propagating along the upper side and the lower side of a stainless steel slit. (b) Photo image of slit with 100-μm slit width.

The experimental setup is similar to the one in Chapter 6.1. Instead of the multiple slits used previously to study the band gap properties, a single stainless steel slit was employed as a notch filter. As shown in Fig. 9.1(a), the slit has 30-µm thickness, 100-µm width, and 9-mm length where the propagated THz beam width is 7 mm. A vertically polarized (y direction) THz beam, which is perpendicular to the tapered surface (x×z surface) of the waveguide, generates a TM modes. And THz beam is gradually confined through the 9-mm long flat area in the waveguide. As the total length of the stainless steel is 96 mm, the stainless steel protrudes toward the inlet and outlet of the tapered area by 43.5 mm. Identical metal spacers are used to make same upper and lower air gaps. Such a structure confines the THz beam to the two equal-width air gaps on opposite sides of the steel plate, as the incident THz beam is split into two parts by the protruded stainless steel before arriving at the air gap in the waveguide. Therefore, the incident THz beams are propagated simultaneously across the upper side and the lower side of the slit along each air gap. Figure 9.1(b) shows a photo image of the slit sample, which was made by micro-photochemical etching.

Collection

9.2 Experimental results : Notch Filter
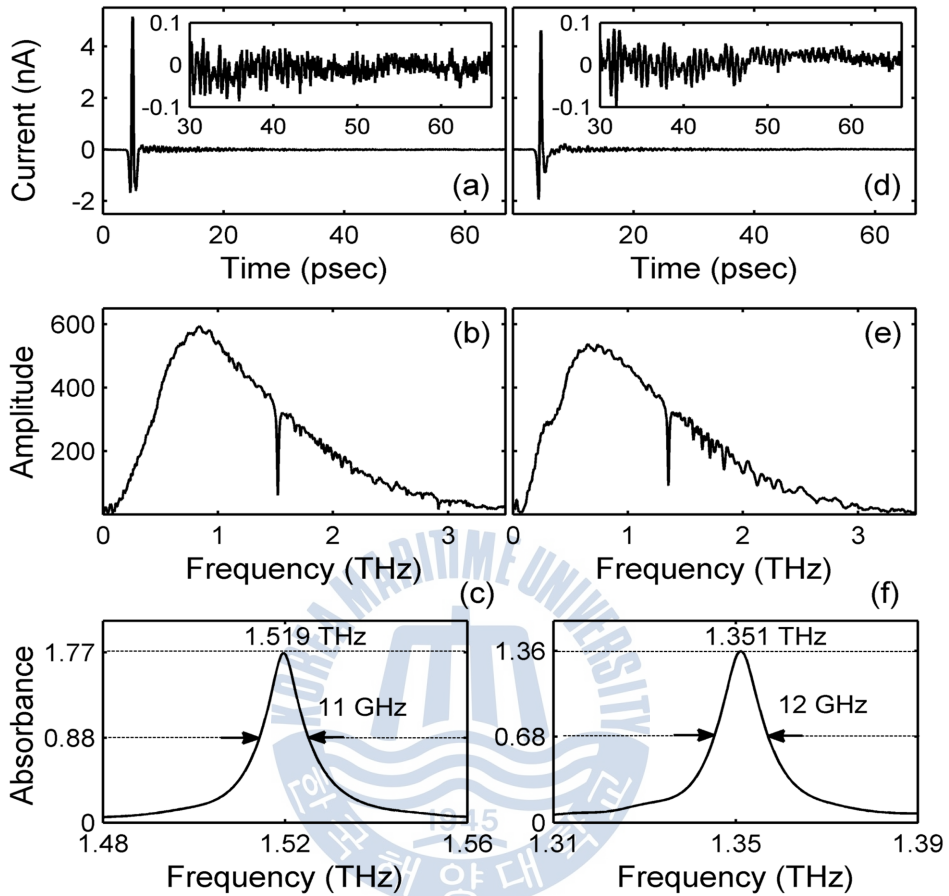
Figure 9.2 (a) Measured THz pulse for a 92-µm air gap. The inset shows the expanded THz ringing from 30 ps to 66 ps. (b) Spectrum of the THz pulse. (c) Absorbance spectrum zoomed in on the resonance. (d)-(f) identical to (a)-(c) but for a 105-µm air gap.

Figure 9.2 shows each THz pulse and spectrum resulting from the 92-µm and 105-µm air gaps in order to study the tunable properties of the THz notch filter. The image inserted in the THz pulse in Fig. 9.2 (a) and (d) displays the ringing related to the resonance of the notch filter existing after the main pulse. Now that the resonance of the notch filter in the spectrum region is very sharp, the THz ringing in the time domain has been measured over a sufficiently large period of time at

about 66 ps. The amplitude of the ringing at 66 ps is reduced about 1/210 compared to the amplitude of the main THz pulse. The spectra of the THz signals after zero padding are shown in Fig. 9.2(b) and (e). The 66 ps data was extended to 1320 ps by adding zeros at the end of the data. As the air gap had changed from 92 µm to 105 µm, the resonance frequency of the notch filter had also moved to a low frequency region by 0.168 THz (from 1.519 THz to 1.351 THz). The frequency tuning sensitivity (FTS) is given as $\triangle f / \triangle g$, where $\triangle f$ is the resonance frequency shift and $\triangle g$ is the air gap variation. Therefore, the FTS is 12.9 GHz/µm, which shows a tunable notch filter in the THz region. The FTS value is two orders higher compared to that determined from previous methods such as the Fabry-Perot resonance [62] and Bragg resonance [23] methods. Figure 9.2(c) and (f) show the absorbance of the resonance frequency; the arrows denote the FWHM of each absorbance, 11 GHz and 12 GHz, respectively. The calculated Q factors (resonance frequency divided by FWHM) are 138 and 113, respectively. The previous studies have tunable resonance frequency but small Q factor [28, 62], high Q factor but fixed resonance frequency [23], and tunable resonance frequency but a low signal-to-noise ratio [61]. However, the advantage of the notch filter used in this study is its tunable resonance frequency with high Q factor and high signal-to-noise ratio.

9.3   FDTD simulations : Notch Filter
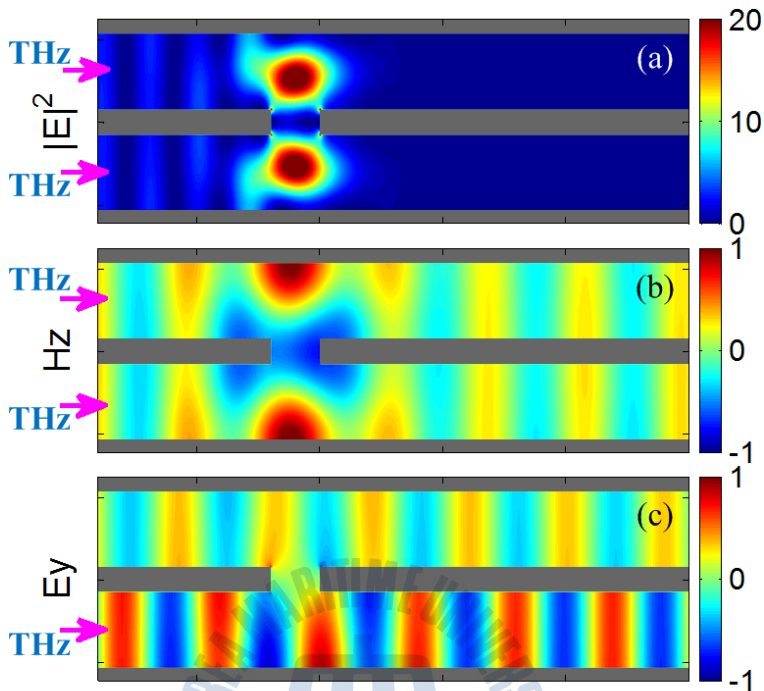
Figure 9.3   FDTD simulation with 92-μm air gap and 1.519 THz continuous wave source. The arrows indicate THz beam incident to the air gap. (a) E field intensity distribution; (b) Hz field distribution; (c) Ey field distribution.

Unlike the Bragg resonance of the defect mode, the measured notch filter resonance can be explained by the canceling out of the THz beams due to the out-of-phase component between the straight THz beam and the THz beam passing through the slit. Figure 9.3 shows FDTD simulation results considered under the conditions of resonance frequency of 1.519 THz and 92-µm air gap. Figure 9.3(a) shows the electric field intensity ($|E|^2$) when a THz beam propagates along the air gap supper and lower the stainless steel slit sample. The electric field is intensely localized in the areas upper and lower the slit. The air gap regions after passing the slit show almost no distribution of the field. Therefore, the 1.519 THz source cannot be

measured in the output spectrum that makes the notch filter. Figure 9.3 (b) illustrates the z-direction of the magnetic field (Hz), showing a symmetric distribution in both the upward and downward directions. Such structural symmetry enables a beam in one gap to leak into another gap and propagate with the same pattern. For that reason, as shown in Fig. 9.3(c), the simulation was performed by incident Ey field of the THz beam lower the air gaps only. Though it is a single slit, the THz beam of the resonance frequency leaks through the slit and distributes across the area on the other side of the air gap. The phase difference caused by time delay is a π radian corresponding to wavelength/2. Therefore, the electric field emerging between the air gaps upper and lower is out of phase. When the THz beams incident upper and lower the air gaps at the same time as in the experiment, the THz beams are canceled out after the slit. This phenomenon generates a narrow dip in the spectrum region and turns it into a notch filter.
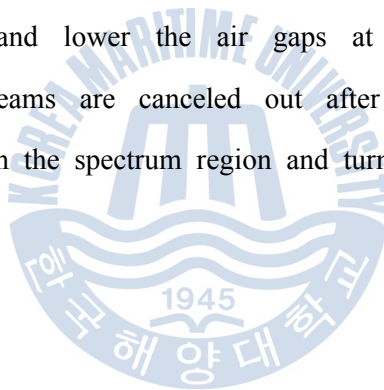
9.4   FDTD simulations : Notch Filter Sensor

In the above section, using only one slit, a tunable notch filter is implemented which have high Q factor and wide tunability. This filter is used the band gap B. In this section, we demonstrated the sensing ability of the different reflective index using FDTD simulation.
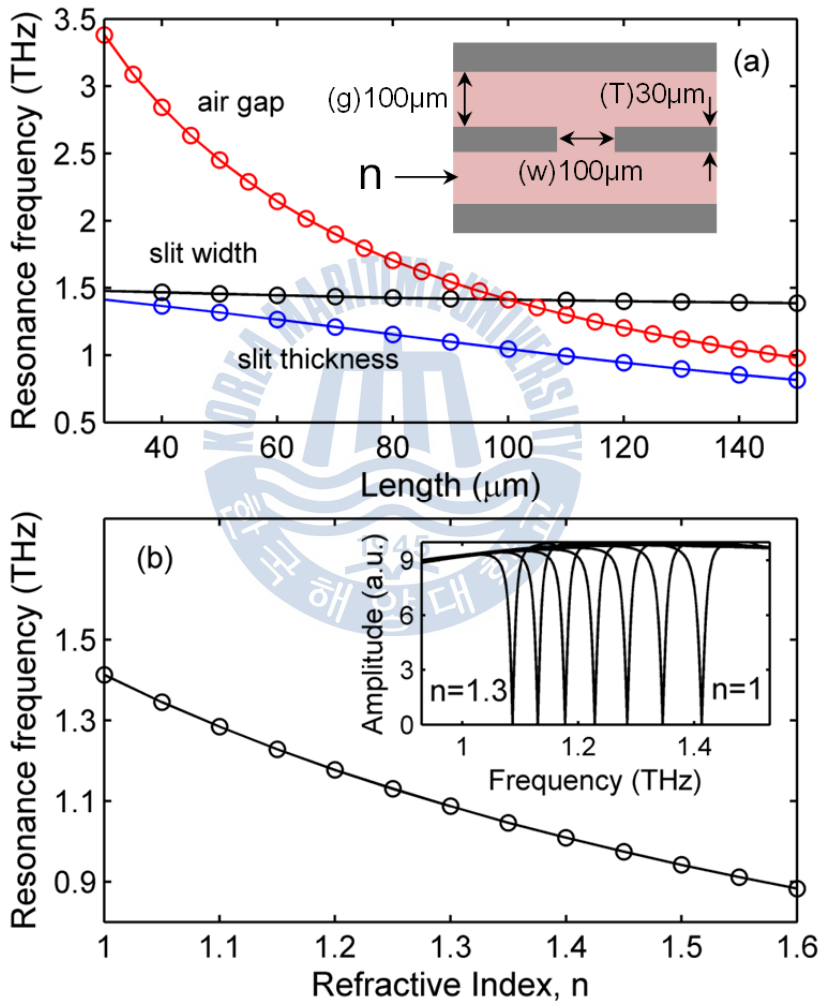
Figure 9.4   (a) Resonance frequency shift of a notch filter according to air gaps, slit width, and slit thickness. The inset shows basic dimension of the slit and air gap. (b) Resonance frequency shift of a notch according to refractive index. The inset shows resonance frequency with refractive index from 1 to 1.3.

As shown in the images inserted in Fig. 9.4 (a), the resonance frequency shift of a notch filter according to 3 dimensions of a waveguide setup ─ 100µm air gap (g), 100 µm slit width (w), and 30 µm slit thickness (T) ─ were changed using an FDTD simulation. When only one variable among air gap, slit width, and slit thickness changed from 30 µm to 150 µm at a time, the resonance frequency shifts ($\triangle f$) are 2.4 THz, 0.09 THz and 0.59 THz, respectively. The calculated FTSs are 20 GHz/µm, 0.75 GHz/µm, and 4.91 GHz/µm, respectively. Since the phase shift of the THz beam mostly depends on the air gap, the variations of slit width and thickness are not very sensitive. However, the air gap variation is most sensitive for FTS. Moreover, the smaller the air gap, the bigger the FTS becomes. When the air gap is slightly asymmetrical, the amplitude of the notch filter decreases because the intensity of out-of-phase components is not same. Moreover the position of notch filter for asymmetry depends on larger air gap than the smaller one. According to the precise adjustment of the air gap, the resonance frequency of the notch filter can be controlled.

Figure 9.4(b) shows the resonance frequency shift from 1.41 to 0.88 THz when the refractive index changes from 1 to 1.6. In this case, a gases having high refractive index are filled in the waveguide channel instead of air. According to the data shown in the figure, the average FTS for the refractive index, $\triangle f/\triangle n$ where $\triangle n$ is the refractive index variation, becomes 0.883 THz/RIU (RIU is the abbreviation for reflective index unit), which is an order of magnitude larger value than that in the recently reported results [30]. The inserted figure in Fig. 9.4(b) illustrates the resonance frequency with the change of the refractive index of the air gap from 1.0 to 1.3. In particular, the FTS is very sensitive (1.36 THz/RIU) when the refractive index is 1 in a vacuum. Therefore, it can be possible to distinguish air and other gases (gas detection) that occur in very small amounts in the air gap.

9.5 FDTD simulations : Low-Pass Filter

A THz beam propagating along slits with a period P inside a TPPWG has a Bragg stop band with strong resonance at a Bragg frequency f_{Bragg}=mc/(2P), where m is an integer and c is the speed of light. The band width of the Bragg stop band broadens as the period gets narrower at the Bragg stop band positions in the high frequency range. Using such characteristics, if slits with different periods are arrayed in a line on a metal sheet, a LPF can be implemented to completely eliminate the high frequency component after cutoff frequency. To design such an LPF, slits with equal width of 60µm and 7 different periods of slit pattern were designed as shown in Table 9.1.

Region	I	II	III	IV	V	VI	VII
Period P [µm]	170	150	140	130	120	110	100
Width w [µm]				60			
Number of Slits N [ea]				10			

Table 9.1 Dimensions of each region of the slit used in LPF. Each region has 10 slits (N) and 60-µm width (w).

Since each region has 10 identical slits, the total number of the slits is 70. Figure 9.5(a) shows images of some of the slits in region I and region VII ; slits were made of stainless steel with a thickness of 30µm. Figure 9.5(b) shows the FDTD simulation results for Bragg stop bands when the air gap is 38 µm. As shown in the figure, the first and second Bragg resonance frequencies corresponding to the slits of region I are located at 0.85 and 1.7 THz, respectively. The bandwidths of each Bragg stop band are 0.19 THz and 0.24 THz, where the bandwidths are measured at a width at 3 dB. The first and second Bragg stop bands of each of the 7 slit patterns are overlapped. Moreover, the first Bragg stop band of region VII (from 1.23 THz to 1.62 THz) and the second Bragg stop band of region I (from 1.58 THz to 1.82 THz) overlap. Only a THz field whose frequency range is below the first Bragg stop band of the slits of region I can propagate to the exit of the waveguide. Therefore, the characteristics of LPF depend on the first Bragg

stop band of region I. The LPF can be predicted to have a 0.76 THz cutoff frequency, 55 dB power transmission in the cutoff region, and 84 GHz transition width (a drop from 90% to 10%) at the cutoff region.

In order to confirm that the slits block the propagation of this particular THz component, FDTD simulation was performed using a THz continuous wave (CW) source. As shown in the red vertical dashed line in Fig. 9.5(b), a 2.3 THz CW source propagates through regions I, II, and III. However, the Bragg stop band of the slits of region IV includes 2.3 THz, which prevents the THz beam propagation along the air gap. Figure 9.5(c) displays a simulation with a 38-µm air gap and a 2.3 THz CW source. Region IV prevents the THz beam propagation to the higher regions.
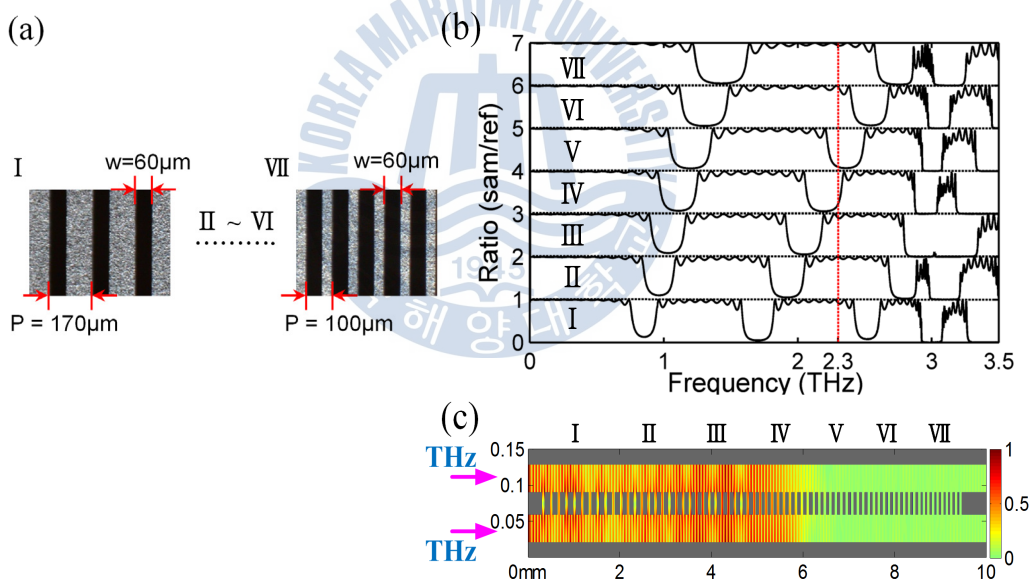
Figure 9.5   (a) Slit images in region I and region VII. Areas from region II to region VI are not shown in the figure because of limited space but these areas are continuously connected. (b) Bragg stop band positions in each region. The (red) vertical dashed line indicates 2.3 THz. (c) FDTD simulation of E field intensity distribution for 2.3 THz continuous wave source.

9.6　Experimental results : Low-Pass Filter
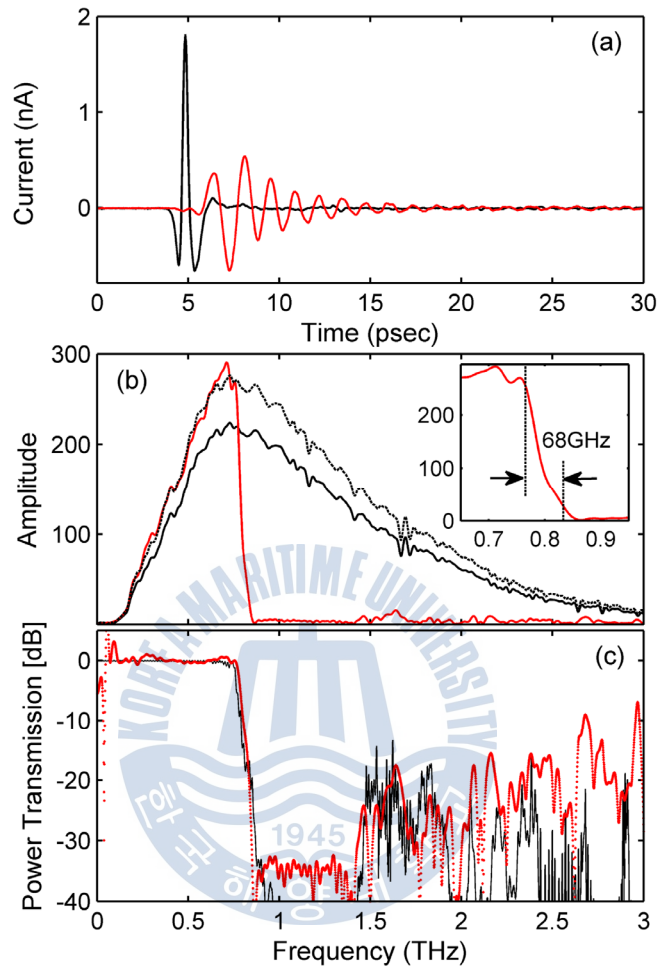
Figure 9.6　(a) Comparison of a THz reference pulse (black) without slits in the stainless steel sheet and output a THz pulse (red) with slits in the stainless steel sheet. (b) The spectra of the reference (black) and output (red). The dashed spectrum indicates a numerically modified reference spectrum. The inset shows expended figure near the cutoff frequency. (c) Comparison of power Transmission in the measurement (red) and FDTD simulation (black).

Figure 9.6(a) shows the measured reference THz pulse (black) without slits in the stainless steel sheet and output of a THz pulse (red) with slits in the stainless steel sheet where the thickness of the sheet and air gap are 30 µm and 38 µm,

respectively. The oscillation of the output THz pulse is much broader than that of the reference THz pulse, whereby a large number of low-frequency components can be assumed. Moreover, the output THz pulse has a time delay compared to the reference THz pulse, caused by the group velocity delay at the time of passing the slits. The spectra of the measured THz pulses are shown in Fig. 9.6(b). The amplitude of the output spectrum (red) is cut off at 0.78 THz, which is consistent with the simulation results in Fig. 9.5(b). As shown in the inserted figure, the magnitude response changes from pass band to stop band. The transition width is about 68 GHz. On the other hand, the amplitude of the output spectrum is larger than that of the reference spectrum. The summation of total slit width (60 µm x 70 ea = 4200 µm) allows a small propagation loss because one large air gap (38 µm + 30 µm + 38 µm = 106 µm) between two waveguide plates has smaller attenuation than the two small (38 µm) air gaps. Therefore, a power transmission, as shown in Fig. 9.6(c), was obtained by using numerical modification of the reference amplitude, expressed as a dotted line in Fig. 9.6(b). The power transmission in the cutoff region of the LPF is measured at about 35 dB, as shown by the red line. The experimental result is in good agreement with the FDTD simulation, which is represented with a black line in Fig. 9.6(c).

.

Chapter X.　THz band gaps induced

by metal grooves inside TPPWG

In Chapter VI and VIII, we induced several interesting band gaps using metal 1-D (defect) slit arrays positioned at the center of the air gaps in TPPWGs. And we tried to apply the each band gaps to THz filters, LPF, (tunable) notch filter and gas sensor for THz applications. In this Chapter, we report on the characteristics of band gaps by using *metal grooves* which are located inside the flare PPWG. The properties of band gap and defect mode using a groove structure were done by the Grischkowsky group [23,60]; however, the depth of grooves was very small compared to the air gap and wavelength. So, they can not have the standing-wave cavity mode (SWCM) with such a small depth and can not well explain the forming mechanism of band gaps with the mode matching analysis. By using the grooves with a deep depth, we investigate several interesting band gaps which have the different origin in forming mechanism by experimental and FDTD simulation studies. And then, we try to apply the each band gaps to THz filters, LPF, (tunable) notch filter and microfluidic sensor for THz applications.

10.1 Experiment setup
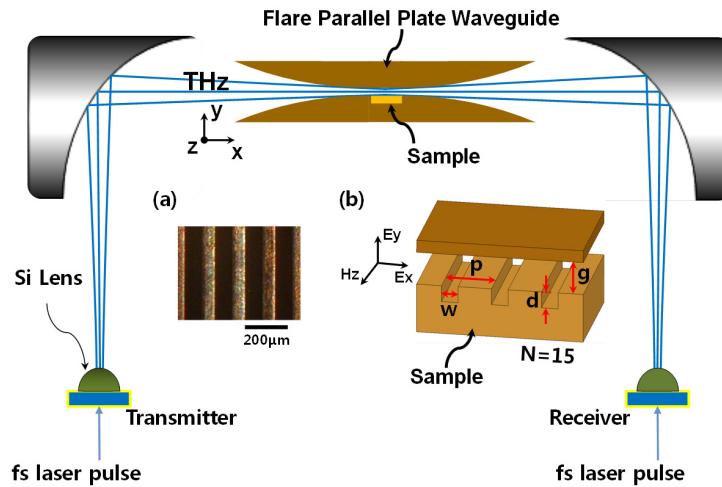
Figure 10.1 Experimental setup: (a) Photo image of grooves. (b) Geometry of grooves. The period (p) is 142 μm, the groove width (w) is 58 μm, the groove depth (d) is 84 μm, and the number of grooves (N) is 15.

The THz waveguide system used for our experiments is shown in Fig. 10.1. The groove used in the measurement has a 84-µm depth (d), 58-µm width (w), and 142-µm period (p) with 15 grooves (N). The copper sample plate with a groove pattern is made by a deep etch X-ray lithography method. A vertically (y-direction) polarized THz beam is focused into the air gap by a flare PPWG which is also made of copper. A solid flare PPWG comprises of two areas, namely, a smoothly curved metal flare area and a flat area in the middle of the waveguide. The PPWG enables simple and precise measurement. The 40-mm wide (z-direction) and 12-mm length (x-direction) copper groove sample plate is embedded into the flat area of the lower waveguide. To reduce the boundary effect between the groove sample plate and the PPWG, a 16-µm thick thin aluminum foil covers the boundary. The grooves exist on only half of the copper groove sample plate to measure the output THz signal. The other half of the plate has no grooves in order to measure the reference THz signal. Therefore, the waveguide with the copper groove sample plate in one unit is moved in the z direction to measure the reference and output THz signals, and this can reduce system errors.

10.2 Experiment results
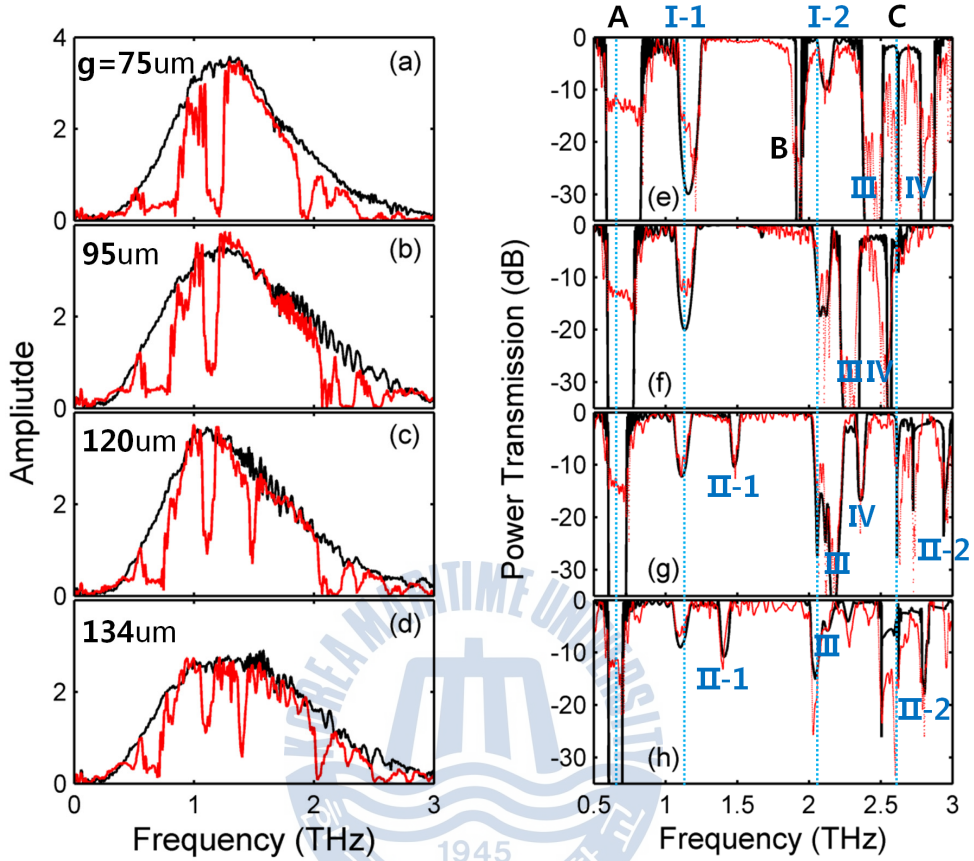
Figure 10.2 (a)-(d) Measured THz spectra with various air gaps. The black and red lines indicate reference and output spectra. (e)-(h) Comparison of measured power transmission spectra (red) and FDTD simulated power transmission (Black) for spectra (a)-(d), respectively. The Roman numerals I, II, III, and IV and letters A, B, and C are used to distinguish the source of band gaps from multiple grooves and single groove, respectively.

Four different air gaps, with g = 75, 95, 120, and 134 µm were used to study the characteristics of the band gaps. Figures 10.2(a) to (d) show the spectra of each measured THz pulse. The measured 66 ps data was extended to 1320 ps by adding zeros at the end of the data. And the frequency resolution is 0.75 GHz. The upper black curves and lower red curves indicate the reference pulse spectra without grooves and the output spectra with grooves into the PPWG, respectively. The TM_1 modes are detected as shown in the rapid oscillations in the reference and output

spectra, especially large air gaps due to the imperfect odd mode of the THz field in the air gap. A 16-µm thick aluminum foil layer is used to cover the boundary between the groove sample plate and waveguide, which creates the imperfect odd mode in the air gap. However, the TM_1 mode oscillation is small enough compared to the output resonances. The position and amplitude of the output resonances are gradually changed as the air gap increases. The measured power transmission spectra and FDTD simulation are shown in Fig. 10.2(e) to (h), which show the variations of band gaps with increasing air gap. The waveguide blocks and groove structure are define as perfect electrical conductors in the FDTD simulations. The measured and simulated results show good agreements. The Roman numerals I, II, III, and IV and letters A, B, and C are used to distinguish two groups of resonances. The band gaps of the Roman numerals group, as simulations will show, come from multiple grooves and the band gaps of the letters group originate from the first single groove. The vertical dashed lines indicate the constant band gap frequency with increasing air gap.

Band gap A has a narrow width but its center frequency is constant with increasing air gap. However, band gap B appears only for the 75-µm air gap. Band gap C displays a very narrow spectral width and its position remains unchanged with increasing air gap. The amplitude of band gap I-1 is decreased with increasing air gap, but that of band gap I-2 is changed little. Band gaps II-1 and II-2 are seen in 120-µm and 134-µm air gaps only. Band gaps III and IV both move to a low frequency range with increasing air gap. To understand the characteristic of the band gaps, FDTD simulation is used.

10.3   FDTD simulations : Multiple Grooves vs Single Groove
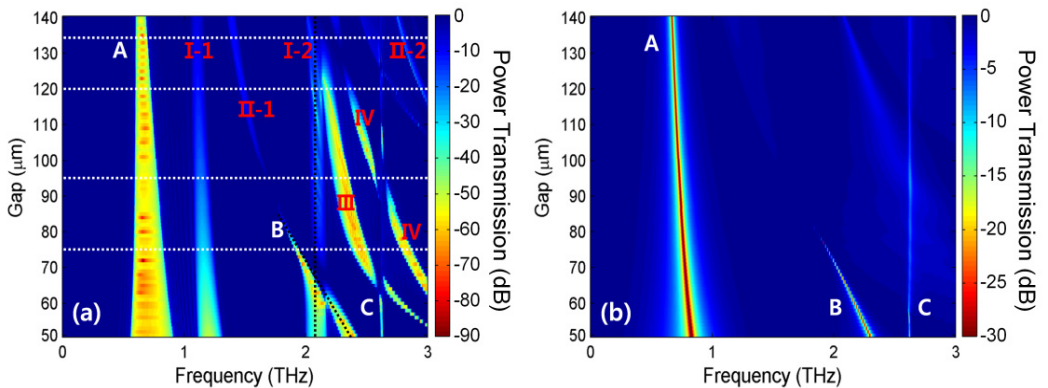
Figure 10.3   (a) 2-dimension FDTD simulations for 15 grooves. The air gaps used in the measurement are indicated by horizontal white lines. The vertical and inclined dotted lines indicate band gap I-2 and band gap B respectively. (b) 2-dimension FDTD simulations for single groove.

Figure 10.3(a) shows FDTD simulation results for the 15 grooves used in the measurement with various air gaps. The air gaps used in the measurement are indicated by horizontal white lines. Figure 10.3(b) shows another FDTD simulation for a single groove with various air gaps, which shows only A, B, and C band gaps in contrast with many more peaks in the multiple grooves sample. The A and B band gaps of the single groove have narrower widths and smaller power transmission than those of multiple grooves because the specific wavelength component of THz pulses involves the first groove. However, band gap C has a very narrow band gap width for both multiple and single groove. Except band gaps A, B, and C in Fig. 10.3(a), band gaps I, II, III, and IV come from the multiple grooves. As the air gap increases, the frequencies of band gaps A, C, and I are fixed to the resonance frequency, which means a specific wavelength is involved to the each resonance. The other band gaps, namely, B, II, III, and IV shift to a lower frequency range with increasing air gap.

dCollection

10.4 FDTD simulations : Band gaps A~C and I~IV
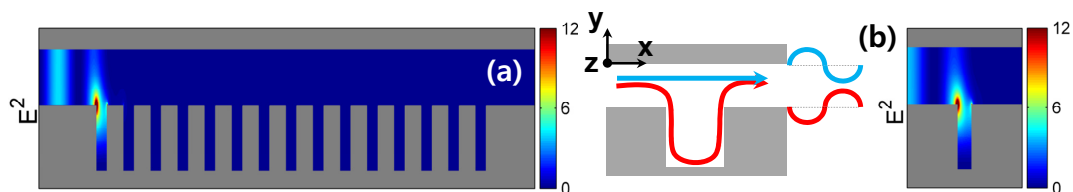
Figure 10.4   E field intensity (a),(b). (a) Band gap A at 75-μm air gap with 0.7 THz single frequency. The diagram shows the out of phase state between the detour (red arrow) and straight (blue arrow) propagated THz fields. (b) is identical with (a) but for single groove.

Band gap A can be explained by the THz field being canceled out between the straight propagated THz field by the air gap and the detour (reflected) THz field by the first grove. The incident THz field is separated into three parts at the first edge of the groove, namely: transmission, reflection, and splitting. The split THz field to the down side (-y direction) is reflected from the groove bottom and then splits again at the second edge of the groove and goes to the output direction (x direction) with the propagated THz field through the air gap. The phase difference between the detour THz field by splitting and propagated THz field through the air gap is π radian at the band gap A. Because the two THz fields are out of phase, the two combined THz fields disappear after the first groove as shown in Fig. 10.4(a). The diagram in Fig. 10.4(a) shows the out of phase state between the detour and straight propagated THz fields. Figure 10.4(b) show the E field intensity when the condition of simulation are identical with Fig. 10.4(a), except that the simulation is performed for the single groove sample.
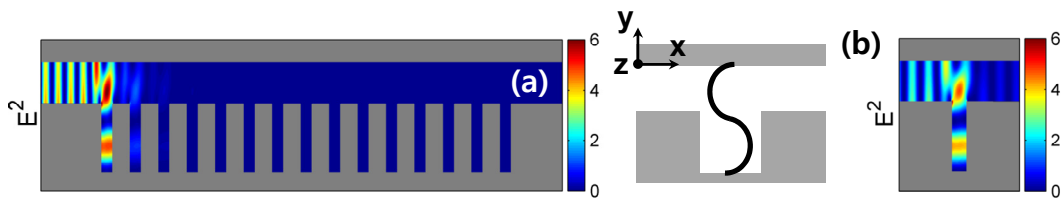
Figure 10.5 E field intensity (a),(b). (a) Band gap B at 51-µm air gap with 2.37 THz single frequency. The diagram shows vertically localized standing-wave. (b) is identical with (a) but for single groove.

Unlike band gap A, the position of **band gap B** shifts to a low frequency range with increasing air gap up to approximately 80 µm. When the air gaps are 50 µm and 75 µm, the band gap frequencies are 2.295 THz and 1.948 THz, respectively, corresponding to the wavelengths of 130.7 µm and 154 µm, respectively. These wavelengths are the same as the length summation of the air gap height (g) and groove depth (d). Therefore, the frequency of the band gap B, which we name vertically localized SWCM, is defined as c/(d+g), where c is the speed of light and the depth d=84 mm. Figure 10.5(a) shows the localized THz field which mainly exists near the first groove and the diagram of vertically localized standing wave. Only a small fraction of the incident THz field is propagated to the second groove. Therefore, the resonance frequency component of the band gap B cannot be detected at the end of multiple grooves. When only the air gap is smaller than the depth of the groove (g < d), the vertically localized SWCM exists in the groove as shown in band gap B of Fig. 10.3(b). When the air gap increases, the band gab B shifts to lower frequency range corresponding to longer-wavelength standing wave. If the air gap is larger than the depth of the groove (d=84 µm), the THz field energy at the air gap is larger than the THz field energy in the groove. Therefore, the THz field cannot be localized in the groove. Figure 10.5(b) show the E field intensity when the condition of simulation are identical with Fig. 10.5(a), except that the simulation is performed for the single groove sample.

Collection
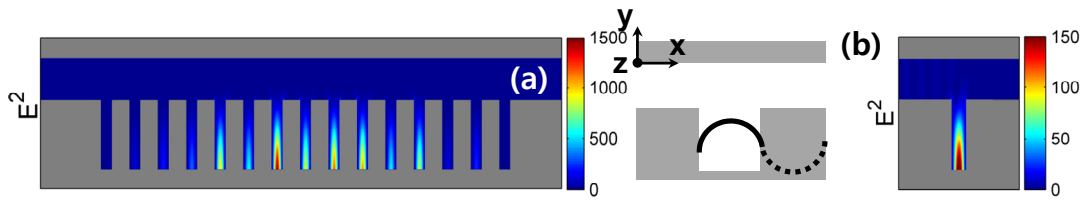
Figure 10.6   E field intensity (a),(b). (a) Band gap C at 51-µm air gap with 2.625 THz single frequency. The diagram shows horizontally localized standing-wave. (b) is identical with (a) but for single groove.

Band gap C is another SWCM where the field is horizontally localized in the groove cavities. The field is confined between both side walls and the bottom of the groove as shown in Fig. 10.6(a). Since the band gap frequency of a horizontally localized SWCM is determined by twice the groove width, the mode frequency is independent of the air gap. The diagram in Fig. 10.6(a) shows the wavelength of a horizontally localized SWCM in a groove. The groove width in the experiment was 58 µm which corresponds to the 2.62 THz band gap frequency as shown in the band gap C of Figs. 10.3(a) and (b). After the horizontally localized SWCM forms at the first groove, like band gap B, some of THz field is propagated to the second groove. The propagated THz field makes another horizontally localized SWCM at the next groove and so on. The THz field at the horizontally localized SWCM cannot arrive to the end of the groove. Therefore, the power transmission of multiple grooves is smaller than that of a single groove. The field is localized in some of multiple grooves, but the other grooves are not exist the field as shown in Fig. 10.6(a). Because we used single frequency for the simulation, the phase of an incoming THz field is periodically changed such as +, 0, and -. Therefore, the horizontally localized SWCM repeatedly appears and disappears in the grooves. Figure 10.6(a) shows a snapshot when E field in the grooves is at a maximum. The THz field energy is accumulated in the grooves until saturation because of the equilibrium between incoming and leaking THz field energy. The maximum E field intensity in the grooves is about 1400 times higher than the E field intensity in the input channel. Figure 10.6(b) show the E field intensity when the condition of simulation are identical with Fig. 10.6(a), except that the simulation is performed for the single groove sample.
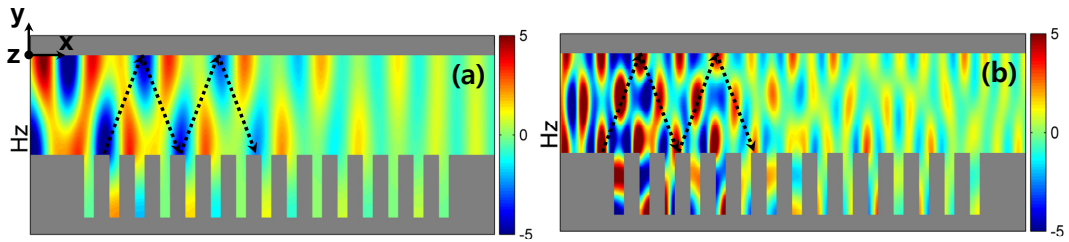
Figure 10.7 H_z field (a),(b) distribution in grooves. (a) Band gap II-1 at 134-μm air gap with 1.4 THz single frequency. (b) Band gap II-2 at 134-μm air gap with 2.8 THz single frequency.

Meanwhile, band gaps I-1 and I-2 show Bragg band gaps which are given by mc/2p, where m is an integer, and p is the period of the groove. Because **Bragg band gaps** depend only on the period of grooves, not the air gaps, the first and the second Bragg band gap frequencies are always located around 1.06 THz and 2.11 THz, respectively, as show in Fig. 10.3(a). **Band gaps II, III, and IV** are caused by the π radian delay (out of phase) between the THz field reflected by the grooves and the THz field propagated through the air gap. Figures 10.7(a) and (b) show the magnetic field Hz field distributions of band gaps II-1 and II-2, respectively. The Hz field pattern repeats every 3rd grooves. After two or three repetitions of the patterns (point of view), the polarity of the field uniformly distributes to the y direction that makes out of phase to the THz field directly propagated through the air gap. Therefore, band gaps II-1 and II-2 have air gap dependent characteristics. The Hz field pattern of band gap II-2 is the same as that of band gap II-1 except the wavelength. Because the wavelength of band gap II-2 is half as long as that of band gap II-1, the position of band gap II-2 is located at a frequency two times higher as shown in Fig. 10.3(a). Band gaps III and IV have an out of phase mechanism which is similar to that of band gap II, but it shows very complicated and irregular field patterns. Many band gaps also come out after 3 THz ; however, more study is required to understand the higher frequency band gaps completely.

- 107 -

This work has demonstrated the characteristic of band gaps using metal grooves in a flare PPWG with increasing air gap. The observed vertically and horizontally localized SWCMs in measurement showed good agreement with the FDTD simulations. Vertically localized SWCMs only exist when the air gap is smaller than the depth of the groove (g < d). Horizontally localized SWCMs depend only on the groove width, not the air gap. Since the band gap width of horizontally localized SWCM is so narrow, it is recommended to be used as a notch filter with very high quality factor. The grooves function as THz field energy containers for SWCMs. Other band gaps except Bragg band gaps can be explained by the field being canceled out by the out of phase between detour THz fields reflected by grooves and/or air gap and THz fields propagated through air gaps. Next Chapter, we show the applications of groove structures as THz filters or THz sensors.
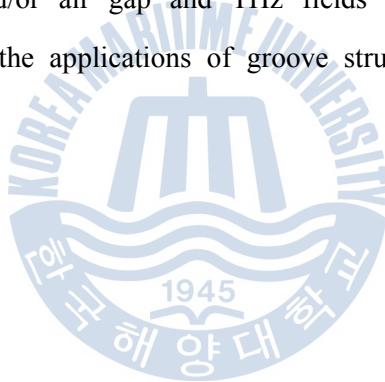
Chapter XI.   Application for THz filter and sensing based on band gaps properties by using metal grooves in TPPWG

THz notch filters have been demonstrated using slits inserted in the tapered PPWG with the TEM mode propagation in Chapter IX. The main advantages of the TEM mode compared to the TE_1 mode [30,65] are that there are no cutoff frequency and no group velocity dispersion. Because of no cutoff frequency, the resonant frequency of the notch filter can be located along the entire THz bandwidth, which leads to a wider tunable range for the THz notch filter. Another advantage is that the lack of group velocity dispersion can lead to short THz pulse ringing after the main THz pulse in the time domain, which makes it possible to perform a short scan.

In order to make a THz notch filter using a single groove, the THz band gaps caused by localized standing-wave cavity modes have to be removed. In this study, we successfully removed the localized standing-wave cavity modes using a wider and shallow single groove compared to the multiple grooves used in an earlier study (Chapter X). Moreover the frequency of notch filter was very sensitive according to the air gap variation in the PPWG, leading to a feasibly tunable THz notch filter. In this Chapter, we report a THz notch filter that is tunable by adjusting the air gap as well as the application of a microfluidic sensor filled with liquid in a single groove that is embedded in the PPWG.

11.1   Experimental setup : Notch filter
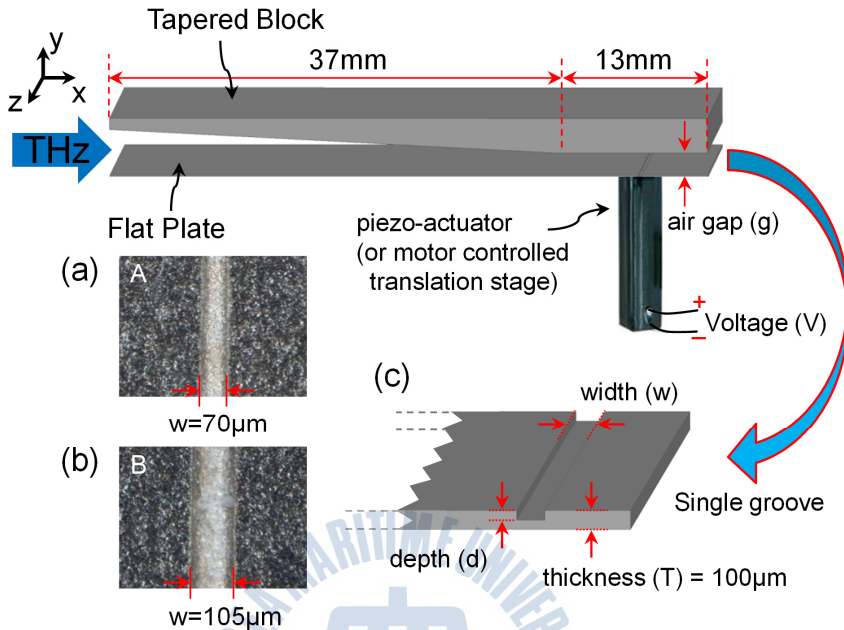
Figure 11.1   Schematic diagram of the PPWG. A single groove is embedded into the lower flat plate, which is attached to a piezo-actuator (or a motor-controlled translation stage). (a, b) Optical micrograph of the single groove. Samples A and B show 70 and 105-μm groove widths and 28 and 40-μm groove depths, respectively. (c) Expanded view of the groove.

Figure 11.1 schematically shows the tunable THz notch filter setup, which is composed of a tapered aluminum block and a flat stainless plate with a single groove on the surface. The tapered aluminum block consists of a tapered area with a 3° angle and a flat area. A flat stainless plate, which is the lower part of the PPWG, has dimensions of 50 mm (length), 24 mm (width), and 100 μm (thickness). The single groove, fabricated by a micro-photochemical etching method, is embedded in the flat plate. The single groove is located 6.5 mm from the right edge, which is in the middle of the 13 mm flat surface of the upper plate. Because a vertically polarized (y-direction) THz field propagates to the PPWG, only

TM modes exist.

We prepared two types of single grooves. Sample A has a 70 µm wide and a 28 µm deep groove, and sample B has a 105 µm wide and a 40 µm deep groove, as shown in the image in Fig. 11.1(a,b). Figure 11.1(c) shows the definition of the depth and width of the groove. A motor-controlled translation stage is connected to a flat stainless plate to adjust the air gap of the PPWG, and the tapered aluminum plate is fixed. After measuring the notch filter properties, we replaced the motor-controlled translation stage with a piezo-actuator in order to adjust the air gap using a DC voltage source, as shown in Fig. 11.1.

The THz notch filter can be obtained by inserting a single slit into the middle of the PPWG air gap (Chapter IX). The THz notch filter by the single slit can be tuned by adjusting the two air gaps split by the slit. Because the slit is located in the middle of the waveguide air gap, the upper and lower air gaps have to have identical spaces in order to realize the notch filter. This requires a complete experimental setup and a very precise adjustment of both air gaps at the same time. The experimental setup for the single groove, however, provides a much simpler method to make a tunable THz notch filter because there is only one air gap, which can be controlled by one of the PPWG plates. And unlike the slit, the groove can contain a liquid that can be applied to a THz microfluidic sensor.

11.2   Experimental results : Tunable Notch filter
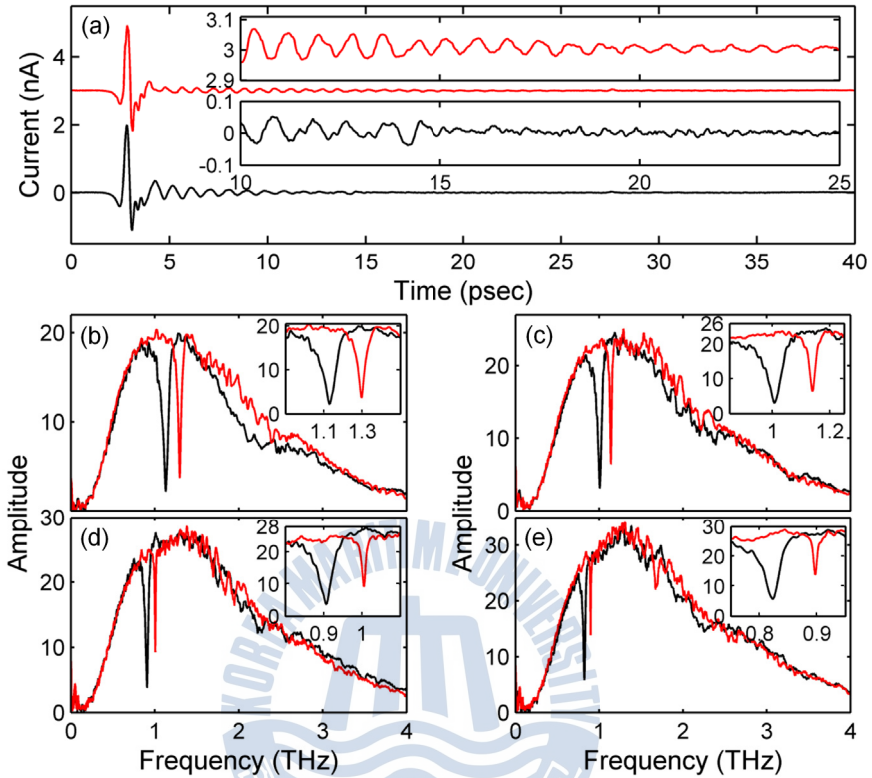
Figure 11.2   (a) Measured THz pulses (sample A: upper red, sample B: lower black) for 100-μm air gap. The inserted figures show the expanded THz ringing from 10 to 25 ps. (b)-(e) Spectra of the measured THz pulses for 100-, 120-, 140, and 160-μm air gaps, respectively for samples A (red) and B (black). The inserted figures show expanded images of the resonances.

Figure 11.2(a) displays the measured THz pulses after propagating through the PPWG with a 100-µm air gap for samples A (upper red) and B (lower black). The images inserted in the THz pulses display the ringing related to the resonance of the notch filter existing after the main pulse. The ringing signal of the sample A has a bigger and longer signal than the sample B. The ringing signal indicates that the sample A has a stronger localized resonance dip and a higher Q factor compare to the sample B. Figure 11.2(b) to 2(e) show the amplitude spectra of the measured THz pulses with the 100-, 120-, 140-, and 160-µm air gaps, respectively,

dCollection |

for samples A (red) and B (black). When the air gaps are increased, the resonance frequencies shift to lower frequency region and also the resonance width gradually becomes narrower. Like the property of the notch filter resonance in the TE_1 mode [12], that in the TEM mode is also excellent. The resonant frequencies of samples A and B for 100-µm air gap are 1.29 and 1.13 THz, respectively. Because the groove of sample B is wider and deeper than that of sample A, the resonant frequency exists in a lower frequency range. Unlike the TE_1 mode, which has a cutoff frequency, the notch filter resonances of the TEM mode can be obtained for the entire frequency region by adjusting the air gap.
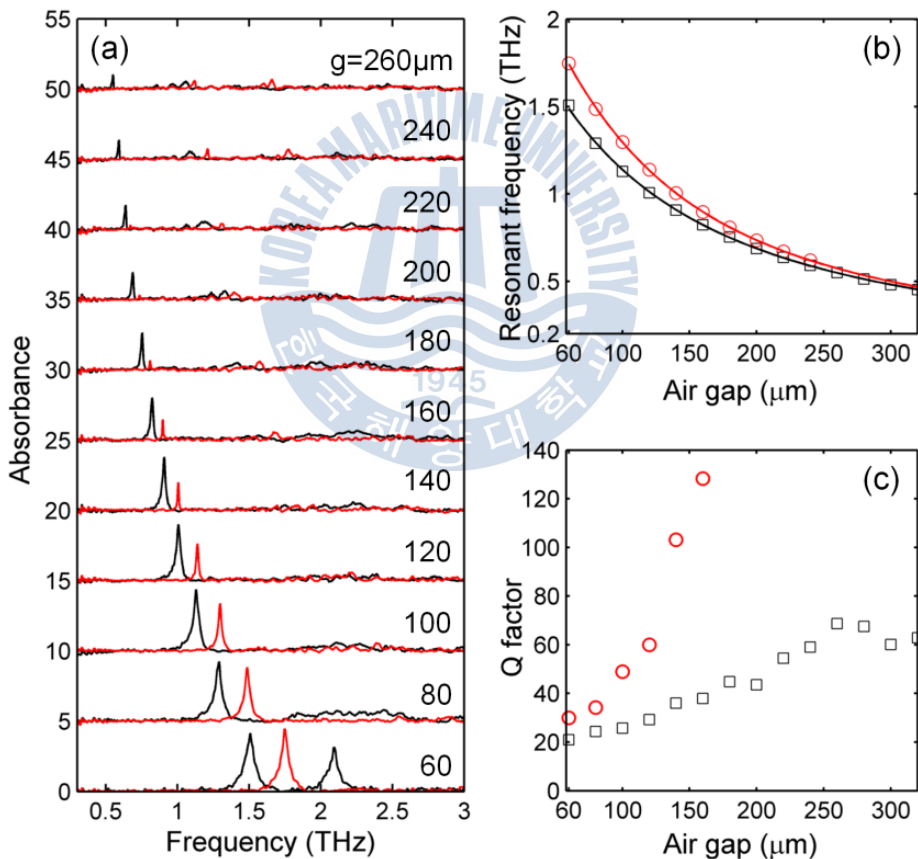
Figure 11.3   (a) Absorbance spectra in sample A (red) and B (black) for variation air gaps from 60 to 260-µm. (b) The resonant frequency shift of the notch filters according to the air gaps. The solid lines are numerical fitting lines. Red circles and black squares indicate sample A and B, respectively. (c) Q-factors of the notch filter resonances according to air gaps.

Figure 11.3(a) shows the absorbance of the notch filter resonance with different air gaps ranging from 60 to 240 µm. The resonant frequency shifts to a low frequency range and the absorbance becomes small with an increase in the air gap because the THz field (energy) in the groove becomes weaker compared to the THz field in the air gap according to increase in the air gap. When the air gap is large enough compared to the groove depth, most of the THz field is distributed into the air gap. Therefore, an out-of-phase (phase mismatch) condition does not (or does only very weakly) arise between the incoming THz field and the reflecting THz field from the bottom of the groove. The second resonance of sample B with an air gap of 60 µm is shown to be at 2.09 THz. The second resonance is related to the localized standing-wave cavity mode. When the air gap is wider than the groove width and the groove depth is small enough compared to the groove width, the localized standing-wave cavity mode does not occur, as shown in sample B in Fig. 11.3(a), with an 80-µm air gap. The resonant frequencies of the notch filter of sample A are 0.62 and 1.75 THz when the air gaps are 240 and 60 µm, respectively. Therefore, the tunable sensitivity of the THz notch filter is 6.28 GHz/µm, which is compared to 1.36 GHz/µm obtained from one of the THz notch filters shown in Fig. 10.3(b) from Chapter. X. Figure 11.3(b) shows the resonant frequency shift according to the difference in the air gap when it ranges from 60 to 240 µm for sample A and from 60 to 320 µm for sample B. The solid lines indicate the numerical fitting lines, which are defined as

$$f_r(g) = \frac{c}{2 \times [d_{eff}(g) + g]}, \tag{1}$$

where c is the speed of light in a vacuum; g is the air gap; and d_{eff} is the effective groove depth, which is defined as (d - $\Delta d(g)$). Also, $\Delta d(g)$ (shown in Fig. 11.4(g)) is the height from the groove bottom, which has a very weakly distributed THz field compared to the space above of the groove. Therefore, the

height is not considered to determine the effective groove depth. When the air gap is much smaller than the depth, the strong THz field in the groove is fully distributed at the bottom of the groove. Therefore, the entire groove depth contributes to the realization of the effective height ($h_{eff} = d_{eff} + g \approx d + g$), where $\Delta d(g) \approx 0$ and $d_{eff} \approx d$. Meanwhile, when the air gap is large enough compared to the groove depth, most of the strong THz field is distributed in to the air gap; however, the THz field in the groove is very weak. For this reason, the effective height is only the air gap ($h_{eff} \approx g$), where $\Delta d(g) \approx d$ and $d_{eff} \approx 0$. According to our calculation, the value of $\Delta d(g)$ can be obtained by an exponential function. The groove depth is the important factor in determining the resonant frequency of small air gap; however, it is less important with a large air gap. For example, when the air gap is 60µm, the effective depths of sample A ($d_{eff} = 25.8$µm, where $\Delta d(g) = 2.2$µm) and B ($d_{eff} = 39.5$µm, where $\Delta d(g) = 0.5$µm) have ratios of about 30.1% and 39.7%, respectively, to the total heights ($d+g$). The resonant frequencies of sample A and B are 1.75 and 1.51 THz, respectively. On the other hand, according to the increase in the air gap, the resonant frequencies of both notch filters are nearly identical, as shown in Fig. 11.3(b). For example, when the air gap is 240 µm, the effective depth of sample A ($d_{eff} = 1.8$ µm, where $\Delta d(g) = 26.2$µm) and B ($d_{eff} = 14.2$ µm, where $\Delta d(g) = 25.8$µm) have ratios of 0.7% and 5.6%, respectively, to the total height ($d+g$). The resonant frequencies of sample A and B are 0.62 and 0.59 THz, respectively. Figure 11.3(c) shows the relationship between the air gap and the Q factor, which increases with an increase in the air gap. Sample A has a greater Q factor than sample B because it has a smaller groove depth. The maximum Q factors of sample A and B reach about 128 and 69, respectively, which can be compared to the value of 138 as obtained with the single slit in the PPWG in Chapter X.

11.3　FDTD simulations : Tunable Notch filter
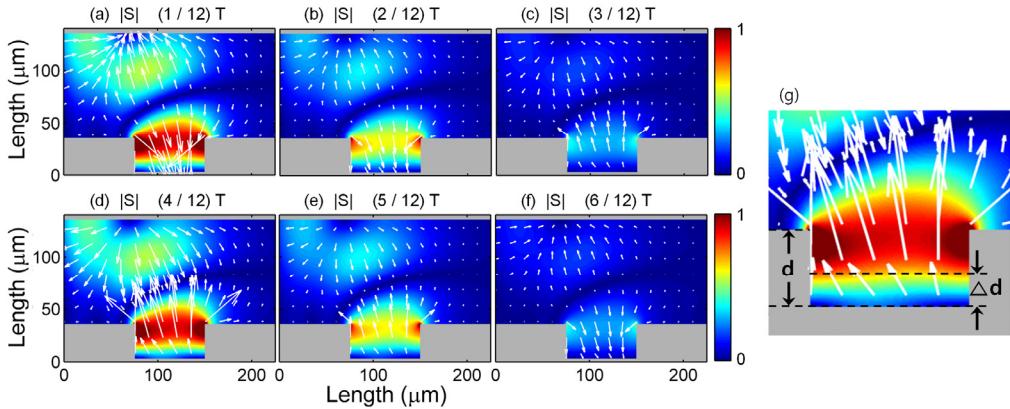
Figure 11.4　Poynting vectors around the groove (sample A) for an air gap of 100 μm and a resonant frequency of 1.29 THz. (a)-(f) Each frame shows a 1/12 time period. (g) An enlarged graph of (d) in which Δd is 12.5 μm for an air gap of 100 μm.

To determine the directional energy flux density of a THz field, Poynting vectors are used, as shown in Fig. 11.4; these show the FDTD simulations considered with a resonant frequency of 1.29 THz, a groove depth of 28 µm (sample A), and an air gap of 100 µm. Each figure shows a 1/12 time period of T, which is equal to 1/wavelength. The figure shows only six frames, which make up a half period of T. After finishing the half period of T, the Poynting vectors repeat the cycle from Figs. 11.4(a) to 11.4(f) with an E-field phase shift of 180°. The two opposite directions of the Poynting vectors oscillate in the space between the groove bottom and the upper surface of the PPWG. The energy flux density is confined in this space. The energy density of the other frequencies moves to the output-side PPWG; however, only the energy density of the notch filter frequency is unable to go to the output-side PPWG. This situation makes the notch filter resonate at the measured THz bandwidth. The process of building up the notch filter resonance by the single groove is identical to that of the single slit measurement in Chapter X; the only difference is the THz field reflection by the groove bottom and the THz field passing through the slit. When the THz fields are reflected from the metal

- 116 -

waveguide surface or the groove bottom, which are considered as perfect conductors in the THz frequency region, the images of the THz fields exist inside the metal. According to image theory, the THz field pattern in the groove waveguide is identical to that in the folded THz field halfway along the horizontal center of the slit. Therefore, the formation of notch filter resonance by the single groove can be explained in terms of the resonance of the single slit.

11.4   Application for tunable Notch filter using Piezo-actuator
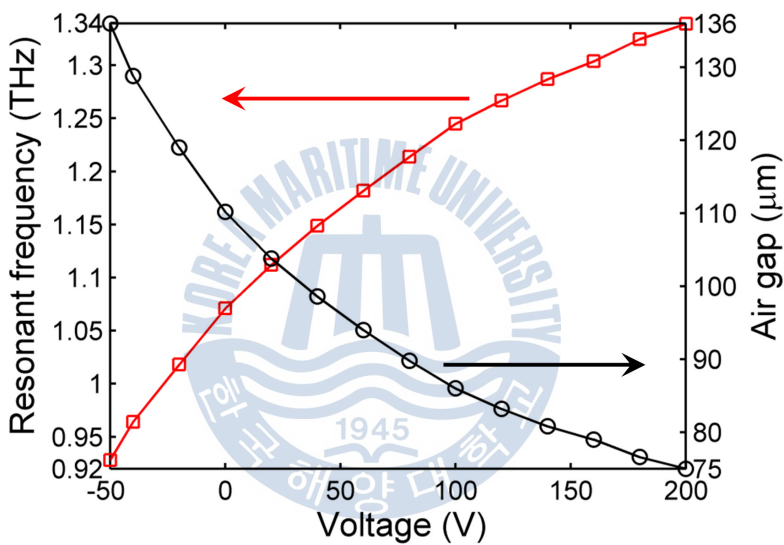
Figure 11.5   Measured voltage-dependent resonant frequencies of notch filter (red squares) and air gaps of PPWG (black circles) when one end of piezo-actuator is attached to the flat plate.

Because the weight of the flat stainless plate is only 0.95 g, the piezo-actuator can support the plate. Instead of mechanical movement by the motor-controlled translation stage, the piezo-actuator makes its length longer and shorter by controlling the DC (or AC) voltage supplied to the piezo-actuator. Therefore, the motor-controlled translation stage is replaced by the piezo-actuator, which is 30-mm long (Piezomechanik, model No. PSt-HD 200/7x7/40), as shown in Fig. 11.1.

Figure 11.5 shows the notch filter resonance variations (red squares) and air gap variations (black circles) of sample B according to the DC voltage supply. Due to the limited length of the piezo-actuator, it increases to 61 µm when the voltage changes from -50 to +200V. The resonance variation of the notch filter ranges from 0.92 THz to 1.34 THz, which is in very good agreement with the data shown in Fig. 11.3(b). The frequency-tuning sensitivity (FTS) is given as $\Delta f/\Delta V$, where Δf is the resonant frequency shift and ΔV is the voltage variation. The calculated FTS is 1.67 GHz/V, which shows that a piezo-actuator can use a tunable notch filter device. Because most piezo-actuators have hysteresis characteristics, they require additional controlling equipment to set the position and to control the velocity.

11.5   FDTD simulations : Application for THz Microfluidic Sensor
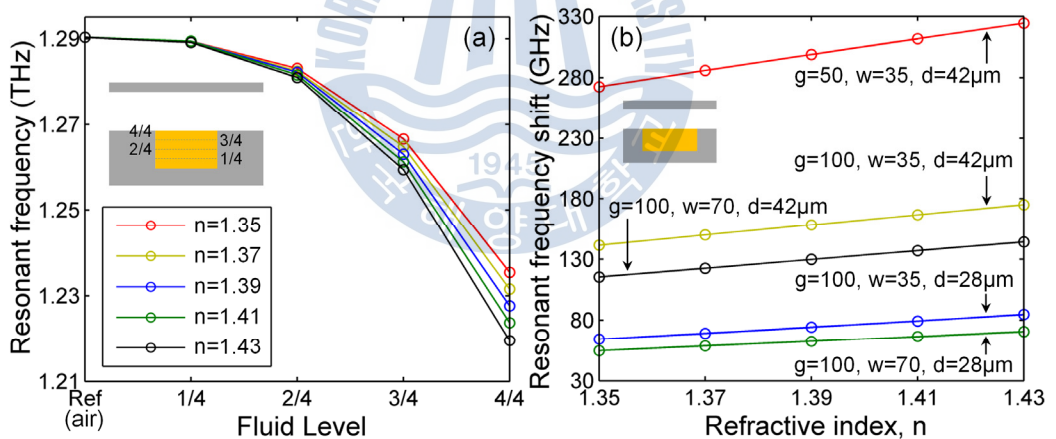
Figure 11.6   (a) The resonant frequencies of the notch filter for four different fluid levels with different reflective indexes. (b) The resonant frequency shift for different sample conditions when the groove is fully filled with liquid.

The THz microfluidic sensor is one example of applying the notch filter resonance [30]. Using FDTD simulation, we attempted to calculate the resonance shift for liquid samples that had different reflective indexes ranging from 1.35 to 1.43 based

on liquid alkanes [66]. Figure 11.6(a) shows the variation of the resonant frequency for four different fluid levels in the groove of sample (A) with a 100 µm air gap. If the liquid level is increased, the sensitivity of the resonant frequency is also increased. When the groove is fully filled with the liquid, the resonant frequency deviation (Δf) is 16 GHz between the reflective indexes of 1.35 and 1.43. The sensitivity is $\Delta f/\Delta n$ = 162.5 GHz/RIU, where RIU is the refractive index unit. The groove depth, the groove width, and the air gap are important factors when seeking to increase the sensitivity, as shown in Fig. 12.6(b). For example, if the groove width and the groove depth are changed to 35 µm (50% decrease; blue line) and 42 µm (50% increase; black line), respectively, the sensitivity levels increase to 255 GHz/RIU and 360 GHz/RIU. When both the width and the depth are changed (yellow line), the sensitivity is increased to 420 GHz/RIU. In this case, if the air gap is reduced from 100 to 50 µm (red line, Δf = 52 GHz), the sensitivity increases to 650 GHz/RIU, which is an increase of four times compared to the ordinary sample condition (green line). This simulation shows that, as in the TE mode, in the TEM mode it is possible to fabricate a THz microfluidic sensor. The advantages of this development are detailed in the introduction.

11.6   FDTD simulations : Low-Pass Filter and Band-pass filter

In this study, we implement low and band pass filters which are similar concepts in case of slit arrays in Chapter 9.5. Groove arrays used in filters are shown in Table. 11.1. Figure 11.7(a) shows the FDTD simulation results for Bragg stop bands and low (I~IX) and band (II~VIII) pass filters. Figure 11.7(b) shows images of some of the grooves in region II and region IX. Figure 11(c),(d) show when a 1.5 THz CW source propagate through low and band pass filters. In case of band pass filter (II~VIII), THz wave can propagate through groove arrays while low pass filter (I~IX) prevents the THz beam propagation.

Region	I	II	III	IV	V	VI	VII	VIII	IX
Period P [μm]	100	110	120	130	140	150	160	170	180
Width W / Depth D [μm]	60 / 22								
Number of grooves N [ea]	7								

Table 11.1 Dimensions of each region of grooves used in LPF and BPF. Each region has 7 grooves (N) and 60-μm width (w).
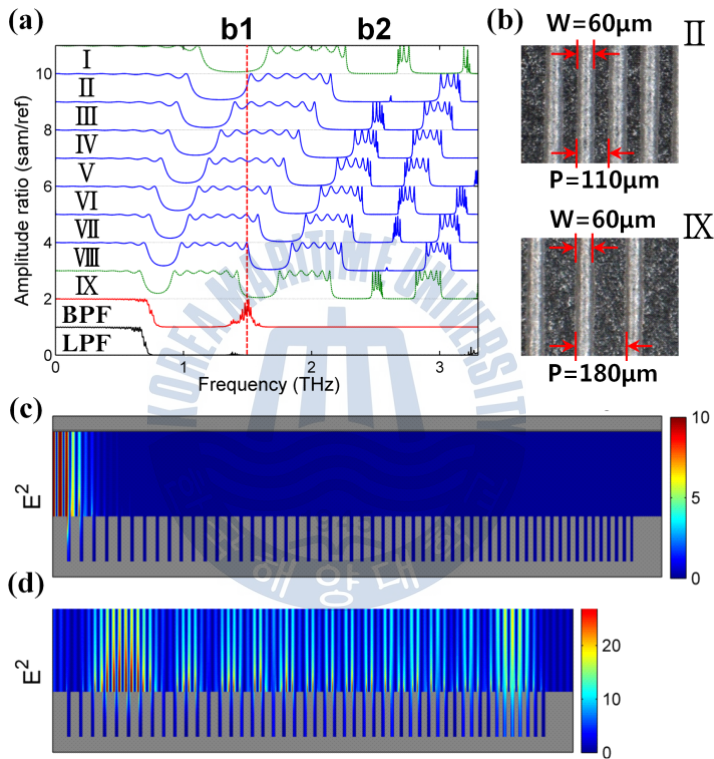
Figure 11.7 (a) Transmission ratio from region I to region IX and from LPF and BPF. The red vertical dashed line indicates 1.5 THz. (b) Slit images in region II and region IX. Areas I and from region III to region VIII are not shown in the figure because of limited space but these areas are continuously connected. (c),(d) FDTD simulation of E field intensity distribution for 1.5 THz continuous wave source for (c) LPF and (d) BPF. The air gap is 40 μm.

11.7   Experimental results : Low-Pass Filter and Band-pass filter
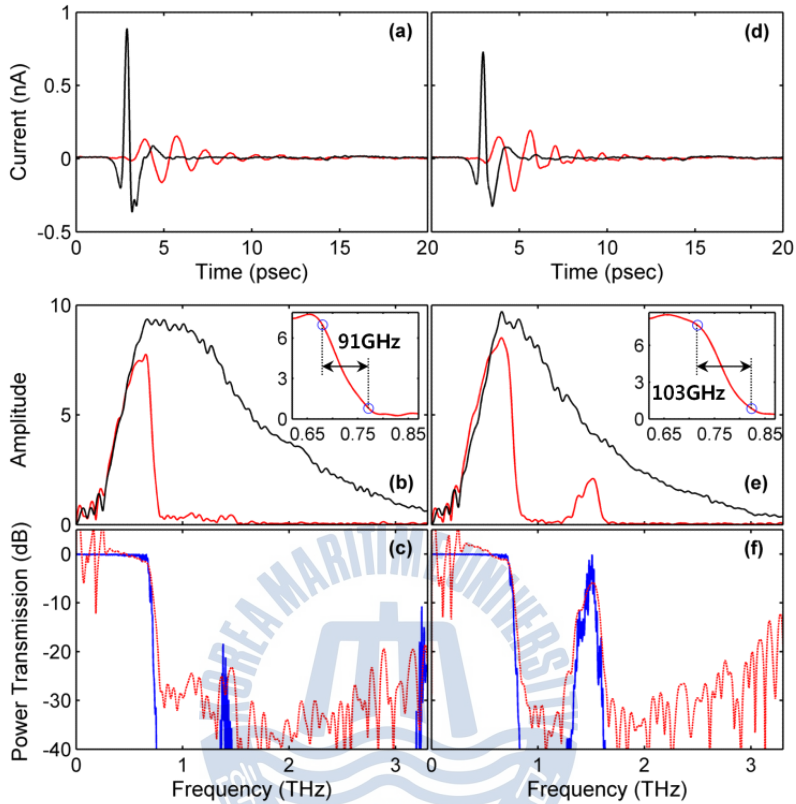
Figure 11.8 (a) Comparison of a THz reference pulse (black) without grooves and output pulse (red) with grooves in the waveguide plate. (b) The spectra of the reference (black) and output (red). The inset shows expended figure near the cutoff frequency. (c) Comparison of power transmission in the measurement (red) and FDTD simulation (blue). (d)-(f) identical to (a)-(c) but for the except I, IX groove groups. The air gap is 40 μm.

Figure 11.8(a,b,d,e) show the measured reference data (black) without grooves and output data (red) with grooves for low(a,b) and band(d,e) pass filter. The transition widths are about 91 (low pass filter) and 103 (band pass filter) GHz, respectively. And by removing the region I and IX of the groove groups, we made the propagating region (center f=1.514 THz, FWHM = 125GHz) inside the band gaps of low pass filter. And Fig. 11.8(c),(f) show the power transmission of the experimental data which is in good agreement with the FDTD simulation (blue line).

Chapter XII. Resonant transmission through slit arrays patterned parallel-plate waveguide

In this Chapter, we introduce a mechanism for resonant transmission through a new type of PPWG featuring two metal plates patterned with half-pitch offset slit arrays, which we call a *photonic PPWG*. In the preceding Chapters, we investigated various types of filters that use PPWGs with photonic crystals engraved with slits or grooves. These filters share the characteristic that the low-frequency region can only be cut off in the TE_1 mode, which results in pulses that are stretched over the time domain. In prior research, various circular and rectangular structures [8, 9], as well as photonic crystal waveguides, such as metalized cylindrical pillars [33], have been used to reduce transmission in low-frequency regions by means of cutoff frequencies for transverse magnetic (TM) and transverse electric (TE) modes.

In my opinion, we first demonstrate that the low-frequency transmission is decreased using the TEM mode in a PPWG which has no cutoff frequencies. This is caused by the well-known diffraction phenomenon of waves that longer wavelength tends to diffract more than those of shorter wavelength through the air slit arrays of this photonic PPWG structure. And we also introduce the new resonance phenomenon in a PPWG which has the resonance wavelength corresponding to the twice of the air gap size. So, the resonant frequency can be controlled by the air gap. Actually, this proposed structure has been studied in the millimeter waves [67], optics [68,69] and THz range [70,71], but they just considered when the air gap is filled with dielectric materials or air gap is too small compared with wavelength. So, they couldn't measure this resonance while they discussed the standing wave between the metal-metal and single metal regions

due to the impedance mismatch.

While the size of the air gap in a photonic PPWG governs the frequency of resonant transmission, waves of other frequencies will be diffracted through two slits arrays. Resonant transmission caused by slit array periodicity misalignment can be removed by placing a 20-μm gap between the two slit arrays, resulting in an open structure that can be controlled from outside via the air slit arrays. This new type of structure can be used in applications such as active filters and sensors.

12.1 Experimental setup : Photonic PPWG
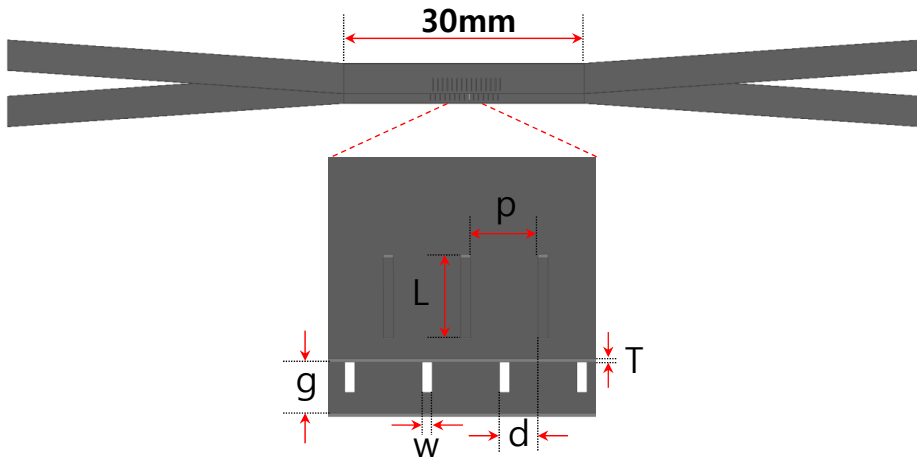
Figure 12.1   Diagram of photonic PPWG and slit arrays, air gap (g) = 90, 160μm, plate thickness (T) = 30 μm, slit width (w) / length (L) / period (p) = 65 μm / 11 mm / 500 μm, lateral shift (d) = 250 μm, N=15.

The experimental setup used in this study is illustrated schematically in Fig. 12.1. The photonic PPWG shown here is composed of two stainless steel metal plates μm period (p) and a 65-µm slit width (w). For the purpose of reference, the slits in the arrays are all engraved within the half-space of the metal plates. As the thickness of the metal plates (T) is only 30 µm, which is considerably less than that of a typical PPWG structure (a few micrometers), strictly speaking, this type of parallel-plate waveguide should be called a parallel-sheet waveguide . As shown in Fig. 12.1, we used two different air gap sizes (g = 90 and 160 µm) in our experiment and positioned the slit arrays of the two metal plates at a half pitch off-set (d = 250 µm). To increase the coupling efficiency of THz radiation into the sub-wavelength gaps, we sloped the tapered structure at a $4°$ angle using spacers located between the tapered parts but outside of the THz beam. On the basis of these specifications, we used a circular aperture with a diameter of 5 mm, corresponding to the height of the opened input piece (h = 5 mm). As the incoming THz beam was vertically polarized (i.e., in the y-direction), only TM modes existed within the PPWG.

12.2 Experimental results and FDTD simulation : Photonic PPWG
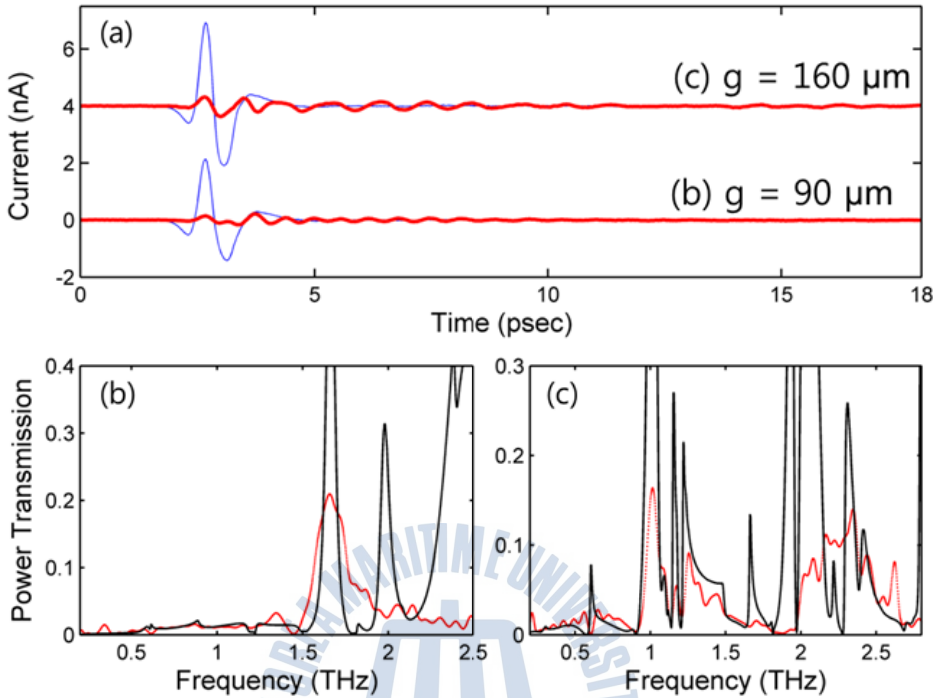
Figure 12.2　(a) Measured THz pulses with 90-μm and 160-μm air gaps. The blue and red lines indicate reference and output pulses. (b),(c) Measured power transmission spectra (red) and FDTD simulation (black) with (b) 90-μm and (c) 160-μm air gaps.

Figure 12.2(a) shows the measured reference THz pulses (blue) transmitting through a PPWG without slit arrays and the output THz pulses (red) from photonic PPWGs with air gaps (g) of 90 µm and 160 µm, respectively. The oscillation intervals of these output THz pulses are 0.601 (=1.664 THz, g=90 µm) and 0.954 (=1.048 THz, g=160 µm) ps, respectively, corresponding to resonant frequencies of 1.658 and 1.014 THz, as shown in Fig. 12.2(b),(c). The power levels transmitted by the measured THz pulses (red) and FDTD simulations (black) are shown in Fig. 12.2(b),(c) from which it can be seen that the first and second resonant transmission frequencies in each case are located at 1.658 THz (first, g=90 µm) and at 1.014 and 2.078 THz (first and second, g=160 µm), as given by the

- 125 -

resonant frequency :

$$f_{reso} = (m \cdot c)/(2 \cdot g), \tag{43}$$

where c is the speed of light, and m is an integer.

Although most THz energies are cut out at frequencies below the first resonance, in the FDTD simulation, there are several sharp resonances between the first and the second resonant frequencies that do not show clearly in the experimental results. Although we will further discuss this discrepancy later, overall, the measured and the simulated results are in close agreement.
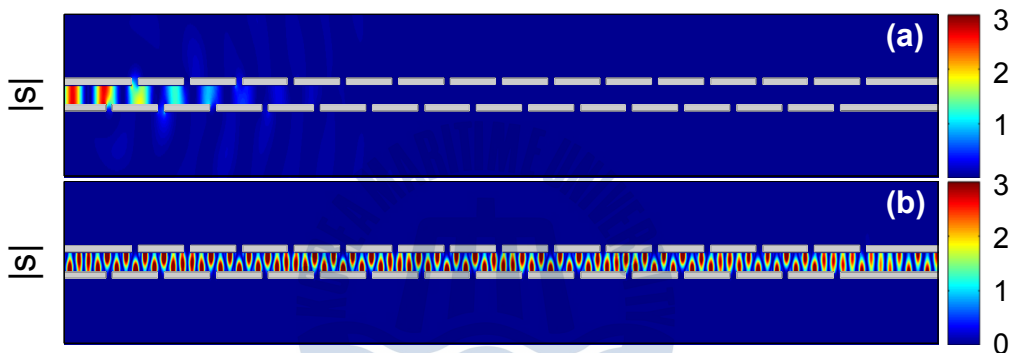
Figure 12.3   FDTD simulation of photonic PPWGs with a 90-μm air gap. (a) 0.5 THz ($f_{non-reso}$), (b) 1.65 THz (f_{reso}).

Figure 12.3 shows the magnitude of the Poynting vectors from (a) 0.5 and (b) 1.65 THz single sources transmitted through a 90-µm air gap. A detailed description of the photonic PPWG structure is provided in Chapter 12.1, whereas the measurement results are described in Fig. 12.2(b). As previously mentioned, resonant transmission generates a 1.65 THz signal (i.e., a signal at a wavelength corresponding to double the size of the 90-µm air gap). Figure 12.3(a) shows a non-resonant transmission (0.5 THz) that is diffracted through each slit, whereas Fig. 12.3(b) shows a THz resonant propagation having almost no diffraction through the slit arrays. To better understand the characteristics of the resonant transmission, we describe several FDTD simulations in Chapter 12.3.

12.3   FDTD simulations : Single slit and multiple slits
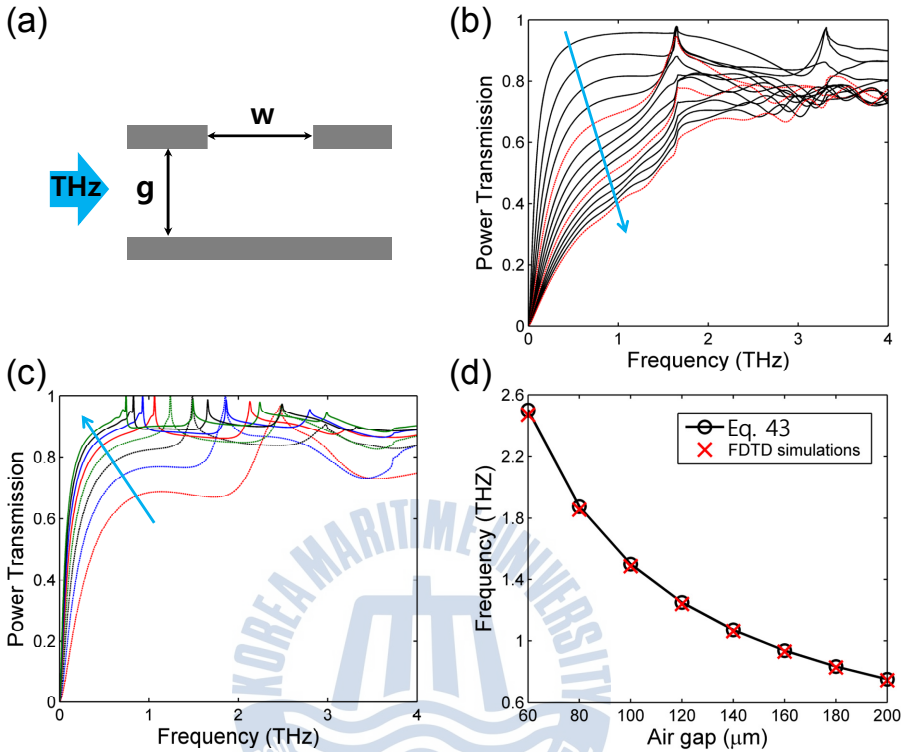
Figure 12.4   (a) Schematic diagram of a PPWG with single slit. Power transmission (b) when the air gap, g is 90 μm and slit width, w varies from 20 μm to 300 μm in step of 20 μm, (c) when the slit width, w is 65 μm and the air gap, g change from 60 μm to 200 μm in step of 20 μm. (d) The first resonant frequencies using FDTD simulations and Eq. 43.

We next analyze the properties of THz propagation by a single air slit perforated into the top plate of the PPWG, as shown in Fig. 12.4(a). The thickness of the plates used is 30 µm and because the polarization of the THz wave is perpendicular to the plates, TM modes are induced. Fig. 12.4(b) shows the FDTD simulation of power transmission at an air gap (g) of 90 µm for air slit widths (w) increasing from 20 to 300 µm in steps of 20 µm. Here, the red lines indicate slit widths increasing from 100- to 200- and then to 300-µm from the top, with

the blue arrow indicating increasing width. It can be seen that, as the slit width increases, the structure shows a resonant transmission property at 1.655 THz, corresponding to twice the air gap (g = 90 µm), and a second resonant transmission (3.313 THz) at twice the frequency of the first resonance, while the other frequencies are diffracted through the slit. However, after the slit becomes wider than approximately 120 µm the resonant transmission property disappears, while transmission in the high frequency region remains rather high and in an apparent state of saturation. As we have previously demonstrated similar resonant transmission properties with a single slit structure, Eq. (43) can be utilized in the case of a single-slit photonic PPWG. We also simulated power transmission for air gaps increasing from 60 to 200 µm in steps of 20 µm, as shown in Fig. 12.4(c), where the blue arrow indicates the increase in gap width. In order to retain a strong resonance phenomenon, the slit width in this simulation was fixed at 65 µm. The results show that when the air gap is small, low frequencies will be strongly diffracted, causing the resonance to become broad. As the air gap becomes larger, however, diffraction weakens and the resonance peak becomes sharp. Figure 12.4(d) shows the resonant frequencies (given by red crosses) seen in the FDTD simulations shown in Fig. 12.4(c), as well as the frequencies calculated from Eq. 43 (black circle); as expected, the simulated positions of resonant transmission at differing air gaps (g) correspond to the results of Eq. (43).
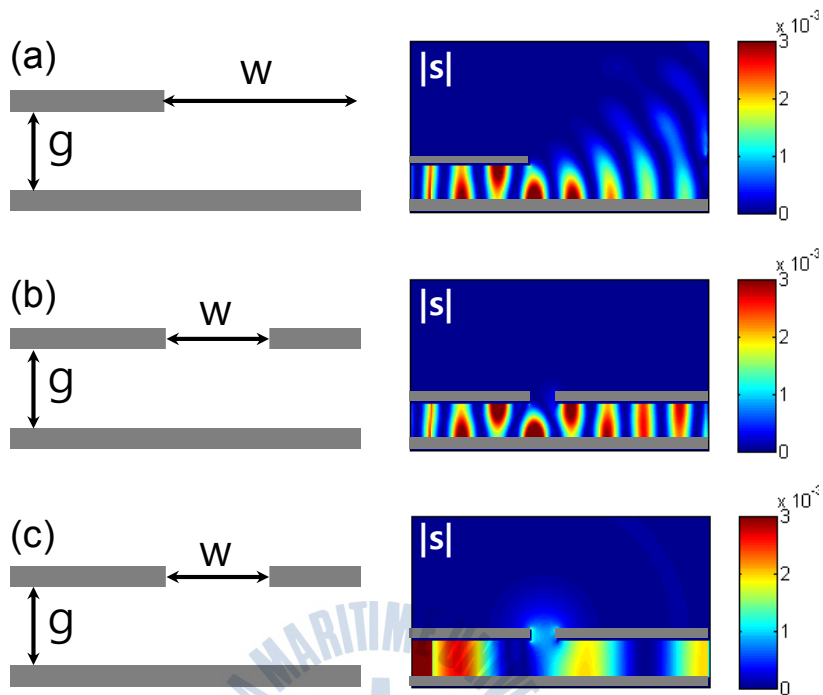
Figure 12.5 FDTD simulation with a 90-μm air gap and single slit. (a) Slit width is infinite and 1.65 THz (f_{reso}), (b) Slit width is 65 μm and 1.65 THz (f_{reso}), (c) Slit width is 65 μm and 0.5 THz ($f_{non-reso}$)

Fig. 12.5 shows the magnitude of the Poynting vector resulting from a 1.65 THz single source for three simulated parallel-plate cases in which there is a 90-μm air gap (f_{reso} =1.65 THz). In the first case, the top plate has an air slit with an infinite width, as shown in Fig. 12.5(a); here, the terahertz field becomes increasingly diffracted as it propagates along the plate. For a finite slit width (Fig. 12.5(b)), by contrast, a resonant terahertz field (1.65 THz) can propagate without being diffracted by the slit, and it appears to bounce between the separated plates. Figure 12.5(c) shows the magnitude of the Poynting vector at 0.5 THz (i.e., a non-resonant single frequency). Here, the diffracted terahertz waves can be seen to penetrate the air slit.

12.4 FDTD simulations : Misaligned photonic PPWG
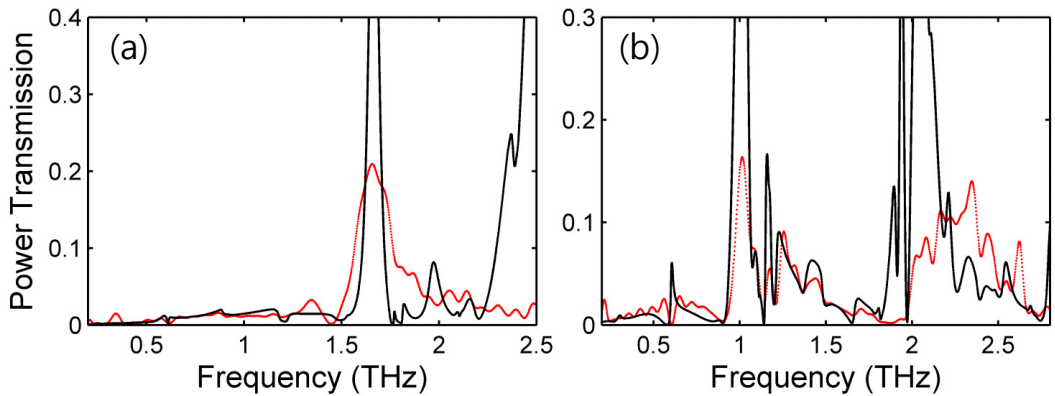
Figure 12.6   Measured power transmission spectra (red) and FDTD simulation (black) with (b) 90-μm and (c) 160-μm air gaps when the slit arrays are misaligned with a 20 μm.

In Chapter 12.2, we found discrepancies between the FDTD simulation results and the measured data for real samples of corresponding size. In the process of sample production, the sizing errors will inevitably occur—we estimate this to be approximately 10−20 µm in our case—and in an attempt to control for this effect, we simulated a case in which the top plate was misaligned with the bottom plate by 20 µm. It should be noted that the air gap remained constant, which should have left the frequency of resonant transmission unaffected. Figure 12.6 shows the measured levels of power transmission (red lines, indicating the same levels as in Fig. 12.2) against an FDTD simulation (black line) of this case. Although resonant transmission is still high, the resonances between the first and the second resonant frequencies decrease (indicating their relation to the periodicity of the slit arrays), and the measured and simulated results show an improved overall agreement.

12.5   FDTD simulations : Photonic PPWG
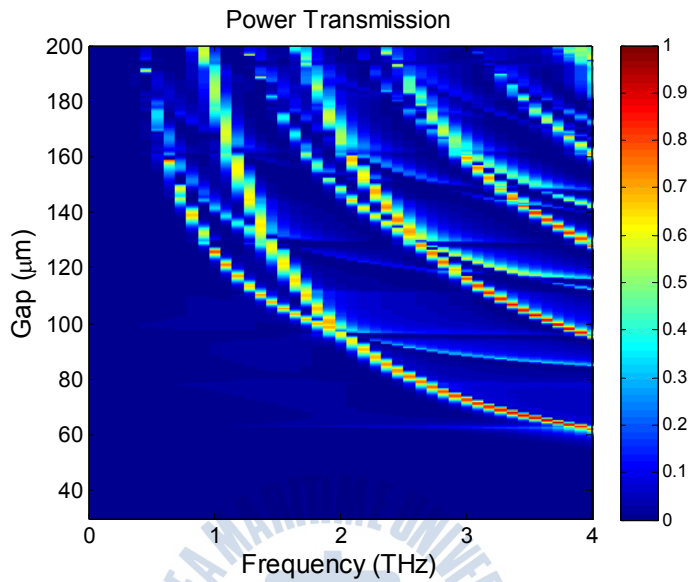
Figure 12.7   3-D THz power transmission of the photonic PPWG
with the different air gaps, g.

Figure 12.7 shows the FDTD simulation results for a photonic PPWG with two
metal plates patterned with slit arrays with a width of 65 µm and a period of 500
µm and positioned by a half-pitch offset width. Here, the air gap g is increased
from 30 to 200 µm. The graph shows a strong resonant transmission property that
follows Eq. (43), indicating that the resonant frequency can be controlled by
changing the air gap size. Moreover, owing to diffraction, low-frequency regions
cannot propagate along this photonic PPWG; further, as discussed previously, the
resonance between the resonant frequencies can be removed by misaligning the two
slit arrays.

Chapter XIII.   Conclusion

In the thesis, we have shown the properties of THz wave propagation in 1) PPWGs and 2) photonic PPWGs combined with photonic crystal structures such as slits and grooves.

It was first demonstrated that PPWGs are an optimal form of waveguides in that they are low-loss, have no modal-dispersion and high free-space coupling, and are simple to fabricate. We showed further that by using the TE_1 mode, the PPWG could cut off the low frequency regions, allowing it to serve as a low-pass filter without the need for photonic crystals or changes in geometry.

A photonic crystal is an artificial material with a periodically varying dielectric constant that produces photonic band gaps in which transmission is prohibited in certain directions. In the work underlying this thesis, slit and grooved photonic crystal structures were combined with PPWGs to obtain band gaps originating from a variety of forming mechanisms, including Bragg reflection, π radian phase differences, and standing-wave cavity modes.

A variety of single slit or grooved devices were used to obtain a (tunable) notch filter and a gas/liquid sensor with a high Q factor. Slit and groove arrays were also utilized to produce low- and band-pass filters.

Finally, a novel PPWG structure featuring two metal plates patterned with slit arrays was suggested. We demonstrated that the characteristics of resonant transmission for this device depend upon air gap size. In TEM mode, we were able to cut off low frequencies for the first time within the THz range.

Our investigations of the photonic crystal PPWG developed for this thesis are still ongoing and will likely have uses in future integrated component and sensor systems.

Reference

1. M. C. Kemp, P. F. Taday, B. E. Cole, J. A. Cluff, A. J. Fitzgerald, and W. R. Tribe, "Security applications of terahertz technology," Proc. SPIE 5070, 44 (2003).

2. D. M. Mittleman, M. Gupta, R. Neelamani, R. G. Baraniuk, J. V. Rudd, and M. Koch, "Recent advances in terahertz imaging," Appl. Phys. B, 68, 1085 (1999).

3. N. Karpowicz, H. Zhong, C.L. Zhang, K.-I Lin, J.-S. Hwang, J. Xu, and X.-C. Zhang, "Compact continuous-wave subterahertz system for inspection applications," Appl. Phys. Lett. 86, 054105 (2005).

4. P. H. Siegel, "Terahertz technology in biology and medicine," IEEE Trans. Microwave Theory Tech. 52, 2438 (2004).

5. H.-J. Song and T. Nagatsuma, "Present and future of terahertz communications," IEEE Trans. Terahertz Science and Technology, 1(1), 256 (2011).

6. P. H. Siegel, "THz Instruments for Space," IEEE Trans. Antenn. Propag. 55(11), 2957 (2007).

7. C. A. Schmuttenmaer, "Exploring dynamics in the far-infrared with terahertz spectroscopy," Chem. Rev . 104, 1759−1779 (2004).

8. R. W. McGowan, G. Gallot, and D. Grischkowsky, "Propagation of ultrawideband short pulses of terahertz radiation through submillimeter-diameter circular waveguides," Opt. Lett. 24(20), 1431−1433 (1999).

9. G. Gallot, S. P. Jamison, R. W. McGowan, and D. Grischkowsky, "Terahertz waveguides," J. Opt. Soc. Am. B 17(5), 851−863 (2000).

10. S. P. Jamison, R. W. McGowan, and D. Grischkowsky, "Single-mode waveguide propagation and reshaping of sub-ps terahertz pulses in sapphire fibers," Appl. Phys. Lett. 76(15), 1987−1989 (2000).

11. R. Mendis and D. Grischkowsky, "Plastic Ribbon THz Waveguides," J. Appl. Phys. 88, 4449-4451 (2000).

12. D. Grischkowsky, "Optoelectronic characterization of transmission lines and waveguides by terahertz timedomain spectroscopy," IEEE J. Sel. Top. Quantum Electron. 6(6), 1122−1135 (2000).

13. T. Akalin, A. Teizebré and B. Bocquet, "Single-wire transmission lines at terahertz frequencies," IEEE Trans. Microw. Theory Tech. 54(6), 2762−2767 (2006).

14. T.-I. Jeon, J. Zhang, and D. Grischkowsky, "THz sommerfeld wave propagation on a single metal wire," Appl. Phys. Lett. 86(16), 161904 (2005).

15. K. Wang, and D. M. Mittleman, "Metal wires for terahertz wave guiding," Nature 432(7015), 376−379 (2004).

16. T.-I. Jeon, and D. Grischkowsky, "Direct optoelectronic generation and detection of subps electrical pulses on sub-mm coaxial transmission lines," Appl. Phys. Lett. 85(25), 6092−6094 (2004).

17. R. Mendis, and D. Grischkowsky, "Undistorted guided-wave propagation of subpicosecond terahertz pulses," Opt. Lett. 26(11), 846−848 (2001).

18   R. Mendis, and D. Grischkowsky, "THz interconnect with low loss and low group velocity dispersion," IEEE Microw. Wirel. Compon. Lett. 11(11), 444−446 (2001).

19   Joseph S. Melinger, N. Laman, S. Sree Harsha and D. Grischkowsky, " Line narrowing of terahertz vibrational modes for organic thin polycrystalline films within a parallel plate waveguide, " Appl. Phys. Lett. 89, 251110 (2006).

20   D. M. Mittleman, "Sensing with Terahertz Radiation," Springer (2003).

21   B.-Y Shew, H.-C Li, C.-L Pan, and C.-H Ko, "X-ray micromachining SU-8 resist for a terahertz photonic filter", J. Phys. D: Appl. Phys. 38, 1097 (2005).

22   Tushar Prasad, Vicki L. Colvin, Zhongping Jian, and Daniel M. Mittleman, "The superprism effect in a metal-clad terahertz photonic crystal slab," Opt. Lett. 32, 683 (2007).

23   S. S. Harsha, N. Laman, and D. Grischkowsky, "High Q terahertz bragg resonances within a metal parallel plate waveguide," Appl. Phys. Lett. 94(9), 091118 (2009).

24   A. L. Bingham, Y. Zhao, and D. Grischkowsky, "THz parallel plate photonic waveguides," Appl. Phys. Lett. 87(5), 051101 (2005).

25   S. Coleman and D. Grischkowsky, "A THz transverse electromagnetic mode two-dimensional interconnect layer incorporating quasi-optics," Appl. Phys. Lett. 83(18) (2003).

26   M. Gong, T.-I. Jeon, and D. Grischkowsky, "THz surface wave collapse on coated metal surfaces," Opt. Express 17(19), 17088 (2009).

27   R. Mendis and D. M. Mittleman, "A 2-D artificial dielectric with $0 \leq n < 1$ for the terahertz region," IEEE Microw. Wirel. Compon. Lett. 58(7), 1993−1998 (2010).

28   R. Mendis, A. Nag, F. Chen, and D. M. Mittleman, "A tunable universal terahertz filter using artificial dielectrics based on parallel-plate waveguides," Appl. Phys. Lett. 97(13), 131106 (2010).

29   R. Mendis, D. M. Mittleman, "Multifaceted terahertz applications of parallel-plate waveguide: TE_1 mode," Electronics Letters, 46(26), 40-44, (2010).

30   R. Mendis, V. Astley, J. Liu, and D. M. Mittleman, "Terahertz microfluidic sensor based on a parallel-plate waveguide resonant cavity," Appl. Phys. Lett. 95(17), 171113 (2009).

31   V. Astley, K. S. Reichel, J. Jones, R. Mendis, and D. M. Mittleman, "Terahertz multichannel microfluidic sensor based on parallel-plate waveguide resonant cavities," Appl. Phys. Lett. 100, 231108 (2012).

32   H. Nemec, P. Kuzel, F. Garet, and L. Duvillaret, "Time-domain terahertz study of defect formation in one-dimensional photonic crystals," Appl Opt. 43, 1965-70 (2004).

33   Y. Zhao and D. Grischkowsky, "Terahertz Demonstrations of Effectively Two Dimensional Photonic Bandgap Structures" Opt. Lett. 31, 1534-1536, (2006).

34   Z. Jian, J. Pearce, and D. Mittleman, "Defect modes in photonic crystal slabs studied using terahertz time-domain spectroscopy", Opt. Lett., 29, 2067 (2004).

35   N. Jukam, and M. Sherwin, "Two-Dimenisional terahertz photonic crystal fabricated by deep refractive ion etching in Si", Appl. Phys. Lett. 83, 21 (2003).

36   F. Miyamuru, T. Kondo, T. Nagashima, and M. Hangyo, "Large Polarization change in two-dimensional metallic photonic crystals in subterahertz region", Appl. Phys. Lett., 82, 2568 (2003).

37   H. Park, M. Cho, J. Kim, and H. Han, "Terahertz pulse transmission in plastic photonic crystal fibres," Phys. Med. Biol. 47 3765-3769 (2002).

38   T.-I. Jeon, "NEW APPLICATIONS OF THz TIME-DOMAIN SPECTROSCOPY," PhD thesis, May (1997).

39   M. Exter and D. Grischkowsky, "Characterization of an Optoelectronic Terahertz Beam System", IEEE Trans. Microwave Theory Tech. 38, 1684 (1990).

40   J. D. Jackson, "Classical Electrodynamics" (John Wiley & Sons, New York, 3rd edition, 1999).

41   N. Marcuvitz, Waveguide Handbook (Peregrinus, London, 1993).

42   M. M. Nazarov, L. S. Mukina, A. V. Sjuvaev, D. A. Sapozhnikov, A. P. Shkurinov and V. A. Trofimov, "Excitation and propagation of surface electromagnetic waves studied by terahertz spectrochronography," Laser Phys. Lett. 2, 471 (2005).

43   T.-I. Jeon, and D. Grischkowsky, "THz Zenneck surface wave (THz surface plasmon) propagation on a metal sheet," Appl. Phys. Lett. 88(6), 061113 (2006).

44   C. Ropers, D. J. Park, G. Stibenz, G. Steinmeyer, J. Kim, D. S. Kim, and C. Lienau, "Femtosecond light transmission and subradiant damping in plasmonic crystals," Phys. Rev. Lett. 94(11), 113901 (2005).

45   F. López-Tejeira, F. J. García-Vidal, and L. Martín-Moreno, "Scattering of surface plasmons by one-dimensional periodic nanoindented surfaces," Phys. Rev. B 72(16), 161405 (2005).

46   K. Matsumaru, "Reflection coefficient of E-plane tapered waveguides," IRE Trans. Microwave Theor. Tech. 6(2), 143−149 (1958).

47   H. G. Unger, "Circular waveguide taper of improved design," Bell Syst. Tech. J. 37, 899−912 (1958).

48   S. Panknin, A. K. Hartmann, and T. Salditt, "X-ray propagation in tapered waveguides: Simulation and optimization," Opt. Commun. 281(10), 2779−2783 (2008).

49   A. Rusina, M. Durach, K. A. Nelson, and M. I. Stockman, "Nanoconcentration of terahertz radiation in plasmonic waveguides," Opt. Express 16(23), 18576−18589 (2008).

50   J. Lloyd-Hughes, G. Scalari, A. van Kolck, M. Fischer, M. Beck, and J. Faist, "Coupling terahertz radiation between sub-wavelength metal-metal waveguides and free space using monolithically integrated horn antennae," Opt. Express 17(20), 18387−18393 (2009).

51   J. Zhang, and D. Grischkowsky, "Adiabatic compression of parallel-plate metal waveguides for sensitivity enhancement of waveguide THz time-domain spectroscopy," Appl. Phys. Lett. 86(6), 061109 (2005).

52   E. Yablonovitch, "Inhibited spontaneous emission in solid-state physics and electronics," Phys. Rev. Lett. 58, 2059-2062 (1987).

53   J. D. Joannopoulos, R. D. Meade, and J. N. Winn, Photonic Crystals: Molding the Flow of Light (Princeton University Press, Princeton, NJ, 1995).

54   N. Amer, W. C. Hurlbut, B. J. Norton, Yun-Shik Lee, S. L. Etringer, and B. K. Paul, "Terahertz wave propagation in one-dimensional periodic dielectrics," Appl. Opt. 45, 1857 (2006).

55   Han, H., H. Park, M. Cho, and J. Kim, "Terahertz pulse propagation in a plastic photonic crystal fiber," Appl. Phys. Lett. 80, 2634-2636 (2002).

56   K. Takagi, K. Seno, and A. Kawasaki: Fabrication of a three- dimensional terahertz photonic crystal using monosized spherical particles. Appl. Phys. Lett. 85, 3681 (2004).

57   W. Shan, W. Walukiewicz, J. W. Ager, E. E. Haller, J. F. Geisz, D. J. Friedman, J. M. Olson, and S. R. Kurtz, "Band Anticrossing in GaInNAs Alloys," Phys. Rev. Lett. 82, 1221 (1999).

58   Y. Akahane, T. Asano, B. S. Song, and S. Noda, "High-Q photonic nanocavity in a two-dimensional photonic crystal," Nature 425, 944 (2003).

59   M. Notomi, A. Shinya, S. Mitsugi, E. Kuramochi, and H.-Y. Ryu, "Waveguides, resonators and their coupled elements in photonic crystal slabs," Opt. Express 12, 1551 (2004).

60   A. L. Bingham and D. Grischkowsky, "High Q, one-dimensional terahertz photonic waveguides," Appl. Phys. Lett. 90(9), 091105 (2007).

61   V. Astley, B. McCracken, R. Mendis, and D. M. Mittleman, "Analysis of rectangular resonant cavities in terahertz parallel-plate waveguides," Opt. Lett. 36(8), 1452−1454 (2011).

62   J.-Y. Lu, H.-Z. Chen, C.-H. Lai, H.-C. Chang, B. You, T.-A. Liu, and J.-L. Peng, "Application of metal-clad antiresonant reflecting hollow waveguides to tunable terahertz notch filter," Opt. Express 19(1), 162−167 (2011).

63   Z. Han and S. I. Bozhevolnyi, "Plasmon-induced transparency with detuned ultracompact Fabry-Perot resonators in integrated plasmonic devices," Opt. Express 19(4), 3251−3257 (2011).

64   Z. Jian, J. Pearce, and D. Mittleman, "Two-dimensional photonic crystal slabs in parallel-plate metal waveguides studied with terahertz timedomain spectroscopy," Semicond. Sci. and Tech. 20, 300 (2005).

65   R. Mendis and D. M. Mittleman, "Comparison of the lowest-order transverse-electric (TE$_1$) and transverse-magnetic (TEM) modes of the parallel-plate waveguide for terahertz pulse applications," Opt. Express 17(17), 14839−14850 (2009).

66   J. P. Laib and D. M. Mittleman, "Temperature-dependent terahertz spectroscopy of liquid n-alkanes," J. Infrared Milli. Terahz. Waves 31(9), 1015-1021 (2010).

67   A. P. Hibbins, and J. R. Sambles, "Squeezing millimeter waves into microns," Phys. Rev. Lett. 92(14), 143904 (2004).

68   Z. Marcet, J. W. Paster, D. W. Carr, J. E. Bower, R. A. Cirelli, F. Klemens, W. M. Mansfield, J. F. Miner, C. S. Pai, and H. B. Chan, "Controlling the phase delay of light transmitted through double-layer metallic subwavelength slit arrays," Opt. Lett. 33(13), 1410 (2008).

69   C.-M. Wang, Y.-C. Chang, and D. P. Tsai "Spatial filtering by using cascading plasmonic gratings," Opt. Express 17(8), 6218 (2009).

70   Y. Todorov, A. M. Andrews, I. Sagnes, R. Colombelli, P. Klang, G. Strasser, and C. Sirtori, "Strong light-matter coupling in subwavelength metal-dielectric microcavities at terahertz frequencie," Phys. Rev. Lett. 102, 186402 (2009).

71   Y. Todorov, L. Tosetto, J. Teissier, A. M. Andrews, P. Klang, R. Colombelli, I. Sagnes, G. Strasser, and C. Sirtori, "Optical properties of metal-dielectric-metal microcavities in the THz frequency range," Opt. Express 18(13), 13886 (2010).